



LUND UNIVERSITY

Electric drive and charging system for heavy vehicles

Solutions based on Electric Road Systems

Karlsson, Anton

2022

Document Version:

Publisher's PDF, also known as Version of record

[Link to publication](#)

Citation for published version (APA):

Karlsson, A. (2022). *Electric drive and charging system for heavy vehicles: Solutions based on Electric Road Systems*. Division of Industrial Electrical Engineering and Automation, Faculty of Engineering, Lund University.

Total number of authors:

1

General rights

Unless other specific re-use rights are stated the following general rights apply:

Copyright and moral rights for the publications made accessible in the public portal are retained by the authors and/or other copyright owners and it is a condition of accessing publications that users recognise and abide by the legal requirements associated with these rights.

- Users may download and print one copy of any publication from the public portal for the purpose of private study or research.
- You may not further distribute the material or use it for any profit-making activity or commercial gain
- You may freely distribute the URL identifying the publication in the public portal

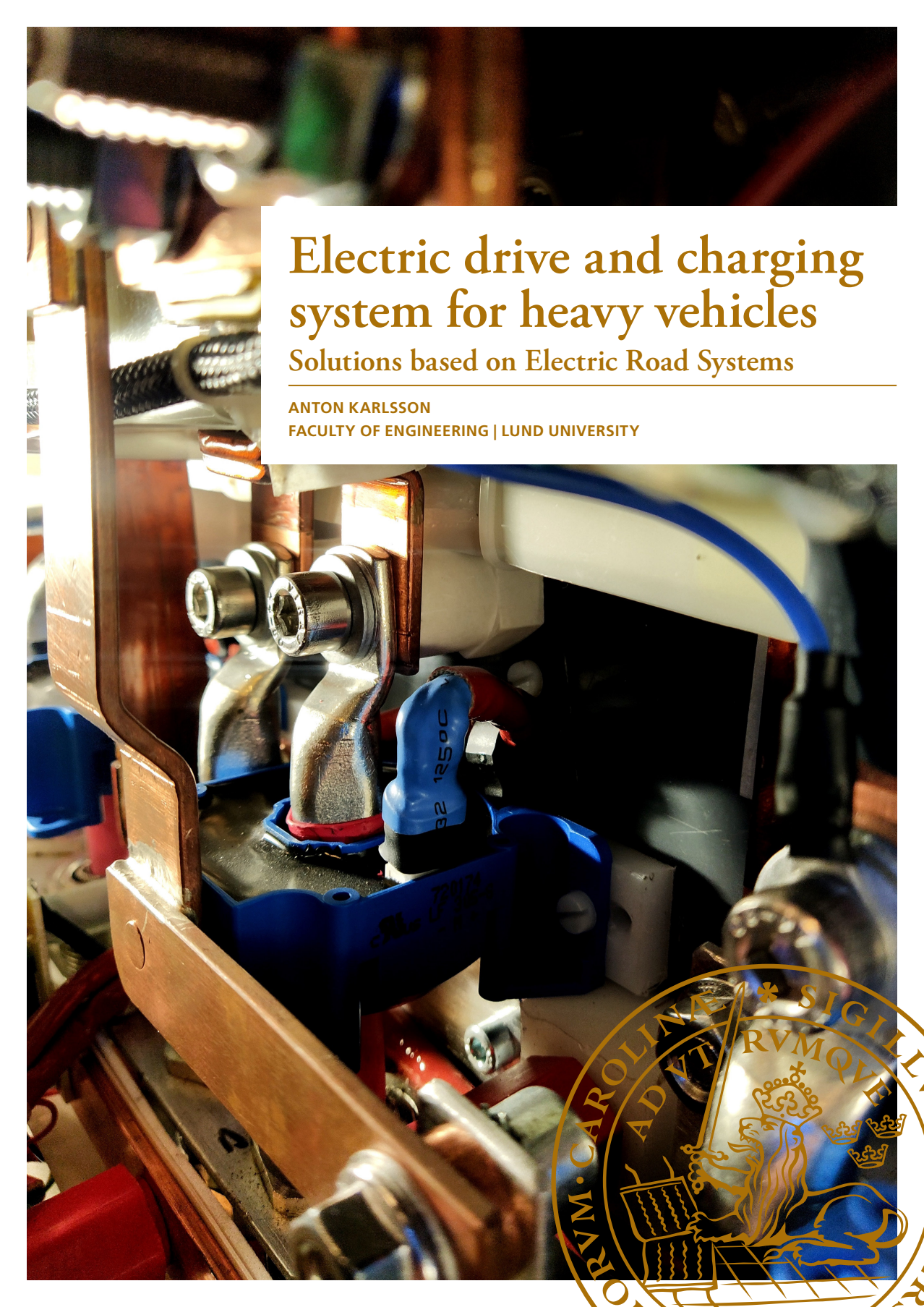
Read more about Creative commons licenses: <https://creativecommons.org/licenses/>

Take down policy

If you believe that this document breaches copyright please contact us providing details, and we will remove access to the work immediately and investigate your claim.

LUND UNIVERSITY

PO Box 117
221 00 Lund
+46 46-222 00 00



Electric drive and charging system for heavy vehicles

Solutions based on Electric Road Systems

ANTON KARLSSON

FACULTY OF ENGINEERING | LUND UNIVERSITY



Electric drive and charging system for heavy vehicles

Electric drive and charging system for heavy vehicles

Solutions based on Electric Road Systems

by Anton Karlsson



LUND
UNIVERSITY

Thesis for the degree Doctor of Philosophy in Engineering
Thesis advisors: Prof. Mats Alaküla, Dr. Avo Reinap
Faculty opponent: Assoc. Prof Pia Lindh

To be presented, with the permission of the Faculty of Engineering of Lund University (LTH), for public criticism in the KC:A lecture hall, Sölvegatan 39, 223 62 Lund, on Friday, the 25th of March 2022 at 10:00.

Organization LUND UNIVERSITY Div. Industrial Electrical Engineering and Automation Box 118 SE--221 00 LUND Sweden		Document name DOCTORAL DISSERTATION	
Author(s) Anton Karlsson		Date of disputation 2022-03-25	
		Sponsoring organization	
Title and subtitle Electric drive and charging system for heavy vehicles: Solutions based on Electric Road Systems			
Abstract The electrification of road bound transport is to some extent limited by the large cost of the energy storage required on-board the vehicles, i.e., the cost of the battery. One way of reducing the required capacity of the on-board energy storage is to enable the possibility to supply the vehicles with electrical energy while it is moving, also called dynamic charging. The energy transfer is usually achieved by either an inductive or conductive coupling between the static supply and moving vehicle. This thesis focuses on a conductive energy transfer system and the challenges that follows, mainly the preference that the supply and the on-board voltage system should be galvanically isolated. A prototype electrical powertrain is developed in a laboratory environment with the purpose of proving the concept as well as gathering measurement data for model validation. The data gathered is used to model three different types of electrical powertrains, each with a different philosophy with regard to galvanic isolation, and to compare their performance from an energy consumption and battery degradation point of view. The experimentally verified powertrain of this thesis features <i>integrated</i> energy transfer capabilities, meaning components originally only meant for traction purposes are also utilized in the process of transferring energy from an external supply to the wheels and energy storage on-board the vehicle. It turns out that this approach to energy transfer can be shown to be beneficial under certain circumstances, such as vehicle type, electric road characteristics for instance, compared to a <i>separate</i> energy transfer solution, where one separate component has, as its only purpose, the responsibility to transfer energy from a supply to the wheels and energy storage.			
Key words Electric Road System, integrated charging, galvanic isolation			
Classification system and/or index terms (if any)			
Supplementary bibliographical information		Language English	
ISSN and key title		ISBN 978-91-985109-4-2 (print) 978-91-985109-5-9 (pdf)	
Recipient's notes		Number of pages 157	Price
		Security classification	

I, the undersigned, being the copyright owner of the abstract of the above-mentioned dissertation, hereby grant to all reference sources the permission to publish and disseminate the abstract of the above-mentioned dissertation.

Signature  _____

Date 2022-02-07 _____

Electric drive and charging system for heavy vehicles

Solutions based on Electric Road Systems

by Anton Karlsson



LUND
UNIVERSITY

A doctoral thesis at a university in Sweden takes either the form of a single, cohesive research study (monograph) or a summary of research papers (compilation thesis), which the doctoral student has written alone or together with one or several other author(s).

In the latter case the thesis consists of two parts. An introductory text puts the research work into context and summarizes the main points of the papers. Then, the research publications themselves are reproduced, together with a description of the individual contributions of the authors. The research papers may either have been already published or are manuscripts at various stages (in press, submitted, or in draft).

Cover illustration front: Photograph from the inside the switch box. Photographed by the author.

© Anton Karlsson 2022

Div. Industrial Electrical Engineering and Automation
Department of Biomedical Engineering
Faculty of Engineering
Lund University

ISBN: 978-91-985109-4-2 (print)

ISBN: 978-91-985109-5-9 (pdf)

CODEN: LUTEDX/(TEIE-1095)/1-149/(2022)

Printed in Sweden by Media-Tryck, Lund University, Lund 2022



Media-Tryck is a Nordic Swan Ecolabel certified provider of printed material. Read more about our environmental work at www.mediatryck.lu.se

MADE IN SWEDEN 

And I knew exactly what to do. But in a much more real sense, I had no idea what to do.
Michael Scott

Contents

List of publications and author contribution	iii
Acknowledgements	v
Popular summary in English	vii
Populärvetenskaplig sammanfattning på svenska	ix
Nomenclature	xi
1 Introduction	1
1.1 Electrical energy transfer system	2
1.1.1 Static	2
1.1.2 Dynamic	5
1.2 Safety	6
1.3 Motivation of the research	7
1.4 Objectives and limitations	9
1.5 Contribution	9
1.6 Disposition	10
2 System solutions for conductive dynamic energy transfer	13
2.1 High power Separate Energy Transfer System, HSETS	16
2.2 Low power Separate Energy Transfer System, LSETS	17
2.3 Fully Integrated Energy Transfer System, FIETS	18
2.4 ERS	21
2.4.1 Equal distance, 'EQU'	21
2.4.2 Power dependant, 'ADA'	21
2.5 Chapter summary	23
3 Modelling	25
3.1 Vehicle/ETS modelling	25
3.1.1 Vehicle dynamics	26
3.1.2 Traction drives and mechanical transmission	27
3.1.3 Energy storage and auxiliaries	29
3.1.4 DC-DC converter	31
3.1.5 Energy consumption	32
3.1.6 Driver model and Power Flow Control	33
3.2 Power electronics modelling	36

3.3	Chapter summary	39
4	Experimental setup	41
4.1	Introduction	41
4.2	Hardware	41
4.3	Software	46
4.3.1	Electric machine control	47
4.3.2	Switch box and switching sequence	49
4.4	Preparations of Measurements	53
4.4.1	Charging efficiency	53
4.4.2	Dynamic switching behaviour	54
4.4.3	Common mode current	55
4.5	Chapter summary	56
5	System validation and analysis	57
5.1	Measurement Results	57
5.1.1	Efficiency	57
5.1.2	Dynamics of switching of electrical supply	59
5.1.3	Post processing	61
5.2	Vehicles	64
5.3	Drive cycles	64
5.4	Parameter sweep	65
5.5	Result and discussion	67
5.5.1	City bus	68
5.5.2	Long haul truck	83
5.6	Chapter summary	92
6	Common mode current validation and analysis	95
6.1	Measurement results	96
6.2	Model validation	102
6.3	Analysis	106
6.4	Chapter summary	110
7	Conclusion and continuation	113
7.1	Future work	115
	Appendices	117
A	Electrical schematics and implementation	119
A.1	Battery model and emulator	119
A.2	Double isolation	120
A.3	EMI filter	122
A.4	FIETS experimental setup	123

List of publications and author contribution

This thesis is based on, but not limited to, the following publications:

- I **EV powertrain topologies for electric road applications**
A. Karlsson, G. Domingues-Olavarria, M. Alaküla
31st International Electric Vehicle Symposium & Exhibition (EVS 31) and International Electric Vehicle Technology Conference 2018 (EVTec 2018), Kobe, Japan, 30 September - 3 October, 2018.
 - I developed the models of the first generation of electrical powertrains suited for dynamic energy transfer. I also did the simulation of a personal car on the WLTP drive cycle with regard to powertrain cost and energy consumption.

- II **Alternative EV powertrain topologies designed for operation in a conductive electric road system**
A. Karlsson, G. Domingues-Olavarria, M. Alaküla
2018 IEEE International Conference on Electrical Systems for Aircraft, Railway, Ship Propulsion and Road Vehicles & International Transportation Electrification Conference (ESARS-ITEC 2018), Nottingham, UK, 7-9 November, 2018.
 - I further developed the models of **Paper I** where the application is heavy vehicles and suitable drive cycles. I performed simulation of these cases and studied the performance with regard to energy consumption and powertrain cost.

- III **Integrated and Isolated EV charger for AC and Electric Road applications**
A. Karlsson, M. Alaküla
2020 International Symposium on Power Electronics, Electrical Drives, Automation and Motion (SPEEDAM), Sorrento, Italy, 24-26 June 2020, pp. 114-119.
 - I took big part in developing a first prototype of a novel powertrain featuring integrated energy transfer from an electric road. I performed several measurements with regard to charging efficiency and dynamic behaviour of the powertrain.

iv **Energy Supply to Buses on a Conductive Electric Road: An Evaluation of Charger Topologies and Electric Road Characteristics**

A. Karlsson, M. Alaküla

World Electric Vehicle Journal. 2021; 12(4):241.

- Based on the result presented in **Paper III** I developed the models of **Paper I-II** to a new level of detail and accuracy and performed simulations of vehicles and electric roads with many different specifications to analyse how certain aspects of the powertrain and/or electric road affects performance.

v **Conductive electric road localization and related vehicle power control**

A. Karlsson, M. Alaküla

World Electric Vehicle Journal. 2022; 13(1):22

- Continuation of **Paper IV** where I present more results established from the simulation study with emphasis on how the electric road placement affects performance.

The thesis author is the original draft manuscript writer (together with G. Domingues-Olavarria in papers I- II) and the main responsible for the conducted research of all the above papers.

All contents of the papers are reproduced with permission of their respective publishers.

Acknowledgements

I have enjoyed going to work most of the days during the years I have spent at LTH and IEA. Partly this is thanks to interesting work topics and the possibility to learn new things on a frequent basis, but mostly I feel it is thanks to the people I have been working with and the people I have shared various lunch and coffee breaks with.

Several individuals have been involved in what has become this thesis work. It would not have been initiated at all had it not been for my main supervisor Prof. Mats Alaküla and for that I am naturally very grateful. When it comes to how to inspire and motivate another person even when things feel close to hopeless, Mats is truly one of a kind. Also, thanks to my co-supervisor, Associate Prof. Avo Reinap who is always available for an interesting approach on the various issues that have arisen during my time as a PhD-student.

I also want to express my gratitude towards Dr. Johan Björnstedt who, I feel, has been my unofficial advisor. Extremely competent and always willing to tackle any issue, theoretical or practical, I have come across.

Thank you also to Getachew Darge, who always choose to see solutions rather than problems. Without GD, probably none of the deadlines in the MFEA project would have been met. Always helpful, always full of ideas.

A special thanks to Lars Lindgren, who also went above and beyond in the early stages of the MFEA project. Thanks for the evenings spent in the lab with Yury to get things going when I couldn't.

During my first years at the division of IEA I spent a great deal of time in our beloved Lab 6 together with Dr. Sebastian Hall. You taught me a lot of trickery regarding Labview FPGA programming and electric machine control but mostly I remember with pleasure our talks about music and life in general. Thanks to Max Collins for all the interesting discussions and splendid company in countless number of lunches. Also, thanks to accountant extraordinaire Dr. Gabriel Domingues for being a great office mate for several years and also for your valuable contribution and input to my work. Thanks also to Dr. Philip Abrahamsson for great collaboration on various topics over the years and for always being ready to get things done.

A big thank you to the entire division of IEA, with Associate Prof. Ulf Jeppsson at the helm, for making the last number of years a pleasure. Thanks to Carina Lindström, Ulrika Westerdahl, Henriette Weibull and Malgorzata Luczak for the administrative support, to Associate Prof. Gunnar Lindstedt, Dr. Francisco Marquez and Prof. Olof Samuelsson for both practical and mental support, to Dr. Rasmus Andersson, Dr. Bobbie Frank and Bengt Simonsson for the entertaining talks and also to David, Martin, Samuel, Alice, Leonardo, Huan and anyone else I might unintentionally have forgotten.

Other individuals involved in the MFEA project also deserves a big thank you, Anders Göransson, Henrik Engdahl, Karin Carlsson and Dr. Yury Loayza Vargas, it would not have been possible without your support and collaboration.

From outside the work-related arena I would like to thank Simon and Ola for our

almost daily conversations on whatever topic is on any of our minds.

A big thanks to Viveka Nilsson for proofreading the thesis.

Thanks to mum and dad for always being supportive and especially when I decided to leave my home town and move to Lund in the first place, now many years ago. For that I should also thank Lehman Brothers for their creative way of getting me fired from my job in 2009, giving me the final push to leave. Thanks to my sister and brother for being supportive in the special way only older siblings can be.

Last but not least, thank you to my lovely family. Ever since the time I started to think about leaving the industry and become a PhD student my girlfriend Isa has been ever so supportive. At the time it was only the two of us, now, almost six years later, we have brought our lovely Einar and Gunnel to the world. You are my favourite people of all, and I love you very much. Thank you for making me forget about work whenever we are together and providing a healthy perspective on life.

Anton Karlsson
Lund, February 2022

Popular summary in English

The infrastructure related to energy transfer to - or charging of - electric vehicles is an important part of the challenge of the electrification of road transport. Traditionally, the transfer of electrical energy to an electric vehicle is achieved by connecting the vehicle to the utility grid, either directly or via a fast charger. This naturally requires the vehicle to be stationary. One alternative to stationary charging is by means of an *electric road* which enables the transfer of energy to a moving vehicle, also referred to as *dynamic* energy transfer or charging. This can be achieved in different ways, either wirelessly, through a magnetic coupling between a transmitter mounted in/on the road surface and a receiver fitted to the vehicle or through a mechanic (conductive) connection, much like the connection utilized by a train or a tram. The motivation of investigating this kind of energy transfer technique is that given the possibility of charging as the vehicle is moving, the requirement on the on-board energy storage capacity is significantly decreased as long as a sufficiently large amount of roads are electric roads. In turn, this can affect the cost of the vehicles in a positive way. The challenges related to the electrification of road transport is not solved by electric roads but rather opens up new ones, some of which are addressed in this thesis, primarily:

Given a (conductive) electric road, how is the energy consumption and battery degradation affected by:

1. the topology of the electrical powertrain on-board the vehicle, and
2. the physical characteristics of the electric road?

As a part of 1) above, a new kind of electrical powertrain for heavy electric vehicles is proposed and verified experimentally. A vehicle adapted for energy transfer from an electric road requires a specific component acting as the 'middle man' between the voltage and current the electric road is able to supply and the voltage and current that is accepted by the on-board high voltage system. This component can become both physically large and heavy as well as costly, which is why it is desirable not to have to incorporate it in the electrical system on-board the vehicle. The powertrain in focus in this thesis presents one way of achieving the same functionality of this component by integrating the energy transfer capability into already existing components on-board the vehicle, referred to as *integrated* charging or energy transfer. In order to evaluate how this type of powertrain performs in comparison to more conventional alternatives, a system level analysis is performed by modelling and simulation of a total of three different energy transfer systems put into context in one city bus case and one long haul truck case.

The physical characteristics, as referred to by 2) above, means how large relative part of a section of road is an electric road (the roads do not completely have to be converted into electric roads) as well as the distance between electric road sections. In this thesis is also an approach to place the electric road section based on the tractive power requirement of the vehicles are also investigated.

It can be concluded that the powertrain specifically developed in this work is promising as its functionality is verified as well as during certain circumstances showing promising result with regard to energy consumption in comparison to its more conventional alternatives.

Furthermore, it is shown that both energy consumption and battery degradation can be significantly altered for the better if the electric road sections are placed along a certain stretch of road according to the tractive power requirement rather than placing them with no regard to the dynamics of the road section.

The work presented in this thesis can be of interest to vehicle manufacturers, aiming to adopt this kind of dynamic energy transfer, as well as electric roads manufacturers and authorities responsible for installation and commissioning of electric roads.

Populärvetenskaplig sammanfattning på svenska

Infrastruktur relaterat energiöverföring till - eller mer vardagligt, laddning av - elektriska fordon är en viktig del av utmaningen som rör elektrifiering av vägbunden transport. Traditionellt sker överföringen av elektrisk energi till ett elfordon via en anslutning till elnätet; antingen direkt till fordonet eller via en snabbbladdare. Detta kräver att fordonet står stilla. Ett alternativt tillvägagångssätt att förse elfordon med energi är med *elvägar*, en teknik som gör det möjligt att överföra elektrisk energi till fordonet medan det är i rörelse, även kallad *dynamisk* energiöverföring eller laddning. Detta kan ske på olika sätt, antingen trådlöst genom en magnetisk koppling mellan en sändare monterat i/på vägen och en mottagare ombord på fordonet, eller via en mekanisk (konduktiv) koppling likt den ett tåg eller spår-vagn utnyttjar. Motivationen till att använda denna typ av teknik bygger på att givet det finns ett sätt att överföra energi till fordonet medan det är i rörelse på en tillräcklig mängd vägar, kan kravet på lagringskapacitet av energi ombord på fordonet reduceras. Detta i sin tur kan leda till att kostnaden för fordonen minskar. Utmaningarna tar dock inte slut här utan öppnar snarare upp för ännu fler, varav några är adresserade i denna avhandling, primärt:

Givet en (konduktiv) elväg, hur påverkas fordonets energiförbrukning och batteridegradering av

1. den elektriska drivlinans elektriska utformning ombord på fordonet, samt
2. elvägens fysiska utbredning i ett specifikt scenario?

Som en del av punkt 1), har en ny typ av drivlina för tunga elektriska fordon föreslagits samt analyserats experimentellt. Ett fordon anpassat för energiöverföring från en elväg behöver en komponent ombord som agerar 'mellanhand' mellan spänningen och strömmen elvägen levererar samt spänningen och strömmen fordonet och dess batteri kan hantera. Denna komponent kan både bli fysiskt stor och tung samt kostsam varför ett sätt att bli av med densamma är önskvärt. Den elektriska drivlina denna avhandling lägger fokus på, presenterar ett sätt att till stor del få samma funktionalitet som ovan nämnda komponent bidrar med, dock genom att integrera energiöverföringskapabiliteten i redan befintliga komponenter ombord på fordonet, kallat *integrerad* laddning eller energiöverföring. För att undersöka hur denna drivlina presterar i jämförelse med mer konventionella metoder har en systemanalys genom modellering och simulering genomförts med totalt tre olika elektriska drivlinor i ett stadsbuss-fall samt ett långtradar-fall.

Med fysisk utbredning av elvägen, som omnämnt i punkt 2) ovan, menas dels hur stor relativ del av en körsträcka som är elvägen placerad på (elvägen behöver högst troligt inte täcka 100% av en specifik sträcka), dels avstånd mellan elvägssektioner. I detta arbete utreds också en strategi som bygger på att elvägssektionerna placeras utmed en specifik sträcka baserat på fordonets traktionseffektbehov.

Vi kan konstatera att den drivlina specifikt utvecklad för detta arbete är lovande i det att funktionen är i en laborationsmiljö verifierad samt att under vissa omständigheter, dess energiförbrukning är fördelaktig i jämförelse mot konventionella alternativ.

Vidare kan vi konstatera att både energiförbrukning och batteridegradering kan signifikant påverkas av att elvägens sektioner placeras baserat på traktionseffektbehov snarare än att placera dem utan att ta hänsyn till vägsträckans, och därmed också fordonets, dynamik.

Det arbete som presenteras i denna avhandling kan vara av värde för både fordonstillverkare som är intresserade av dynamisk energiöverföring med konduktiv elväg men också elvägstillverkare och myndigheter som planerar och ansvarar för installation och driftsättning av elvägar.

Nomenclature

A	Drive cycle aggressiveness (m/s^2)
A_v	Vehicle frontal area (m^2)
C_d	Drag coefficient (-)
C_{par}	Parasitic capacitance (F)
C_r	Rolling coefficient (-)
d_{ers}	Absolute distance between ERS sections (km)
F_{air}	Air resistance (N)
F_{roll}	Rolling resistance (N)
F_{slope}	Slope resistance (N)
f_{sw}	Switching frequency (Hz)
g	Gravitational constant (m/s^2)
k_{ers}	Relative ERS coverage (-)
L_s	Stator inductance (H)
M_v	Vehicle mass (kg)
Ψ_m	Permanent magnet flux (Vs)
P_{aux}	Auxiliary power (kW)
P_{batt}	Battery power (kW)
P_{DC-DC}	Rated power of DC-DC converter (kW)
P_{em}	Rated power of electrical machine (kW)
P_{ERS}	Power supplied by the ERS (kW)
P_{trac}	Mechanical traction power (kW)
R_s	Stator resistance (Ω)
s_{ers}	ERS section length (km)
T	Torque (Nm)
t_{bt}	Blanking time (s)
W_{batt}	Battery capacity (kWh)

AC	Alternating current
ADA	Adapted ERS placing method
AFE	Active front end converter
DC	Direct current
DoD	Depth of discharge
EMD	Electric machine drive
EMI	Electromagnetic interference
EMSM	Electrically magnetised synchronous machine
ERS	Electric road system
ETS	Energy transfer system
EQU	Equidistant ERS placing method
FIETS	Fully integrated energy transfer system
FPGA	Field programmable gate array
HSETS	High power separate energy transfer system
HVAC	Heating ventilation & air condition
ICE	Internal combustion engine
IM	Induction machine
LHT	Long haul truck
LSETS	Low power separate energy transfer system
MnSW	Minimum switching control strategy
MxRE	Maximum regeneration control strategy
OBC	On-board charger
PMSM	Permanent magnet synchronous machine
PWM	Pulse width modulation
p.u	per unit
RCD	Residual-current device

RMS Root mean square
SOC State of charge
TVS Traction voltage system

Chapter 1

Introduction

In recent years an increase of interest in electrification of transport is seen in order to meet regulations and recommendations regarding emissions and the shift from the dependence of fossil fuels. The sales of both passenger vehicles as well as heavy vehicles such as trucks and buses are expected to increase in the coming years [1].

Possibly the main difference between an ICE vehicle and an EV is that the energy storage is 'refilled' differently. In an ICE vehicle the process is short as it is only limited by the volumetric flow rate the pump can provide and it is aided by the fact that the energy density of petroleum is high [2]. Re-charging an EV takes a longer time, even though there are now charging networks providing charging power up to 350 kW [3], [4]. The number of vehicles that can utilize this kind of charging power is, however, limited [5]. The relatively long charging times and the fact that the majority of EVs have shorter range than the typical ICE vehicle is being the main reasons the general public is hesitant to buy an electric vehicle [6], [7]. Another significant reason is the higher cost of EVs compared to their combustion engine counterpart, which mostly depends on the cost of the battery [8].

For heavy vehicles, electrification is a more significant challenge since a larger amount of energy stored on-board is required. A subset of heavy transport, such as city bus transport or inner-city distribution, can, depending on the specific route and load, make use of fast DC charging at end stops or similar. Long haul transport would require a substantial battery capacity together with a charging infrastructure capable of power levels up in the megawatt range. This fact has several implications; on the vehicle side, the cost of the energy storage (battery) will be considerable and the physical size and weight of it might affect the vehicle in such a way that the payload the vehicle can tolerate has to be significantly decreased. On the charging side, the load on the grid must be taken into account when considering providing several charging points capable of several hundreds of kilo watts at a regular basis along the larger roads.

Alternatives to electrifying long haul transport by batteries are for example electrifying by fuel cells where a larger amount of energy can be stored on-board the vehicle. One chal-

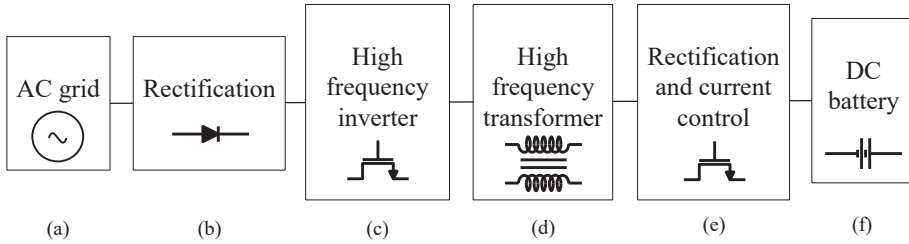


Figure 1.1: The principal stages of supplying electrical energy to an electric vehicle.

lenge regarding electrification by hydrogen fuel cell is that the benefit of faster refuelling is counterweighted by the significantly lower energy efficiency seen from a renewable electric energy source to the wheels [9]. Another way of enabling electrification of transport without the requirement of a vast on-board energy storage is to by some mean be able to transfer electrical energy to the vehicle while it is in motion.

1.1 Electrical energy transfer system

Electrical energy can be supplied to an EV in several ways. Below follows an elaboration of conductive and inductive energy transfer techniques.

1.1.1 Static

Static charging or energy transfer refers to the electric energy flow from a source to the vehicle while it is standing still, or parked. Generally, this means energy transfer from the AC grid or an off-board DC charger but could very well be another vehicle, a photovoltaic system, etc. In all cases, the normal source of the electrical energy is the AC-grid whilst the target is the battery with a DC voltage, implying that some kind of adaption of the electrical quantity is required:

- Rectification of the AC voltage to DC.
- The DC voltage is required to firstly, be adapted to the voltage of the battery, and secondly, be current (power) controlled so that the charging power can be controlled.
- Galvanic isolation between the AC supply and the on-board voltage system (including most importantly the battery) is preferably included.

The items above can be illustrated by the block diagram shown in Fig. 1.1. Generally, all the illustrated parts in the figure are included whether charging the vehicle from the AC-grid, from a DC-charger or by using an inductive charger. Naturally, the AC-grid, Fig. 1.1(a), is not a part of the vehicle whilst the battery, Fig. 1.1(f), is always a part of the physical vehicle.

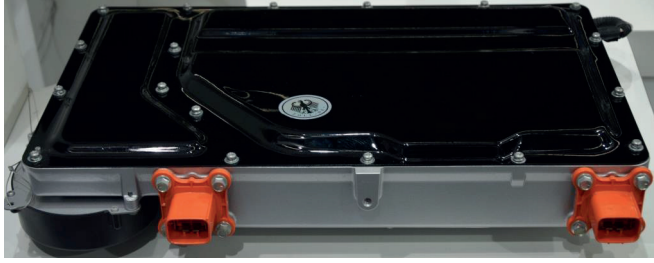


Figure 1.2: An on-board charger (OBC) [10].



Figure 1.3: A DC fast charger [12].

However, depending on the charging method (AC, DC, inductive), the other components, Fig. 1.1(b)-(e), can be either on-board or off-board the vehicle.

When AC charging, i.e., connecting the vehicle to an AC outlet, the equipment depicted in Fig. 1.1(b)-(e) are all part of the on board charger (OBC), an illustration of which is shown in Fig. 1.2, which generally is rated for one or three phase, 7 to 22 kW in personal vehicles [11]. The rated power of the OBC is generally limited as the available physical space and allowed weight on board the vehicle itself is limited. AC charging is typically used when the vehicle is at standstill, parked, for a longer amount of time, e.g., during the night.

On the other hand, when DC-charging, the components depicted in Fig. 1.1(a)-(e) is all off-board the vehicle and the charger is essentially connected directly to the battery poles. As all of the components are localized off-board the vehicle the physical size and weight is not limited to the same extent, meaning higher power levels are possible. Available rated charging power levels are typically in the range of 50 to 350 kW [3], [4], [13]. Fast DC-



Figure 1.4: An inductive charging pad [14].

charging is necessary in order to reduce the time spent on longer trips, i.e., when the energy required to complete the trip exceeds the amount of energy stored in the battery.

Inductive charging of electric vehicles is also a feasible option as shown extensively in literature [15], [16], [17] when considering power and efficiency, especially when considering it as an alternative to AC charging which typically occurs at a lower power level than DC charging. Basically the same components are required as when considering AC or DC charging, as shown in Fig. 1.1, however, the interface between the off-board equipment and the vehicle is the magnetic coupling shown in Fig. 1.1(d). In this case the magnetic coupling between the primary (off-board) and secondary (on-board) coil is through the air. The efficiency and maximum transferable power depends on the relative positioning of, and distance between, these coils [18], [19], making the positioning of the vehicle itself important since the coils are usually fixed on the ground and on the vehicle. A connection to protective earth is not required when utilizing inductive charging since the vehicle is floating with respect to the grid as there is no galvanic connection between the vehicle and the grid. Wireless, inductive energy transfer does add a level of complexity to the charging system, as high magnetising current is generally required due to the large airgap as well as the presence of passive, reactive components in order to achieve adequate magnetic coupling. Taking into account a generally lower efficiency compared to conductive charging [20], the total cost of inductive energy transfer becomes higher than the conductive counterpart.



Figure 1.5: One of the test sites of road bound conductive ERS on public roads in Sweden. Photo: Elonroad

1.1.2 Dynamic

The name 'dynamic charging' of EVs is here used to indicate that the vehicle is able to receive energy whilst moving. This can be made possible by an Electric Road System (ERS) which can be either conductive or inductive. Both techniques are and have been evaluated in several different projects and at different levels of technical readiness [21]. Most of these projects and demonstrators feature a relatively short ERS, around a few hundred meters.

A conductive ERS works in a similar fashion to that of a train or a tram where a current collector, mounted on the vehicle - above, underneath or at the side - is in mechanical contact with a conducting element, covering a certain stretch of the road. Fig. 1.5 shows a close-up of one of the test sites where a road bound conductive ERS is evaluated on public roads. This particular ERS utilizes a segmented approach where only the segments beneath a vehicle are activated. Another test facility is shown in Fig. 1.6 where the ERS is based on overhead lines. Most of the conductive electric road techniques found in literature use DC to transfer energy to the moving vehicle, although AC could also be used [22].

The inductive ERS is similar to its static counterpart where the difference is that several transmitting coils are placed along a certain stretch of the road. This means that the transferred power on board the vehicle will be observed as pulsating as the vehicle couples and decouples to the coils that it passes over.

The transverse positioning of either the current collector in the conductive case or receiving coil in the inductive case is important as the vehicle is possibly not positioned perfectly centred above or below the ERS. This can be solved by having the current collector or receiving coil mounted on a tracking actuator, keeping it properly positioned.



Figure 1.6: One of the test sites of road bound conductive ERS on public roads in Sweden. Photo: Region Gävleborg

Features such as self-driving or driving aid, which are largely present in vehicles today, can also contribute to keep the vehicle properly positioned.

Dynamic energy transfer, if not present at all parts of a drive cycle, must transfer the energy that the vehicle needs both when and when not having access to dynamic energy transfer. A heavy duty truck that uses, for instance, 100 kW for propulsion on a highway, requires 200 kW from the dynamic energy supply if only 50% of the road provides energy supply e.g., 1 out of every 2 km. This means that the energy transfer requirements of an ERS may be in the order of several hundred kilowatts. Conductive energy transfer can handle such power levels with very small contact surfaces, in the order of some square centimetres. This can be regarded as a "power density". Dynamic inductive energy transfer does in that comparison require much more space, having a power density of 50-150 kW per square meter [23], [24]. On the other hand, one advantage of the inductive energy transfer is that the *whole vehicle* is galvanically separated from the supply as the magnetic coupling occurs in the interface between the off- and on-board equipment.

1.2 Safety

The conductive and inductive electric road solutions are fundamentally different when assessing the safety precautions that has to be taken should an isolation fault occur on-board the vehicle. With inductive energy transfer, since the vehicle is galvanically separated from

the charging supply, should an isolation fault occur while charging, the chassis of the vehicle will not be put on an electric potential that could be harmful for living beings. In the conductive case, however, should the same fault occur, the chassis of the vehicle could be put on dangerous electrical potential if the ERS supply has an earthed system. In order to prevent this from happening, one could add an additional layer of electrical isolation to all of the components part of the high voltage system, a.k.a. "double isolation". This way, two independent isolation faults has to occur before a possible harmful situation can arise. Another approach is to galvanically separate the charging supply and the on-board high voltage system by means of an isolated DC-DC converter, illustrated by Fig. 1.1(c)-(e). The isolated DC-DC converter would in this case act as an interface between the current collector of the vehicle and the high voltage system. It has to be noted, though, that even when utilizing a DC-DC converter, the electrical components installed on the primary side of it has to be double isolated. The former method might be practically challenging depending on the system architecture, the latter requires a costly and possibly bulky device to be added to the vehicle.

There are conductive electric road systems under evaluation that are floating with respect to ground [25] making the isolation on-board the vehicle not necessary. There are issues to be aware of in this approach, since if the ERS sections are physically large, the capacitive parasitic coupling to ground might not be negligible, creating an, albeit high impedance, reference to ground. Another scenario is if an isolation fault occurs in one vehicle, and if another isolation fault occurs - in another vehicle even, connected to the same ERS - might cause a dangerous situation.

1.3 Motivation of the research

The battery is the single highest cost carrying component of an electric vehicle [8] and albeit the cost has been, and still is, decreasing [26], [27], it still carries a significant part. One way of reducing the on-board capacity of the battery, and consequently cost, is to facilitate a way of providing the vehicles energy while in motion. It is shown that, should all of the road transport be fully electric, the societal cost will be lower if an electric road system is implemented on all major roads rather than equipping the vehicle fleet with a sufficiently large capacity battery and build an extensive network of fast chargers to cover all of its needs [28], [29].

The Swedish Government is planning the dissemination of conductive ERS with 2000 km ERS by 2030 and 3000 km ERS by 2035, as a major solution to facilitate a full electrification of road transport in Sweden [30]. This obvious increasing interest in Electric Road Systems and based on what is elaborated on in earlier sections; that higher power densities can be achieved with conductive energy transfer in comparison to inductive energy transfer a conductive ERS is of focus in this thesis. Following the decision to utilize an ERS, a number of challenges arise as to where and how should the ERS sections be placed along a certain stretch of road as well as how much power should the ERS be able to provide. It

is also important to try and quantize how/if the placing of the ERS affects the operational costs of a vehicle.

Given a conductive ERS, as mentioned in an earlier section, the proper safety precautions have to be taken when considering the technology used for energy transfer from the ERS to the vehicles traction and battery system. It is not obvious, when considering energy efficiency and manufacturing cost, how the charger and/or electric propulsion system on-board the vehicle should be designed.

Publications related to dynamic charging of electric vehicles that can be found in literature mostly concern wireless, inductive, methods of transferring energy from the stationary supply to the moving vehicle. Of these, several studies analyse the shape and layout of the coils [31] - [32]. In [33] a stochastic method of placing the charging sections of a dynamic charging system is proposed (again, aimed at inductive energy transfer) and in [34] a system approach to find the amount of battery capacity that can be reduced thanks to (wireless) dynamic charging availability is presented. The study presented in [35] investigates how the relative coverage of dynamic energy supply and its maximum power transfer capability affects the driving range of a vehicle. However, the energy transfer method is inductive and little concern is made to the on-board part of the charging system. A summary of *conductive* dynamic charging systems that are under development is presented in [36], however it does not provide a system level approach in conjunction with the vehicles operating the conductive electric road. References [25], [37] present a validated method of transferring high power levels through a conductive dynamic charging solution, but they do not discuss alternative architectures of the high voltage system on-board the vehicle, nor how these impact the energy consumption or battery degradation.

Different methods and solutions to *static* integrated charging can be found in literature and [38] present a comprehensive summary of typical characteristics of said chargers in recent literature. In most of the reported solutions in [38] the charger is either low power or non-isolated, only a few feature both high power and isolation. Although it was not the intention, there are a few charger topologies presented that could relatively easily be adapted for dynamic charging, namely those that feature two separate electrical machines or one six-phase machine, by separating the DC-link to one for each machine or pair of three phases, i.e., one separate three phase converter per three phases. This way, one DC-link can be connected to the battery and one to the DC-supply. If there are two separate machines, they do need to be mechanically connected. There are publications presenting solutions to isolated, high-power charging where either a six phase machine and/or inverter is required [39], [40] or where reconfiguration of the motor windings are required [41]. The integrated charging solutions described in [38]-[41] are all intended for *static* charging and *none* of the solutions described are suitable for dynamic energy transfer. This is due to the fact that the scientific and engineering field of dynamic conductive ERS is very young.

Based on the above, where a gap in related research concerning *conductive* ERS and on-board charging topology is established, this thesis presents a study on high power conductive dynamic energy transfer applied to real-world use cases. Both relative coverage of

the ERS and the distance between ERS sections are part of the study where driving range, energy consumption and battery degradation are the outcomes of interest. Besides the ERS characteristics investigated, different topologies of the on-board propulsion and charging system are part of the evaluation to investigate their effect on the aforementioned outcomes.

1.4 Objectives and limitations

The purpose of this thesis is to evaluate different approaches to enable energy transfer from a conductive electric road whilst solving the safety requirements and taking system and operational cost into consideration. Operational cost is in this context limited to energy consumption and battery degradation. Apart from the design of the high voltage system on-board the vehicle, the placement of the ERS is also evaluated from the same point of view as in how the placement affect the energy consumption and battery degradation of the vehicle. Also, how much ERS is actually required.

The evaluation takes shape as modelling and simulations of three different electric powertrains which all conform to the safety requirements but each with a different approach to how to provide the transfer of energy from the ERS to the battery and traction machines. One of the powertrains utilize a method of the energy transfer where the equipment used for traction purposes is also a vital part of the energy transfer from ERS to battery, known as *integrated* energy transfer/charging. One could argue that this solution is the most technically challenging when it comes to design and control, which is why this powertrain is built and validated in a laboratory environment. The results from the measurements on this powertrain are then used in the simulations, where the common components, such as electric machines, are modelled the same way across the powertrains in order to isolate cause and effect.

As the engineering field of conductive energy transfer to road vehicles is relatively immature, the simulation study presented here is not yet possible to verify experimentally as the infrastructure is not yet in place. Ideally, several vehicles of the same type, equipped with different powertrains as well as a significant amount of ERS should be in place in order to properly validate the simulation study.

The experimental setup used in order to verify the functionality of the powertrain featuring integrated energy transfer capability is also used to validate the meaning of galvanic isolation with regard to parasitic current.

1.5 Contribution

Besides the experience and personal development of the author, the contributions of this thesis are related to the develop knowledge concerning energy transfer from a conductive electric road to a moving vehicle and the control of energy flow on-board said vehicle. A more detailed list of the contributions of each chapter follows below.

- Chapter 2
 - Presentation of three different electric energy transfer systems where one features integrated energy transfer in a new way, capable of transferring high power.
- Chapter 3
 - Modelling of the on-board energy flow between the ERS, traction drives and energy storage. Modelling of common mode currents in a charging system due to parasitics and topology.
- Chapter 4
 - Development laboratory setup consisting of a complete electric powertrain (except energy storage) with integrated charging capability. Proof of functionality with regard to dynamic behaviour when connecting/disconnecting the different supplies (see Chapter 2 for more details), charging efficiency and parasitic current.
- Chapter 5
 - Firstly is the experimental results gathered in Ch. 4 post processed and turned into models for use in vehicle simulations. Further, this chapter presents the result of the vehicle simulations on a system level where the operational cost, in terms of energy consumption and battery degradation, of operating a vehicle on a conductive ERS is presented.
- Chapter 6
 - An analysis of common mode currents in a charging system with regard to an isolated/non-isolated approach.

1.6 Disposition

This thesis can be divided into two major parts, one which is modelling and simulation and the other is experimental validation. In turn, the former can be divided into two parts that are, 1) system level modelling of a whole vehicle with a time constant in the regions of hundreds of milliseconds and, 2) modelling of a charging system on power electronic level with a time constant in the region of nano to microseconds.

The two parts mentioned above are partly mixed among the chapters according to the following structure. Chapter 2 and 3 presents the concept and modelling of dynamic energy

transfer both on the ERS side and on the vehicle side and Chapter 4 continues to present the experimental setup and some of the measurement result (which is not directly related to Chapter 5 or 6) whereas Chapter 5 and 6 both present measurement and modelling result and following discussion.

Chapter 7 concludes the thesis and suggests areas where further research should be focused on.

Chapter 2

System solutions for conductive dynamic energy transfer

Allowing energy transfer from a conductive electric road system is associated with a safety risk and precautions must be taken with regard to the on-board charging system. The ERS is in this case assumed to be galvanically separated from the grid, as illustrated in Fig. 2.1-2.2 by an isolated AC to DC converter, with its minus pole connected to protective earth. The potentially harmful situation is if an isolation fault between the traction voltage system (TVS) and the chassis of the vehicle should occur whilst connected to the ERS. The term TVS is used to refer to the electrical components connected to the high voltage DC bus on-board the vehicle. The chassis of the vehicle could then be put on dangerous potential with respect to ground, see Fig. 2.1 where the TVS is illustrated as one single load between the two poles of the ERS. A grounded human being would, if in contact with the chassis, create a path for a potentially harmful current.

One way of mitigating the risk of creating a harmful situation is to double isolate all of the equipment connected to the TVS, meaning that two independent isolation faults have

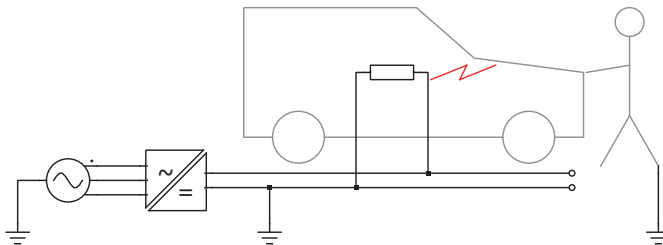
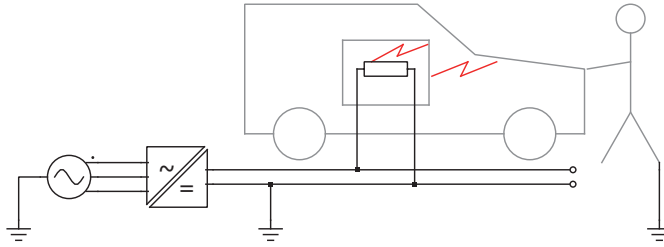
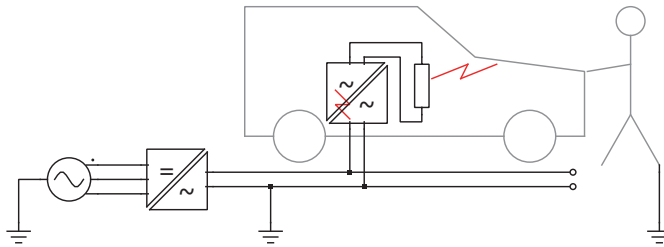


Figure 2.1: Illustration of how an isolation fault on-board a vehicle can incur a, for living beings, harmful situation.



(a) Double isolation of the entire TVS illustrates two independent isolation faults are required to put chassis on harmful potential.



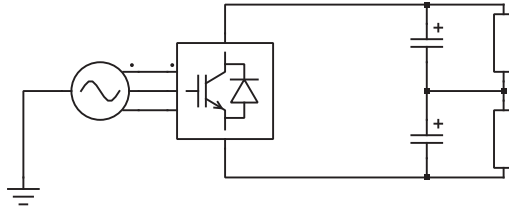
(b) An isolated DC-DC converter is installed as an interface between the ERS and TVS which would require two separate isolation faults in order to put the chassis on dangerous potential.

Figure 2.2: Safety precautions to be taken when a vehicle is galvanically connected to a grounded charging supply with no protective earth connected to the chassis.

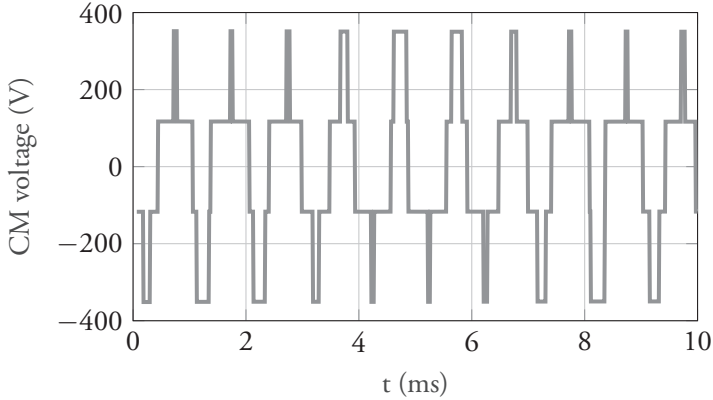
to occur in order to put the chassis on potential with respect to ground, as illustrated in Fig. 2.2a. As isolation faults can be detected with proper equipment on-board the vehicle, it is deemed that double isolation is an acceptable way of reducing the risk of any dangerous situation to arise. Fig. 2.2a illustrates the TVS as a single load which is 'contained' in an extra layer of isolation, in reality, the extra isolation layer must also include the current collector, i.e. *every* component of the vehicle connected to the ERS.

A third method to mitigate the risk is to galvanically separate the ERS, which is minus pole-grounded, from the TVS, which then will float with respect to ground. Just as in the 'double isolation method', two independent isolation faults would be required in order to put the chassis on a dangerous potential with respect to ground. One difference to the former scenario is that one isolation fault would have to occur within the DC-DC converter, as shown in Fig. 2.2b.

In practice, if adopting the method of installing an isolated DC-DC converter, all of the components 'up stream' of the isolation transformer (within the DC-DC converter) would also have to double isolated, which would mean the current collector, cabling and the



(a) Basic layout of a grid connected converter.



(b) Common mode voltage of a 700 volt DC-link with respect to ground while charging from a grounded grid.

Figure 2.3: The mid (common) point of the DC-link in (a) fluctuates with respect to ground as shown in (b) with a grid connected two-level converter.

DC-DC converter itself. When galvanically isolating the TVS from the charging supply, not only is a level of safety added, but it also eliminates the path for parasitic currents due to parasitic capacitances on-board the vehicle. This parasitic current arises due to the switching converter which creates a common mode voltage fluctuation of the DC-link, as illustrated in Fig. 2.3. In turn, the fluctuating common mode voltage can generate current through parasitic capacitances to ground. When statically charging, as protective earth is connected to the vehicle, this parasitic current might trip RCD-breakers and similar. This can become an issue especially if the TVS is physically large, as it might be in heavy vehicles, as components such as cabling, battery pack and so on increase in physical size. Shielded cables can be seen as a radial capacitor between the main lead and the shield and the longer the cable, the higher the capacitance. Similarly, if the battery pack is physically large, the area of which conducting material carrying different charge is increased, i.e., increasing the capacitance.

In this thesis, three different charger topologies/electric powertrains are considered, each of them with an individual approach to galvanic isolation and/or double isolation. Since a specific charging solution should not be limited to only allow energy transfer from an ERS, static AC-charging should also be made possible. As the powertrain on-board the vehicle consists of the components both responsible for traction (energy flow to/from the

wheels to/from the battery and/or the ERS) and charging (energy flow to the battery from the ERS or grid) these components are hereinafter referred to as an Energy Transfer System (ETS). Common for all ETSs considered are that two separate traction drives (machine and inverter) are used for all of them. This is due to, 1) it is of necessity in one of the ETSs, see Sec. 2.3, and 2) since the type of vehicles part of the study in this thesis require a relatively high traction power, it is deemed not unlikely, due to scalability, that a manufacturer chooses two medium sized traction drives rather than one which alone provides the full traction power requirement.

When considering vehicles supplied by a conductive ERS, which in several ways are similar to a catenary system that has been in use for many years in train, tram, and trolley bus applications, an input LC filter on the DC-link is often required in order to limit current and stabilise the voltage [42]. The on-board DC-link voltage on a bus supplied by a conductive ERS is presented in [43], which gives an insight to supplied voltage quality. This publication shows the voltage at the current collector, i.e., 'before' the installed LC-filter and due to the passive rectification of the grid voltage, an AC component is present on top of the DC voltage, something that to some extent is reduced by the LC-filter. The systems considered in this thesis require a similar filter should the voltage behave the way as described. However, the filter required is deemed to be similar in all three systems elaborated on below, which is why this aspect is left out of the analysis.

A detailed explanation of each ETS considered in this thesis follows below.

2.1 High power Separate Energy Transfer System, HSETS

A combination of what is shown in Fig. 2.2a and 2.2b on a more detailed level is shown in Fig. 2.4 where the extra layer of electrical isolation is illustrated by the dashed line. Since

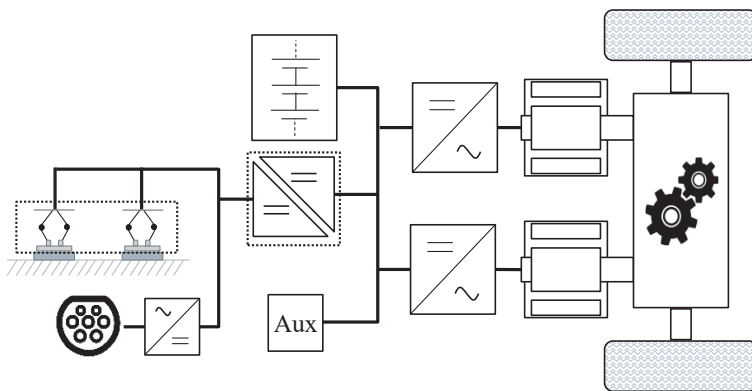


Figure 2.4: An ETS with ERS and AC energy transfer enabled with an isolated DC-DC converter galvanically separating the charging supply and TVS. The dashed line illustrates where an extra layer of isolation is required.

the current collector and (the primary side of) the DC-DC converter are connected to a grounded potential, these components are required to carry this extra layer of isolation as well. The rest of the TVS, i.e., the energy storage, traction drives and auxiliaries, are consequently not required to be doubly isolated. As shown to the left of the DC-DC converter in Fig. 2.4, there are two inputs, the top one illustrates the current collector when charging from an ERS whereas the lower one illustrates a 'Type 2' cable inlet [44], normally used when statically charging from an AC-outlet. As an interface to the AC-grid an active front-end, a non-isolated AC-DC converter, is connected in between the inlet and the isolated DC-DC converter. When utilizing the static AC-charging, protective earth is connected to the vehicle, meaning the isolated DC-DC converter *could* be bypassed and the active front-end could be connected directly to the battery since an isolation fault is easily detectable. However, as mentioned above, it is still advantageous to galvanically separate the TVS from the supply due to parasitic currents that may trip the equipment connecting the vehicle to the grid, and on-board chargers from AC normally contain a galvanic isolation interface.

With regard to Fig. 1.1 and considering energy transfer from the ERS, the grid and rectification (Fig. 1.1(a)-(b)) are off-board the vehicle, whereas the high frequency inverter, transformer and rectification and current control (Fig. 1.1(c)-(e)) is contained within the DC-DC converter.

It is obvious from the design of the ETS that the isolated DC-DC converter has to be rated in such a way that all of the energy consumed by the vehicle has to be supplied by the DC-DC converter. In turn, this requires the DC-DC converter to be rated at a relatively high power and therefore becomes a high-cost device of the ETS. Hereinafter, this type of ETS will be referred to as a High power, Separate, Energy Transfer System, HSETS.

2.2 Low power Separate Energy Transfer System, LSETS

Fig. 2.5 shows an ETS with an isolated DC-DC converter but also with a switching device allowing the traction drives to be supplied directly from the ERS, bypassing the DC-DC converter. Similar to the HSETS, the current collector and DC-DC converter are double isolated while the rest of the TVS is not. The concept of this ETS is that as long as the vehicle is travelling below a certain speed, the switch is configured in a way that connects the traction drives to the DC-DC converter, making the TVS galvanically separated from the ERS. Above a certain speed however, the switch is reconfigured so that the traction drives are supplied directly from the ERS. The reason is that as the vehicle is travelling at a high speed, a person is not likely to come in physical contact with the vehicle and a lower level of safety can be accepted. At low speed however a higher level of safety is achieved.

With regard to the stages of energy transfer to an EV, Fig. 1.1, all of the stages are at all times included when considering energy transfer to the *battery*. However, as energy transfer to the *wheels* is separated from the energy transfer to the battery at high speed only Fig. 1.1(a)-(b) is part of the energy transfer to the wheels.

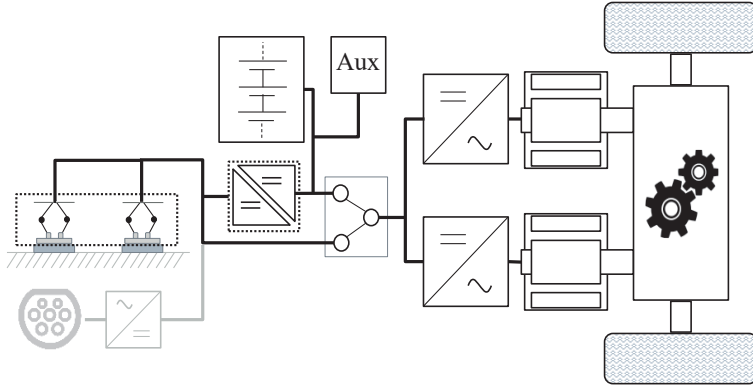


Figure 2.5: An ETS with a low power, isolated, DC-DC converter and a device allowing the traction drives to be supplied directly from the ERS - a switch box. The dashed line illustrates where an extra layer of isolation is installed. The AC interface is greyed out as it is only relevant when the switch is configured to its upper position.

The switching device allows for a DC-DC converter rated at a lower power level than the HSETS as the DC-DC converter only has to supply the energy required by the vehicle travelling at low speed. At high speed, the DC-DC converter is still connected so that charging of the battery all the while is possible. Hereinafter, this type of ETS will be referred to as a Low power, Separate, Energy Transfer System, or LSETS.

2.3 Fully Integrated Energy Transfer System, FIETS

Integration in terms of charging of electric vehicles, is widely documented in literature [45], [46], [47], [48], [49]. Not uncommonly an 'integrated charger' is aimed at static AC-charging where the motor windings are utilized as line filter and the machine converter is treated as an active rectifier, or non-isolated charger. This is made possible by switchgear allowing the motor windings, converter, and grid connection to be configured in such a way, as shown in [40]. Other topologies with multiphase (more than three) machines and converters have also been shown [46], [50], [51]. Typically, the integrated charger topologies published in literature are either - or both - relatively low power or does not feature galvanic isolation between the charging supply and the on-board TVS. The reason mainly being that they are aimed at static AC charging where protective earth can be presumed to be connected.

As shown in the HSETS and LSETS, both comprise an isolated DC-DC converter. Should one want to eliminate the DC-DC converter from the ETS due to cost and/or physical space reasons, a topology shown in Fig. 2.6 could be used. The DC-DC converter is in this case 'replaced' by a device allowing each of the inputs (energy storage, ERS or active front-end) to connect to either of the traction machines. The idea is to use the traction machines as the isolation interface between the charging supply and the TVS instead of

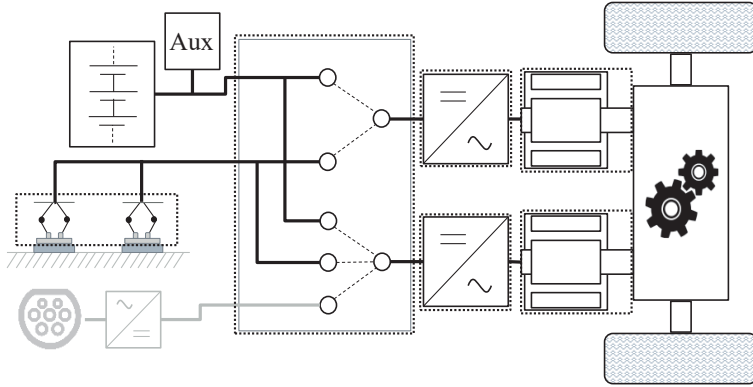


Figure 2.6: An electric powertrain with integrated charging capability, where the isolated DC-DC converter can be omitted. The AC interface is greyed out as it is only relevant when the upper switch is configured to its upper position and the lower switch is configured to its lower position.

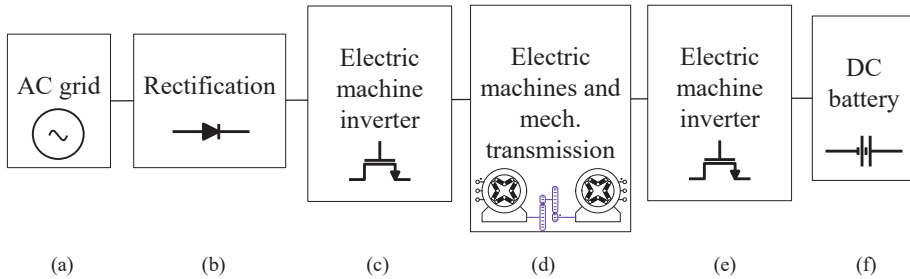


Figure 2.7: The principal stages of supplying electrical energy to the battery with the FIETS.

parts (c)-(e) in Fig. 1.1 as illustrated by Fig. 2.7. Therefore, both machines, including converters, and switchgear has to be double isolated towards the chassis of the vehicle as any of them can be connected to ERS potential. Energy is transferred from the charging supply to the energy storage by connecting one of the machines to the ERS or active front-end whilst the other machine is connected to the energy storage. By running the former machine in motoring mode and the latter in regeneration mode, energy is transferred from the supply to the energy storage with a galvanic isolation interface in between *without* the need of an isolated DC-DC converter with only the addition of components with low complexity. In order to be able to charge while the vehicle is at standstill, the mechanical transmission is required to feature a neutral gear whilst the machines are still mechanically coupled. Charging while the vehicle is moving is possible as long as the tractive power requirement is lower than what one machine alone can provide, as illustrated by Fig. 2.8 where

$$P_{ERS} = P_{traction} + P_{Bat} \quad (2.1)$$

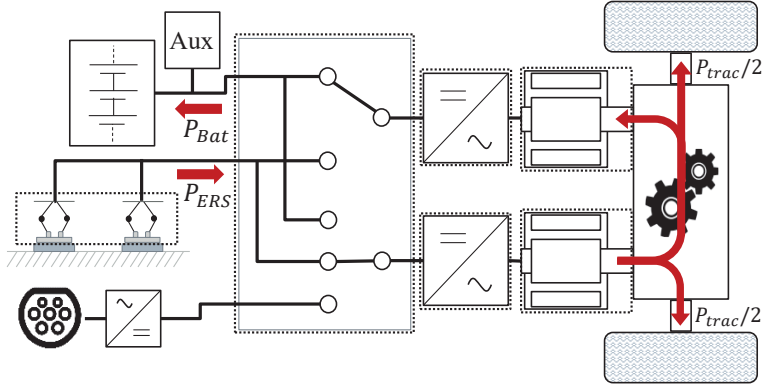


Figure 2.8: An electric powertrain with integrated charging capability, where the isolated DC-DC converter can be omitted.

and

$$P_{Bat} = \max(P_{em,max} - P_{traction}, 0) \quad (2.2)$$

where $P_{em,max}$ denotes the maximum rated power of one individual machine. For thermal management it is naturally possible to interchange which of the machines that are connected to the ERS and consequently operates at the higher power level of the two.

Should the traction power requirement exceed the rated power of the one machine connected to the ERS, the second machine will instead assist in propelling the vehicle. If the vehicle is in such a state that charging of the battery is not necessary, both machines can be connected directly to the ERS in order to minimize conversion losses, which naturally are higher in this topology than in the HSETS and LSETS.

Given the design of the ETS, it is required by the switchgear to be able to change state rapidly and seamlessly while the vehicle is in motion. For instance, assuming that the vehicle uses both traction machines for propulsion, drawing power from the battery, and approaches an ERS with the intent of switching over one of the traction machines to ERS supply for charging the battery. This means that a sequence of events must be performed for one or both machines according to the following,

1. reduce the stator current to zero in the traction machine to be switched from battery to ERS supply,
2. disconnect the related traction converter from the original supply,
3. adjust the voltage of the DC-link so that it matches the new supply,
4. connect to the new supply,
5. ramp up the stator current,

all within the approximate time a normal gear change would take, meaning less than one second. The voltage of the DC-link is adjusted by either supplying a small amount torque to the output shaft, i.e., taking energy from the DC-link capacitor, or by regenerating a certain amount of energy from the moving vehicle, i.e., feeding energy back to the DC-link capacitor.

Hereinafter this type of ETS will be referred to as a Fully Integrated, Energy Transfer System, or FIETS.

2.4 ERS

The details of the conductive electric road system are not a part of this thesis. It is treated as a voltage source seen from the vehicle. However, certain aspects, as where to place the ERS along a certain stretch of road is investigated here as it is deemed as important from an energy consumption perspective as the vehicle ETS topology. Below, two different proposals as to where to place a certain ERS section as well as how long each section should be is presented.

2.4.1 Equal distance, 'EQU'

A pragmatic approach to placing the ERS sections is to place sections of equal length, an equal distance apart, along a certain stretch of road. In order to clarify, two parameters are introduced.

- k_{ers} , describing the relative coverage of ERS along a certain stretch of road,
- d_{ers} , describing the absolute distance between the start of two consecutive sections of ERS.

In order to define k_{ers} , another parameter is introduced, s_{ers} which is the length of the equally long ERS sections, as illustrated by Fig. 2.9. The relative ERS coverage, k_{ers} is thus defined by

$$k_{ers} = \frac{s_{ers}}{d_{ers}}. \quad (2.3)$$

This method of deciding where the ERS sections is placed does not take characteristics of the drive cycle/road into account. Hereinafter, this method of placing the ERS sections along a stretch of road will be referred to as the Equidistant (EQU) method.

2.4.2 Power dependant, 'ADA'

As opposed to what is described above, one could argue that the ERS sections should be placed based on the traction power requirement, i.e., place the ERS sections at locations where vehicles typically accelerate for a significant amount of time, along up hills and so

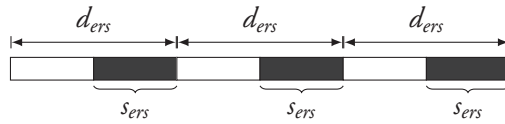
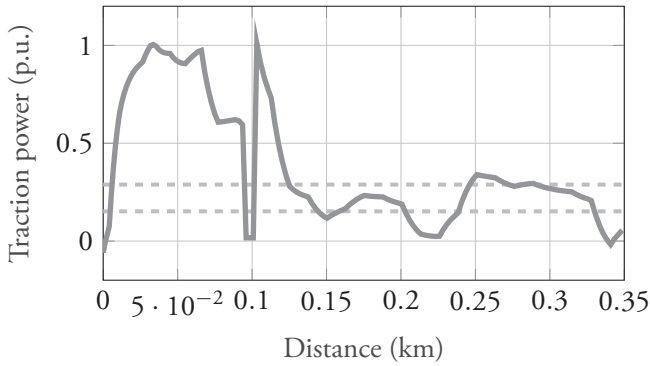
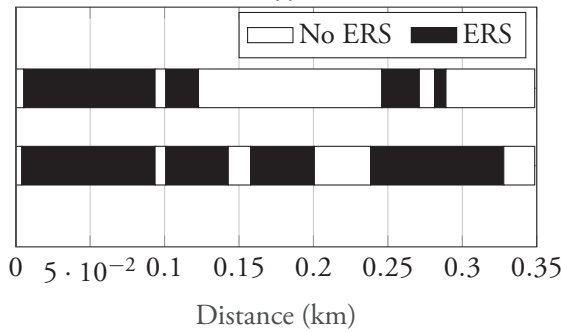


Figure 2.9: ERS characteristics



(a)



(b)

Figure 2.10: Traction power requirement (a, solid line) and two levels of constant power (a, dashed lines). Final ERS placement shown in (b), where the higher constant power level in (a) corresponds to the upper 'road' and vice versa.

on. Consequently, this requires significant knowledge about the certain stretch of road beforehand, in order to assess where each ERS section should be placed. In the context of drive cycle simulations, as is the case with this thesis, the exact locations as to where to place the ERS sections is deduced by running a simulation with the specific vehicle with an unrealistically large capacity battery and by post processing the required traction power at every instance in time. The ERS section is placed where the traction power exceeds a certain power level. In order to adjust the total ratio of ERS coverage along the drive cycle, the 'threshold' power level is adjusted accordingly; higher or lower. An illustration of how the traction power requirement determine where the ERS sections are placed is shown in Fig. 2.10 where only two levels of constant power levels are shown for clarity. In reality,

a minimum ERS section length, as well as a minimum distance between ERS sections, is defined in order to eliminate unrealistically short ERS sections or gaps between sections.

The reason for investigating this type of approach to placing the ERS sections is based on the assumption that if the energy supplied by the ERS is more or less directly consumed for traction purposes unnecessary conversion is avoided. The effect should be especially prominent in the ETSs with the ability to supply the traction machines directly from the ERS.

Hereinafter, this method of placing the ERS sections along a stretch of road will be referred to as the (Traction power) Adapted (ADA) method.

2.5 Chapter summary

This chapter elaborates on the importance of double isolation and/or galvanic isolation of the TVS on-board a vehicle aimed at utilizing energy transfer from an ERS. Three different layouts of the on-board electric architecture is presented, referred to as an Energy Transfer System (ETS). The system is not called charging system as it is in this case responsible for energy transfer from the ERS to both the battery and driven wheels, as well as there in between. Two the ETSs feature a DC-DC converter, acting as an interface between the ERS and the TVS whereas the third features integrated energy transfer capabilities, meaning components primarily utilized for traction purposes are also utilized in the transfer of energy from the ERS to the battery.

Furthermore, two different philosophies with regard to where to place the ERS sections along a certain stretch of road is presented. Either sections of equal length are placed equidistantly apart, or instead, the power requirement of the vehicle can be taken into account and hence, place the sections where the power requirement is high. The idea of the latter is that conversion losses can be lowered if the electrical power is used immediately instead of being intermittently stored in the battery.

Chapter 3

Modelling

Modelling of physical systems serves several purposes, among which cost and time saving are of essence. By modelling a complex system with a suitable tool (modelling and simulation tool in this case), the effect of altering the ingoing components for example can possibly be done within minutes or hours, compared to possibly weeks, months, or years in the physical system. As it is compelling to model systems and draw conclusions based on the outcome of simulations, one always has to remember that 'All models are wrong, but some are useful' [52], meaning that modelling can only take you so far.

This chapter covers the modelling of the whole vehicle with which the drive cycle simulations are run and also the modelling of the charging system on a more detailed level in order to investigate parasitics effect on common mode current.

3.1 Vehicle/ETS modelling

The vehicle model is a development of what is published in [53], [54], [55] adapted for dynamic energy transfer. The model is run with a frequency of 5 Hz, implying that the

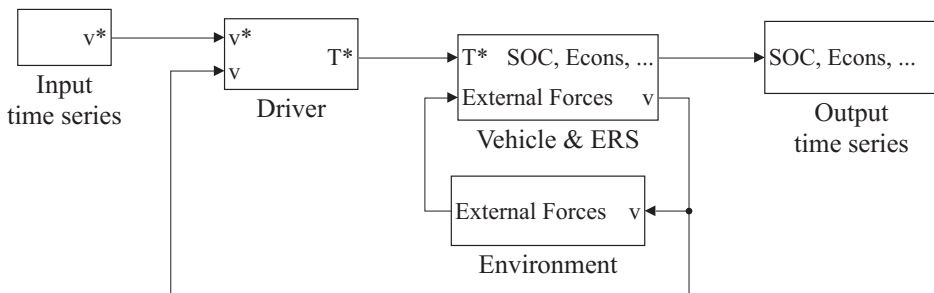


Figure 3.1: A simplified block diagram of the basics of the vehicle simulation model.

electrical system is modelled on a power and energy level, i.e., not voltages and currents in order to increase simulation performance.

The modelling of the vehicle and energy transfer on-board the vehicle can be divided into two major parts; modelling of the physical system such as vehicle Newtonian dynamics and the electromagnetic dynamics of the electric traction machines, and the modelling of the control of the power and energy flow. The former is generally modelled with mathematical expressions or by look-up tables, whereas the latter generally is modelled with state machines using Stateflow [56]. A simplified overview of the vehicle model is shown in Fig. 3.1 where the input time series consists of several arrays, such as time, vehicle reference speed, slope of the road, etc. The input is fed to the driver model which references the vehicle model with a requested torque in order to keep the speed error small. The 'Vehicle & ERS' sub model of Fig. 3.1 is naturally the most significant part of the model, containing the control modelling with regard to energy flow and also all the models related to energy transfer, i.e. DC-DC converter, traction drives, mechanical transmission, etc. Based on the speed, the vehicle is also subjected to a number of external forces, as illustrated by the 'Environment' sub model. The output time series consists of everything that might be of use when analysing the result, i.e., traction drive power, SOC, energy consumption, actual vehicle speed, etc. A detailed explanation of the different major parts of the vehicle follows.

3.1.1 Vehicle dynamics

The physical vehicle is modelled as a point mass, subjected to a number of forces. The vehicle has one degree of freedom along which all the forces also act, as is illustrated in Fig. 3.2. The force F_1 is always directed in the opposite direction with regard to the direction of travel, indicated by v , and consists of several forces:

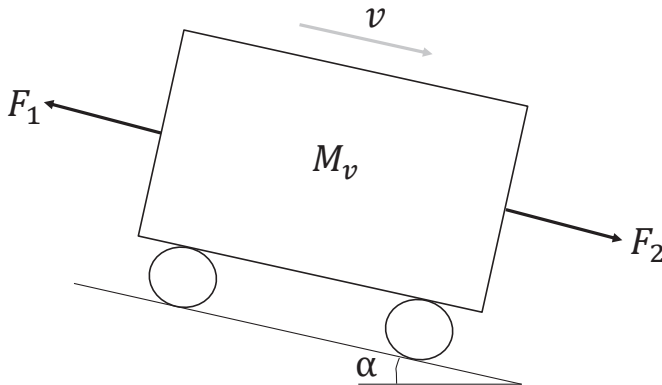


Figure 3.2: The mechanical dynamics of the vehicle model, with a mass m , travelling with a velocity v , on a road with a slope α , exposed to forces, F_1 and F_2 .

$$F_1 = F_{air} + F_{roll} + F_{brake} \quad (3.1)$$

whereas

$$F_2 = F_{traction} + F_{slope} \quad (3.2)$$

which can be directed both in the same direction as the direction of travel as well as in the opposite direction. The terms of Eq. 3.1 equals

$$F_{air} = \frac{1}{2} \cdot \rho_{air} \cdot C_d \cdot A_v \cdot v^2 \quad (3.3)$$

where ρ_{air} (kg/m³) is the density of the air, C_d (-) the drag coefficient, A_v (m²) the cross sectional area of the vehicle seen along the direction of travel, and v (m/s) the speed of the vehicle. Furthermore,

$$F_{roll} = C_r \cdot M_v \cdot g \quad (3.4)$$

where C_r () is the rolling resistance constant, M_v (kg) the mass of the vehicle, and g (m/s²) the gravitational constant. Lastly, F_{brake} originates from the friction brakes which are actively controlled by the driver model whenever the electric machine(s) cannot provide the required braking power. The term $F_{traction}$ of Eq. 3.2, originates from the electric machines, which can both propel and brake the vehicle and where

$$F_{slope} = M_v \cdot g \cdot \sin(\alpha) \quad (3.5)$$

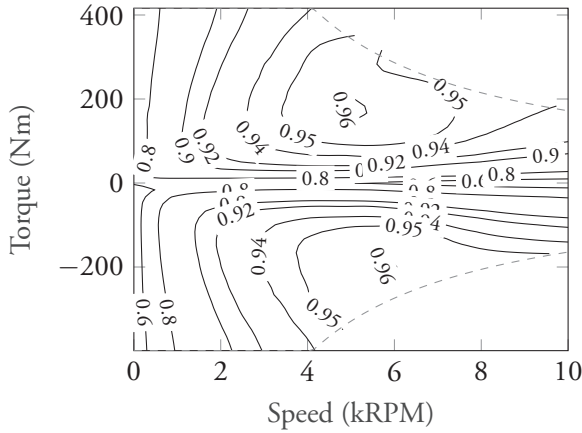
where α is the angle of the road with respect to the horizontal plane.

3.1.2 Traction drives and mechanical transmission

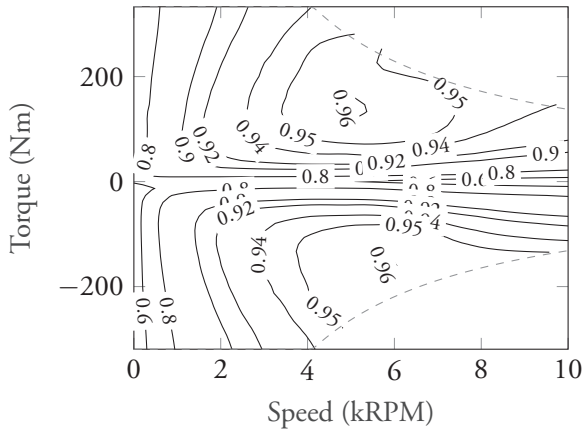
The efficiency of the traction drives, i.e., electric machine and its converter, is experimentally compiled from measurements on a mechanical transmission with two traction drives, see Chapter 4. An efficiency map of the traction drive, Fig. 3.3a, is produced, which in turn can be transformed to a loss map which is used as the model in the vehicle simulation.

Both the traction drives, and mechanical transmission is modelled by a two-dimensional map which has torque and rotational speed as inputs and loss as output. The loss of each traction drive and mechanical transmission is added to the total mechanical power they provide, adding up to the total electrical power used. Together with the distance travelled by the vehicle, the energy consumption can be calculated.

In order to evaluate traction drives at different levels of rated power, a new loss map adapted to a certain level of rated power can be created by adjusting the torque axis on the original efficiency map. This is illustrated in Fig. 3.3b where the torque-axis is reduced by a factor 0.8 from the original. This method is not perfect as the scaled traction drives are not based on measurements. However, they are expected to be accurate enough for the



(a) Efficiency of the experimentally verified traction drive.



(b) Altered y -axis in order to model a traction drive with 80% rated power of the experimentally verified traction drive.

Figure 3.3: Efficiency map of the machine including inverter. Dashed line shows the constant power limit.

purposes of this thesis as long as the scaling is reasonable. However, as this study is not focusing on whether different types of traction drives, as in PMSM versus EMSM versus IM, affect different aspects of performance it is desirable to keep the characteristics of the traction drive as similar as possible at different rated power levels.

The electric machine model also comprises a version of a thermal model in order to keep track of whether the machines are overloaded or not. The thermal characteristic of the machine is represented by a moving average filter which is fed with the instantaneous power of the machine, operating like a first order thermal model with constant cooling conditions. When the filtered value (the equivalent of temperature) exceeds 75% of peak power, the machine is deemed to be overloaded and continues to be so until the filtered

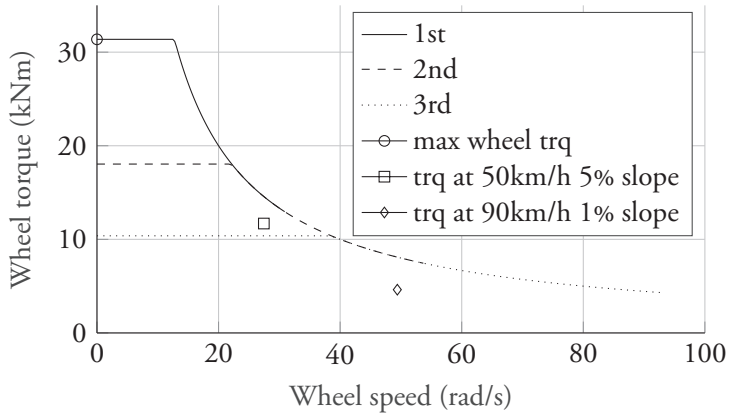


Figure 3.4: Traction requirement at different wheel speeds as well as torque and speed characteristics at different gear ratios.

power falls below 65% of peak power. The available power is, however, still unaltered even though the machine is deemed to be overloaded. The time constant of the filter is chosen to 300 s based on what is found in literature on thermal time constants of electric machines in automotive applications [57], [58]. Overloading could potentially become an issue in the FIETS as when transferring energy from the ERS to the vehicle, one of its traction drives are operating at a high-power level as both traction and charging power is supplied by this traction drive. The switch box enables the possibility to share the load between the traction drives as any of the two can connect to the ERS.

Depending on application, the mechanical transmission consists of two or three different gear ratios. The gear ratios are chosen according to a number of requirements:

- The vehicle is required to be able to, at low (walking) speed, climb a 16% slope,
- The vehicle is at a slope of 5% required to be able to maintain a speed of 50 km/h,
- The vehicle is at a slope of 1% required to be able to maintain a speed of 90 km/h.

The requirements are illustrated in Fig. 3.4.

3.1.3 Energy storage and auxiliaries

The energy storage is modelled as a Thevenin equivalent in which the series resistance is dependent on state of charge (SOC) and electrical power at the terminals, as proposed in [59], [60]. The pack is made up of a certain number of lithium-ion cells connected in series - a string - in order to reach a nominal voltage of approximately 800 V. The energy level is then altered by adding or removing a number of strings in parallel. The final number of cells in series and parallel equates to the final equivalent resistance. The efficiency of the whole pack at two different levels of capacity is shown in Fig. 3.5.

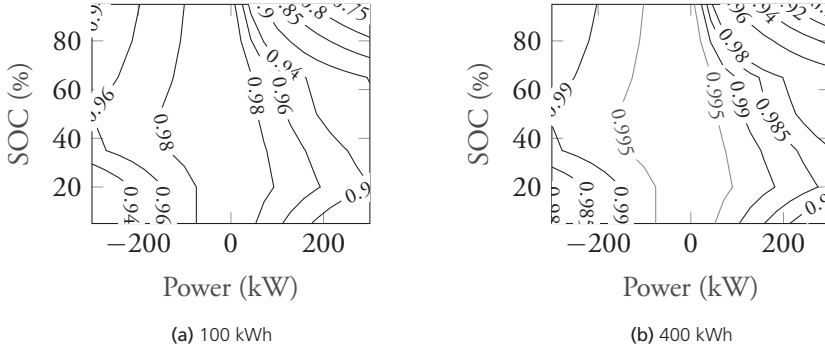


Figure 3.5: Battery efficiency at two different levels of capacity. Negative power indicates discharging.

As can be seen in Fig. 3.5, high charging power at high SOC generates a significant amount of losses, which is why a limit to charging as a function of SOC is introduced, shown in Fig. 3.6. with regard to the mathematical model of the energy storage, the battery power, P_{batt} , including losses are calculated as Eq. 3.6

$$P_{batt} = \begin{cases} \eta_{batt}(SOC, P_{term}) \cdot P_{term}, & P_{term} > 0 \\ \frac{P_{term}}{\eta_{batt}(SOC, P_{term})}, & P_{term} < 0 \end{cases} \quad (3.6)$$

where P_{term} is the power at the battery terminals and $\eta_{batt}(SOC, P_{term})$ is a 2D lookup table, as illustrated by Fig. 3.5. The container of energy is modelled with an integrator, where its initial condition is set to the assumed start value of the vehicles' SOC, as shown by Eq. 3.7

$$SOC = \int_0^{t_{end}} P_{batt} dt \quad (3.7)$$

As part of the performance evaluation of different ETSs and electric road placing, the battery degradation is evaluated by analysing the SOC time series after each drive cycle and counting the cycles the battery has been put through. This is done by a cycle counting

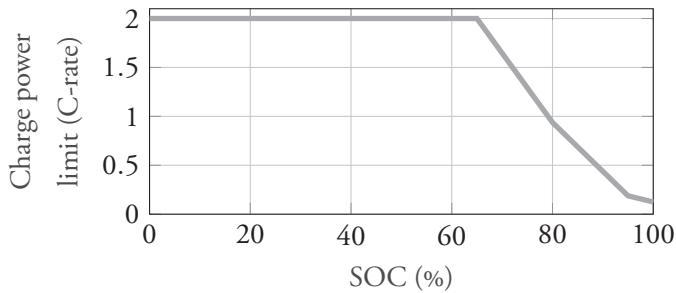


Figure 3.6: Charging power limit.

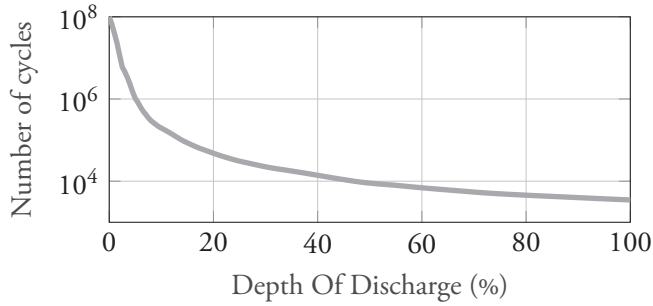


Figure 3.7: Relation between number of cycles and depth of discharge (DoD) of the battery. Used in order to estimate how much of the battery's life that is consumed.

algorithm stemming from fatigue analysis of materials [61], [62] and the data shown in Fig. 3.7 [63] where the number of cycles versus depth of discharge (DoD) is defined. There are several mechanisms that degrade a Li-Ion battery, cycling is just one. Also, the behaviour shown in Fig. 3.7, where the number of cycles are presented as a function of DoD, is different between different battery chemistries [64], [65]. In this thesis, however, the degradation is evaluated this way as it represents a good approximation of cycle life versus cycle depth of Li-Ion energy storage. It should also be noted that it is the comparison of how different ETSs and ERS characteristics affects battery degradation. Therefore, it is assumed that the batteries in the different constellation of ETS and ERS characteristics are affected the same amount by calendar ageing, storage temperature and so on.

The different vehicles are assumed to have different rating of auxiliary loads. In the case of a city bus depending on the environmental circumstances, the auxiliary load can be either reasonably low, or high, on par with the energy required for traction, e.g., to account for seasonal differences in the use of A/C. In this thesis, the auxiliary loads are lumped together and is seen as a constant consumer of energy, connected directly at the battery terminals. Different levels of auxiliary power are set in order to evaluate its influence of energy consumption and battery degradation.

3.1.4 DC-DC converter

The DC-DC converter is modelled as a power dependant efficiency, generating a certain loss of power depending on the power it supplies, see Fig. 3.8. The efficiency is based on reasonably recent publications covering either a specific topology of isolated DC-DC converters or review publications covering a multitude of DC-DC converters [66], [67], [68], [69]. SiC and GaN devices have not been considered due to devices utilizing these kinds of semiconductor materials are to a lesser extent available on the market as well as, if available, more costly compared to conventional Si devices. In order to be able to evaluate DC-DC converters at different levels of rated power, an unaltered efficiency curve is assumed regardless of rated power, similarly to how the traction drives are handled.

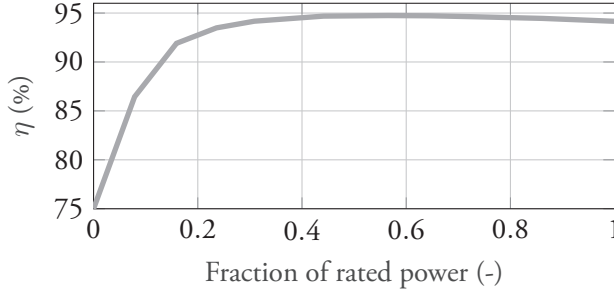


Figure 3.8: Efficiency of the DC-DC converter.

3.1.5 Energy consumption

The energy consumption, E_{cons} (kWh/km), of the vehicle is defined by

$$E_{cons} = \frac{E_{tot}}{s} \quad (3.8)$$

where E_{tot} is the total energy consumed by the vehicle during the drive cycle and s is the total distance travelled. The total energy consumed consists of

$$E_{tot} = E_{ERS} + \Delta E_{batt} \quad (3.9)$$

where E_{ERS} is the energy supplied by the ERS and ΔE_{batt} is the energy difference in the battery observed from the start of the drive cycle compared to the end of the drive cycle:

$$\begin{aligned} \Delta E_{batt} &= W_{batt} \cdot (SOC_{t=0} - SOC_{t=end}) + E_{loss,charging} = \\ &= W_{batt} \cdot (SOC_{t=0} - SOC_{t=end}) + (1 - \eta) \cdot W_{batt} \cdot (SOC_{t=0} - SOC_{t=end}) = \\ &= W_{batt} \cdot (SOC_{t=0} - SOC_{t=end}) \cdot (2 - \eta) \end{aligned} \quad (3.10)$$

As indicated by Eq. 3.10, in addition to the SOC swing of the battery is also the loss generated when restoring the SOC to its initial value included. This is true independent of the sign of ΔE_{batt} , i.e., the energy and related charging/discharging losses are compensating the total energy consumption of the vehicle. It is assumed that the SOC is restored by means of static AC charging. The efficiency used when calculating the losses related to charging differs between the ETSSs. The AC charging efficiency of the FIETS is based on the experimental measurements presented in Chapter 5, in particular the data presented in Fig. 5.2 which shows both AC to DC charging efficiency as well as DC to DC charging efficiency. The difference between these two is the inclusion of the conversion from AC to DC which is accomplished by an active front end converter. The same difference is added to the efficiency of the DC-DC converter model, shown in Fig. 3.8, used by the HSETS

and LSETS, in order to emulate charging from the AC grid. The maximum achievable efficiency is assumed, which might not be reasonable in reality as the maximum efficiency is reached at a relatively high-power level. Static charging from the grid is usually taking place at around the lower tenths of kilowatts. If the SOC is higher at the end of the drive cycle, the maximum efficiency of DC charging is assumed as the net increase of energy of the battery is achieved by the ERS, which is DC.

It should be noted, though, that if the drive cycle is sufficiently long, the ΔE_{batt} term of Eq. 3.9 becomes negligible compared to the E_{ERS} term, which is the energy supplied by the ERS.

3.1.6 Driver model and Power Flow Control

The input to the vehicle model - including driver model - is a time series containing vehicle speed set point and slope angle of the road, as per Fig. 3.1. The driver of the vehicle is modelled with a PI-controller with purpose to keep the speed error at a minimum. The output of the driver PI-controller is a torque reference sent to the vehicle model. Depending on ETS topology, the traction drives supply the requested torque within its limits as shown in Fig. 3.3. If a negative (braking) torque is requested which exceed what the electric machines can supply, the friction brakes assist in retarding the vehicle. The HSETS and LSETS, and when the FIETS is not connected to the ERS, the requested torque from the driver model is split between the two machines according to the following relation for positive torque:

$$T_{M1}^* = \min(T_{M1_{avb}}, T_{trac}^*) \quad (3.11)$$

$$T_{M2}^* = \max(0, \min(T_{M2_{avb}}, T_{trac}^* - T_{M1_{avb}})) \quad (3.12)$$

where T_{Mx}^* denotes the torque reference to each of the machines, T_{trac}^* is the traction torque referenced by the 'driver', and $T_{Mx_{avb}}$ is the available maximum torque at the current rotational speed, illustrated by the dashed line in Fig. 3.3. In words, Eq. 3.11 - 3.12 means that as long as one machine can sustain the torque referenced by the 'driver', that machine alone will supply the requested torque. Should the torque reference exceed the one machine's torque limit, the other machine is referenced with the remaining torque. Of course, which machine that is prioritized can be changed for thermal management purposes. Another way of distributing the torque between the traction machines is to at each operating point, i.e., speed of the vehicle, choose the combination of torque references that generates the least amount of losses. This control strategy is however not used in this study. As the traction drives are a part of the energy transfer system from the ERS to the battery as well as to the wheels in the FIETS, the distribution of torque is handled differently when the vehicle is connected to the ERS. Equation 3.13 illustrates based on what parameters the torque is distributed between the two machines. Based on charging requirement and the current

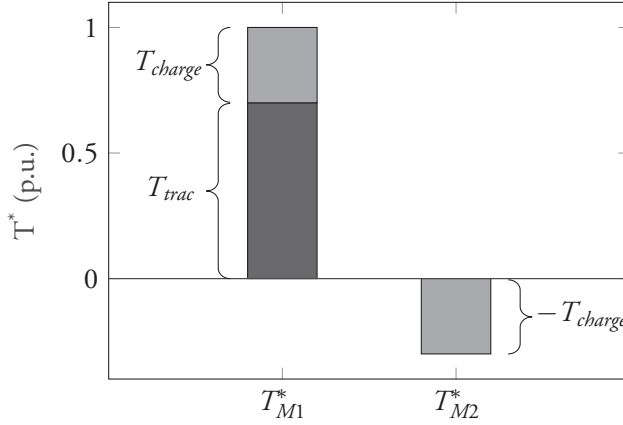


Figure 3.9: Illustration of torque distribution of the the two traction drives of the FIETS when driving and charging from an ERS.

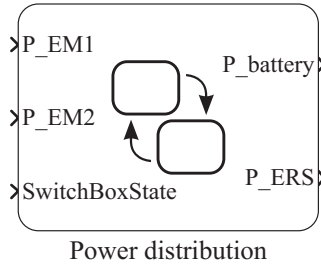


Figure 3.10: The switch box modelled with a Matlab Stateflow state machine.

traction requirement, the torque is distributed accordingly between the two traction drives, generally according to Eq. 2.1-2.2, see also Fig. 3.9.

$$\begin{bmatrix} T_{M1}^* \\ T_{M2}^* \end{bmatrix} = f(T_{traction}^*, P_{charge}^*, ERSavailable, SwitchBoxState) \quad (3.13)$$

The LSETS and FIETS comprise a device that allows the traction drives to, electrically, disconnect and connect to different sources of energy supplies; a switch box. In reality, the switch box connects the different inputs (ERS, battery, AFE) to the two traction drives. The model of the switch box, as illustrated in Fig. 3.10, is rather different as it could be interpreted that the power of the traction drives is fed to the battery and/or ERS. This is not the case but rather, based on ERS availability, the actual power of each traction drive is set equal to either supply. Hence, it is of necessity to limit the power of the traction drives to be within the limits of what the ERS and/or battery can provide/sink. As the switch box has a limited number of bi-stable states, it is conveniently modelled with a state machine.

In the FIETS, depending on mode of operation, the power consumed (or provided)

by the machines is fed from either, or both, supplies. The mode of operation is primarily defined by whether ERS is available or not; if ERS is not available both traction drives are connected to the battery. If ERS is available, generally one, or under certain circumstances both, traction drives are connected to the ERS depending on charging demand. If SOC is above a certain level and ERS is available, charging is not prioritized; the traction drives operate directly from the ERS in order to minimize conversion losses and reduce battery wear. Depending on the total auxiliary load, the battery will at some point eventually need to be charged whereupon the switch box reconfigures to feed power from the ERS. Another reason for reconfiguring the switch box is thermal management of the machines since, in a charging situation, one of the traction drives operates at a higher power level since that traction drive supplies both traction and charging power. When a machine is overloaded (see Section 3.1.2) the tasks of the machines are interchanged, i.e., the machine that was connected to the battery connects to the ERS and vice versa.

The purpose of the switch box in the LSETS differs somewhat from what is elaborated above regarding the FIETS. In this case, the purpose of the switch box is only to facilitate the connection of the traction drives to the ERS *whenever* ERS is available.

Yet another aspect that imposes reconfiguring of the switch box is whether the regeneration of braking power is to be made possible when the vehicle is connected to the ERS. Since it is assumed that the ERS cannot receive power, regeneration of braking power is not possible while the vehicle has its traction drives connected to the ERS. This can be mitigated by letting the switch box reconfigure whenever negative traction torque is requested so that the traction drives are connected to the battery in order to regain the kinetic energy of the vehicle rather than just generating heat in the friction brakes. Depending on the nature of the drive cycle, the number of switching events is expected to increase significantly, allowing the switch box to rearrange whenever negative traction torque is requested. This naturally has its implications on the lifetime on the switching devices. In this thesis the experimental verification is made with switches of a mechanical kind that do have a certain life expectancy. Notwithstanding this consequence, there is expected to be a trade-off between the positives of reducing the energy consumption due to enabling regenerative braking to a greater extent, and the negatives, reducing the lifetime of the switching devices. In order to compare the effect of regeneration of braking power while on an ERS, a control approach which will not reconfigure the switch box at negative traction torque requirement in order to minimize switching events as well as an approach that does just that will be investigated. Hereinafter these two control strategies will be referred to as:

- Minimum Switching Control, **MnSw**, which will not reconfigure the switch box at negative traction torque,
- Maximum Regeneration Control, **MxRe**, which will reconfigure the switch box at negative traction torque in order to minimize energy consumption.

In order to model the switching event of a traction drive from one supply to another,

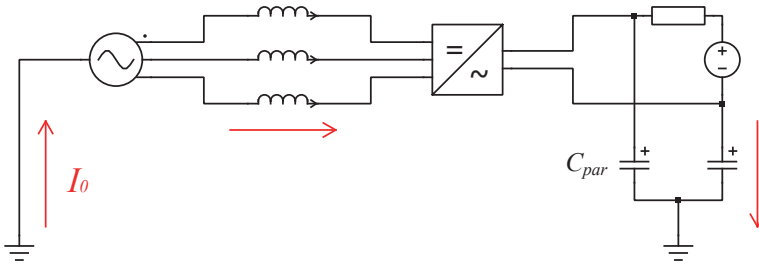


Figure 3.11: Non-isolated charger where the arrows indicate a possible galvanic path for common mode current due to the parasitic capacitance in the TVS.

an interruption of torque to the mechanical transmission, and further the wheels, of 0.6 s is introduced whenever this occurs.

3.2 Power electronics modelling

The different ETS solutions studied in this thesis all affect the separation of the two galvanic systems related to the ERS and the battery. It is thus of interest to understand how these interact from an electric dynamics point of view. This is the motivation of the part of power electronics modelling described in this section. In this section all three ETs presented in previous sections are not included but rather are these models based on the developed experimental setup of the FIETS. Besides being capable of isolated energy transfer, which is the main idea of the FIETS, the practical setup can easily be altered so that non-isolated energy transfer can be achieved, making it possible to compare how the isolation interface might affect certain aspects of the electrodynamics.

The charging system is modelled on a more detailed level than the vehicle and drive cycle modelling described in the previous sections. Here, the purpose is to quantify the impact of galvanic isolation between the charging supply and the TVS on-board the vehicle. The charging system is modelled in Matlab/Simulink with Plecs [70] which is an add-on for electronic, thermal, and mechanical modelling and simulation. A variable time solver is used, with an average time step size in the region of 1-100 ns depending on model complexity. A static AC-charging scenario is modelled where the FIETS, with its galvanic isolation approach, is compared to a non-isolated on-board charger. Both these approaches to static charging are validated experimentally, see Chapter 4. A summary of the electrical characteristics is shown in Table 3.1.

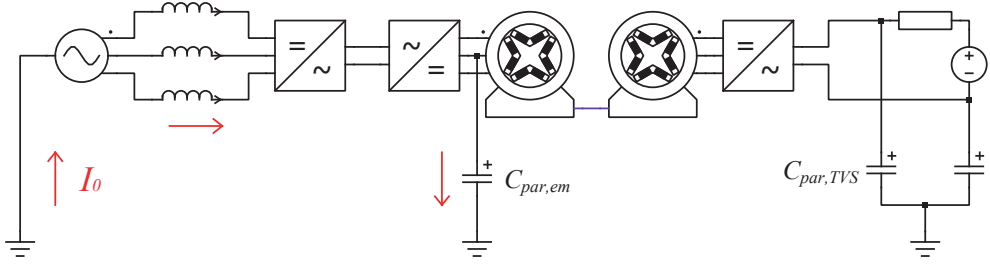


Figure 3.12: Isolated charger where the two machines breaks the circuit for the common mode current through the TVS parasitic capacitances.

Table 3.1: Electrical characteristics .

$C_{par,battery}$	100 nF/pole
$C_{par,em}$	7 nF/phase
$f_{sw,AFE}$	10 kHz
$t_{bt,AFE}$	2.5 μ s
$f_{sw,em}$	10 kHz
$t_{bt,em}$	2.5 μ s

The circuit of the following charging systems do not feature an earthed-minus pole system, such as elaborated on in Chapter 2 and shown in Fig. 2.1-2.2. Instead, the circuits shown here are based on the experimental setup developed of the FIETS.

A non-isolated charger solution is shown in Fig. 3.11 where the grid is illustrated by a three phase voltage source and the non-isolated on-board charger by an AC to DC converter. The TVS is reduced to only battery which is illustrated by a DC voltage source and a resistance. The parasitic capacitance is lumped together to one capacitor connected to each pole on the DC-link, closing the path for the common mode current. The common mode current originates due to the switching of the AC-DC converter, which makes the DC-link common mode voltage fluctuate with respect to ground with an amplitude equal to half the DC-link voltage, see Fig 2.3. In the experimental setup, the parasitic capacitance of the battery emulator is measured to approximately 100 nF per pole. Details on the battery emulator can be found in Appendix A.1.

In order to break the circuit for the common mode current a galvanic isolation interface is introduced in the shape of two back-to-back connected machines, see Fig. 3.12. Consequently, new parasitic capacitances are possibly introduced on the 'primary' side of the galvanic isolation interface. However, these are on a smaller scale than what is expected to observe in a physically large TVS on-board a vehicle. The parasitic capacitance of the electrical machine is measured between one of the phases and the chassis of the machine to approximately 20 nF, which would equate to approximately 7 nF per phase.

The detailed circuitry of the two different charging solutions is shown in Chapter 4 and Appendix A.4. The passive and active components of the circuits are available in the Plects library where the AC-DC/DC-AC converters are modelled by a three phase IGBT converter with data specified by the converter used experimentally, the 'Semikron SKAI 42 GD12' (all the converters are the same device in the experimental setup except battery emulator, see Chapter 4). The IGBT converter model can be specified with a certain forward voltage drop and conduction resistance in the IGBT and anti-parallel diode. Furthermore, if loss analysis is the objective, turn-on and -off loss and conduction loss can be specified. The machines are a permanent magnet synchronous machine specified as similarly as practically possible to the machines used in the experimental setup.

The control algorithms are implemented in the model in a similar fashion to what is implemented in the experimental setup. The control of the active front end converter (AFE) differs somewhat in the two different charging scenarios; in the case where it is used as a non-isolated charger, Fig. 3.11, it is current controlled since its output is connected to a voltage stiff battery model, whereas in the case where it is used as a DC-voltage source for one of the traction drives, Fig. 3.12, it operates in constant DC-voltage mode. In the latter case the DC-voltage control loop is an outer loop to the current control loop that are similar in both cases. Amplitude invariant Park transformation is used for transformation to the synchronous rotating frame whilst the current controller is a PI-controller with feed forward of the cross-coupling term and resistive voltage drop. The latter terms are shown in Eq. 3.14 and 3.15, displaying the direct and quadrature voltage components of a generic three phase load.

$$u_d = R_s \cdot i_d + L_{sd} \frac{d}{dt} i_d - \omega \cdot L_{sq} \cdot i_q \quad (3.14)$$

$$u_q = R_s \cdot i_q + L_{sq} \frac{d}{dt} i_q + \omega \cdot (\Psi_m + L_{sd} \cdot i_d) \quad (3.15)$$

where subscript d and q denotes the direct and quadrature components respectively. R_s (Ω) and L_s (H) is the stator resistance and inductance respectively whilst ω (rad/s) is the angular frequency and Ψ_m (Vs) is the linked flux. Furthermore, both cases utilize sinusoidal modulation with a switching frequency of 10 kHz and a blanking time of 2.5 μ s.

The grid voltage angle is pre-determined based on the angle of the source, i.e., the angle is not deduced on-line as is the case in a real application. The model can be fed with voltage from an ideal, three-phase, voltage source as well as a source supplying the measured no-load voltage. The no-load voltage is measured at the outlet supplying the experimental setup. This is done in order to observe how the imperfections of the grid voltage might affect the harmonic content of both differential and common mode current. The sampled, no-load, voltage and its harmonic content is shown in Fig. 3.13 where, particularly, a 5th and 7th harmonic is apparent. This kind of harmonic content likely originates mainly from rectification [71], [72] in the grid in the vicinity of the laboratory facilities.

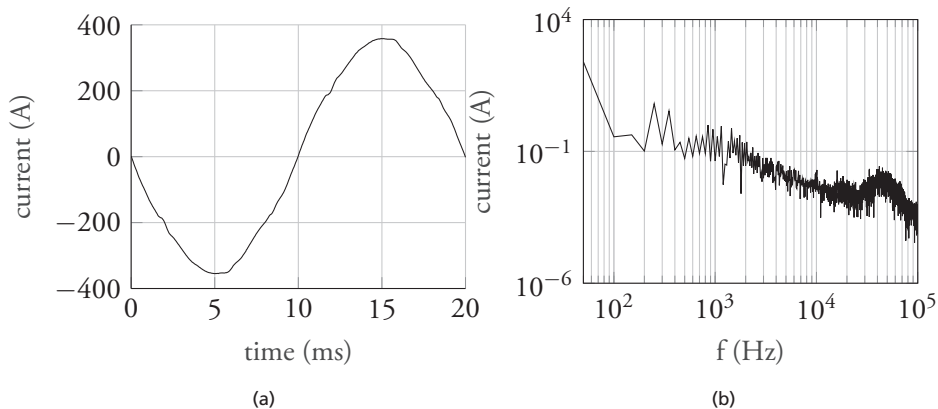


Figure 3.13: The real grid voltage, line to neutral, and its harmonic content.

The control of the two electrical machines shown in Fig. 3.12 consists of an inner current control loop and an outer speed control loop (only one machine operates in speed control). The current controller consists of a PI-controller with feed forward of cross coupling term (Eq. 3.14, 3.15) and resistive voltage drop. The switching frequency and blanking time is 10 kHz and 2.5 μ s, respectively.

The model of the inductance used between the voltage source and AFE, is based on the one used in the experimental setup. The inductance is dependant on the current, i.e., the inductance decreases with current. At the current levels investigated in this thesis, the cores do not approach saturation.

All the cabling of significant length in the model are modelled including a resistance and inductance per meter. Although, both Fig. 3.11 and 3.12 shows a return path of the common mode current through ground. This is not completely true as the return path, at least in part, is through the cable shield, which is not a perfect conductor. Due to the impedance in the cable shield, the common mode current flow in the shield may be reduced.

3.3 Chapter summary

This chapter presents the method of modelling the systems included in the vehicle analysis. This includes the major sub systems of the TVS; the electric machines and their converters, the energy storage and DC-DC converter, and so on. Furthermore, the different philosophies with regard to the control of torque and power on-board the vehicle is also presented.

In addition to the modelling of the vehicles and their related components, the power electronics related to the energy transfer from the grid to the battery is modelled in order to evaluate the impact of parasitic capacitance at the TVS.

Chapter 4

Experimental setup

4.1 Introduction

As two of the three different types of ETS (HSETS, LSETS), presented in Chapter 2, adapted for energy transfer from an ERS are considered the more conventional approach than the third (FIETS), the latter is the chosen one to be evaluated experimentally. Several aspects are of interest when evaluating these types of ETSs, the main points are stated below:

- Charging efficiency
 - DC to DC
 - AC to DC
- Dynamic behaviour when switching supply
- Common mode current

Besides the outcomes of the specific properties above, the tests also provide data for further analysis of the other two ETSs by obtaining an efficiency map of the electrical machine and its converter. This chapter firstly covers the design of the hardware in the experimental setup as well as tools used, followed by the software governing the control of converters and other systems. The result of the measurements is presented in later chapters in relation to where the outcome is used for further analysis.

4.2 Hardware

An overview of the experimental setup is shown in Fig. 4.1. Two active front end (AFE) converters are utilized as DC voltage sources where one is connected directly to the grid whilst the other is fed by an isolation transformer. The reason for the latter is that in order to emulate a battery, the supply is required to be galvanically separated from the grid.

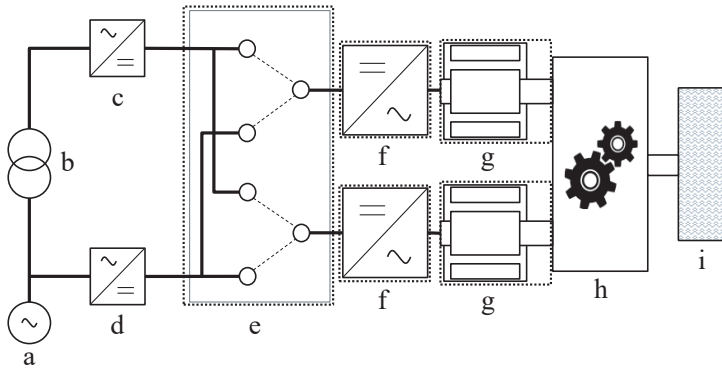


Figure 4.1: Block diagram of the experimental setup of the FIERS powertrain. The dashed line indicates an additional layer of electrical insulation.

Table 4.1: Details of the main components in the experimental setup.

	component	info
a	Grid connection	3 ~ 400V 63A
b	Transformer	ASEA, 380/330V, 180 kVA
c	Battery emulator/ AFE	Semikron SKiiP 513GD172-3DUL
d	Grid interface/ AFE	Semikron SKAI 42 GDI12
e	Switch box	LTH design
f	Traction converter	Semikron SKAI 42 GDI12
g	Traction machine	Commercial 180 kW Permanent Magnet Synchronous Machine
h	Mechanical transmission	Commercial heavy vehicle transmission
i	Flywheel	∅1000 mm, 610kg rotating mass

Two identical traction drives (converter and electric machine) are attached to a mechanical transmission suited for heavy vehicles. A switch box is installed between the AFEs and the traction drives, enabling the traction drives to independently connect to either supply. Mechanically, as shown in Fig. 4.1, additional electrical insulation is required of the switch box, the converters and the electrical machines. The practical implementation of this is shown in Appendix A.2. A list of the main components are presented in Table 4.1.

Each of the AFEs are installed in a separate cabinet with their own control equipment which is based on a National Instruments compactRio (cRio) [73] device. Another cabinet

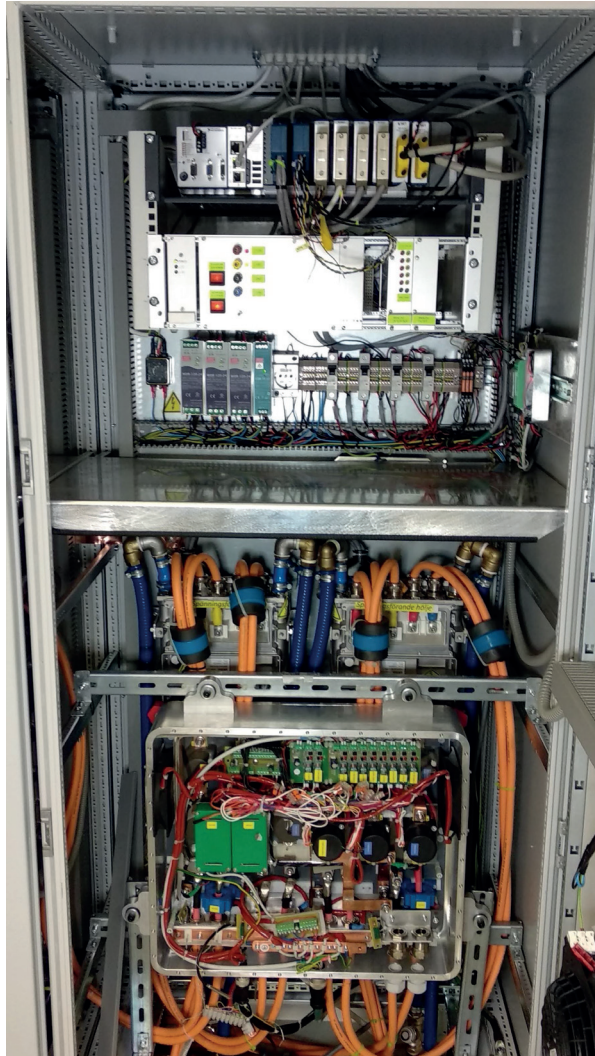
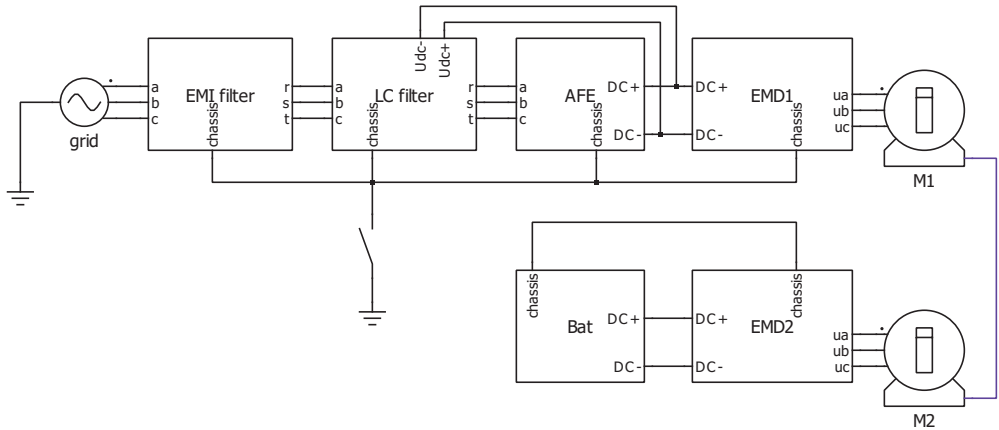
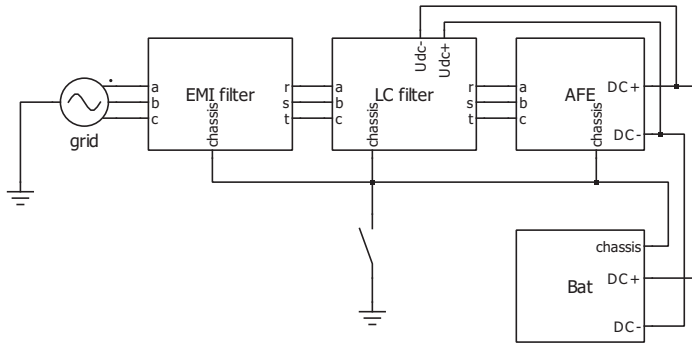


Figure 4.2: Electrical cabinet containing the switch box (lower part), the traction converters (behind the switch box) and control equipment (upper part).

is dedicated to the traction converters and switch box and their pertaining control equipment. Both traction converters and the switch box, are controlled by a single cRio unit equipped with appropriate I/O modules. The switch box contains 12 electromechanical switches in groups of three, one for each pole and one for the cable shield, making it possible to connect either of the traction drives to either of the supplies. The switch box also contains current and voltage measurement on all four of the inputs/outputs. In order to fully comply with the requirement that the converters, switch box and machines should be double isolated, as indicated in Fig. 4.1, the I/O signals between said devices and the



(a) The experimental setup in isolated energy transfer mode. The rightmost line indicates the mechanical connection between the electrical machines.



(b) The experimental setup in *non-isolated* energy transfer mode.

Figure 4.3: Simplified schematics of the experimental set up in isolated (a) and non-isolated (b) energy transfer mode.

cRio are optically isolated. The cabinet containing the switch box, traction converters and control equipment is shown in Fig. 4.2.

A block diagram of the electrical schematic of the experimental setup in both isolated energy transfer mode and non-isolated energy transfer mode is shown in Fig. 4.3. The circuit contains a switch that can connect the chassis of the components 'upstream' of the galvanic isolation interface to ground in order to be able to emulate a static charging scenario when, typically, protective earth is connected to the chassis of the vehicle. When said switch is open, the chassis of the filters, converters and electric machines are floating with respect to ground.

As shown in Fig. 4.3, two filters are installed in between the grid and the AFE, firstly an EMI-filter for attenuation of high frequencies and secondly a LC-filter for smoothing

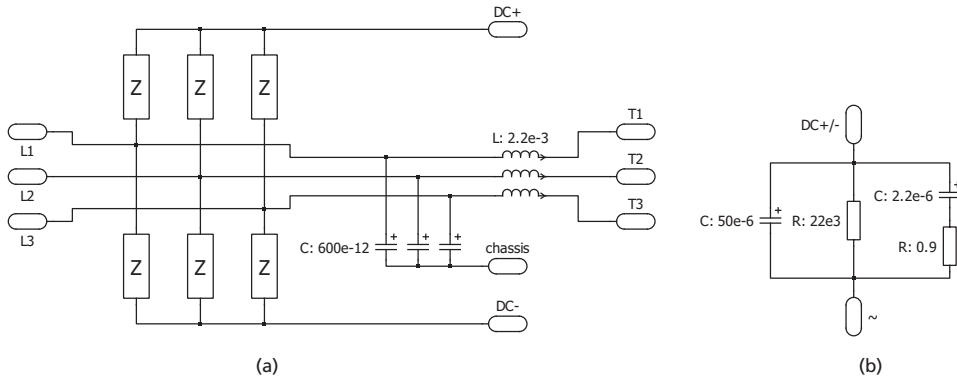


Figure 4.4: The LC-filter (a) with its Y-connected impedances with either pole of the DC-link as the start point, and the phase impedance (b), Z.

of the phase current and also lower the common mode voltage fluctuation of the AFE. The EMI-filter is a bought component (its schematic can be found in Appendix A.3) whereas the LC-filter is an in-house design, shown in Fig. 4.4. The chassis of both the EMI-filter and LC-filter are connected to the chassis of the AFE, referred to as the 'floating chassis'. The floating chassis is connected to the mid-point of the DC-link in the AFE (internally of the Semikron converter) by a capacitive/resistive voltage divider (see the schematics of the AFE and EMDs in Appendix A.4). The three 600 pF capacitors connected between each of the phases and the chassis of the LC-filter are not actual capacitors, but rather parasitic capacitances measured with a LCR-meter [74]. The purpose of the capacitive part of the LC-filter, Fig. 4.4(b), is to decrease the common voltage swing of the AFE which would force a common mode current through the parasitic capacitances. The star point of the phase impedances in Fig. 4.4 creates a virtual neutral point which when connected to the DC-link, +/- respectively, limits the common mode voltage and thereby also the common mode current. The purpose of the L-part of the LC-filter is to low-pass filter the phase current at, mainly, the switching frequency (10 kHz).

All of the converters in Fig. 4.1 except (c) and the electric machines are liquid cooled and in order not to create a galvanic connection between the devices a mineral oil is used as cooling media. An external pump is installed to maintain a constant flow and an oil-to-air heat exchanger is connected in series with all the devices in the cooling circuit. A fan mounted at the heat exchanger starts when the cooling media exceeds a certain temperature.

The mechanical transmission used is a commercial 'off-the-shelf' product intended for heavy vehicles with two input shafts and one output shaft. The gearing ratio of each of the inputs vs. output are 3.67 : 1 and 3.52 : 1 respectively.

A flywheel, Fig. 4.1(i), can be attached to the output shaft of the mechanical transmission in order to be able to transfer net energy from the grid to the output shaft. The mass is approximately 600 kg and both a friction brake as well as a retarder is used to brake its rotation if necessary. Not all experiments required the flywheel to be attached and a

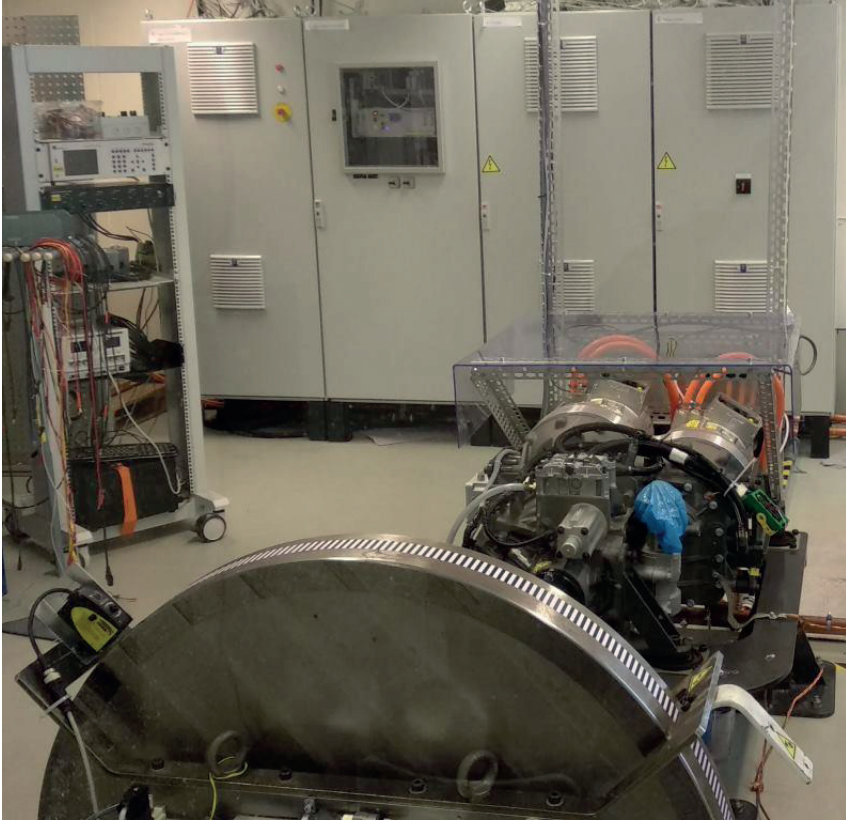


Figure 4.5: Overview of the experimental setup with the flywheel in the foreground followed by the mechanical transmission and electrical machines. In the background are the electrical cabinets containing governing safety system, power electronic converters and their control equipment and filters.

maximum rotational speed of approximately 700 rpm of the flywheel limits the use further. A photo showing the machines, gearbox and flywheel is shown in Fig. 4.5. Due to the limited maximum rotational speed, which is lower than the operational window of the retarder, stationary experiments with a significant amount of power supplied to the output shaft of the mechanical transmission is not possible.

The battery emulator is similar to the circuitry of the AFE and its filters towards the grid; the main difference being an isolation transformer that is connected in between the grid and the LC-filter and further the converter. See Appendix A.4 for a more detailed schematic.

4.3 Software

National Instruments (NI) compactRio (cRio) systems are used for all programmable logic in the experimental set-up. The cRio is based on an FPGA through which the I/O can be

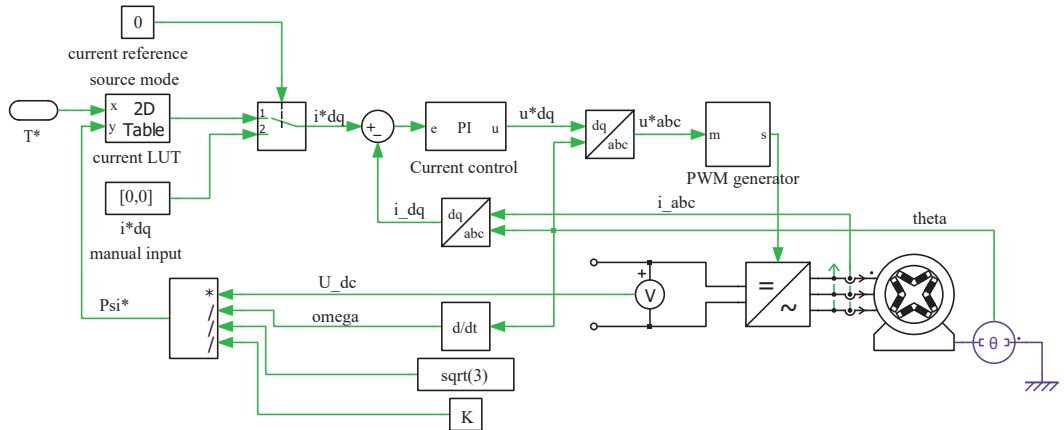


Figure 4.6: The control structure of the electric machines. The supply of the DC-link have been left out of the figure.

accessed. Further logic can be implemented on what NI refers to as the 'Real Time' unit which is suitable for less time critical tasks. A third level on which logic can be implemented is the user PC to which the cRio is connected, consequently the software running on the user PC should only be used for visualizing and observation. Signals can easily be passed through each of these three layers.

Each of the power electronic converters in the experimental set-up in this thesis work follows basically the same structure where the sampling of I/O channels, current PI-controller, and generation of PWM signals are implemented on the FPGA since these tasks are of high priority and time critical. Other functionality is generally implemented on the Real Time target. It should be noted that the control software of the AFEs is not implemented by the author of this thesis, therefore focus will be put on the control software of the electric machines and switch box.

4.3.1 Electric machine control

At the very lowest level of the motor control is a PWM-generator which use a carrier wave of 10 kHz and three reference voltages to create said PWM signals, see 'PWM generator' in Fig. 4.6. In turn, the reference voltages are generated by a vector current controller in the rotating reference frame. The current controller is a PI-controller with anti wind-up with regard to the available voltage on the DC-link. The starting point for tuning the gain in the proportional and integral parts of the PI-controller is based on methods available in literature [75], [76]. Some manual tuning is performed on top of the starting point in order to achieve an adequate response and stability of the current. Emphasis is put on stability rather than rapid dynamics due to the nature of the experiments.

In order to not only be able to control the machine by specifying the direct (d-) and the quadrature (q-) currents explicitly, further layers of outer control loops are added, as

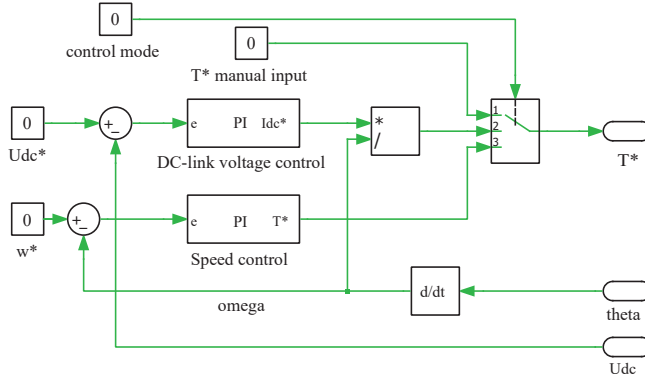


Figure 4.7: The DC-link voltage and speed control structure of the electric machines.

illustrated by Fig. 4.6-4.7. The torque control is an open loop control scheme where a requested torque is translated into a current combination of d- and q-currents by means of a look up table provided by the electric machine manufacturer. The look up table has two inputs, torque reference and stator flux linkage, Ψ , where the latter is estimated by the rotational speed, ω , and DC-link voltage, U_{DC} , and a constant, K , representing the safety margin so that overmodulation does not occur, see Eq. 4.1.

$$\Psi^* = \frac{U_{DC}}{\sqrt{3} \cdot \omega \cdot K} \quad (4.1)$$

A further outer loop is either the rotational speed control loop or the DC-link voltage control loop that are both closed loop PI-controllers, as shown in Fig. 4.7. The output of the speed control loop, a reference torque, is fed directly to the torque-to-current look up table whereas the output of the DC-link voltage controller is the reference DC-current at the DC-link capacitor. In order to specify a combination of d- and q-currents the DC-current reference has to be converted to a torque request as the torque-to-current conversion is always active in the control scheme. This is done by using the relation of power balance, see Eq. 4.2

$$I_{DC} \cdot U_{DC} = T \cdot \omega \Rightarrow T = \frac{I_{DC} \cdot U_{DC}}{\omega} \quad (4.2)$$

where the left hand side of the equation is the electrical, DC, power whereas the right hand side is the mechanical power. This relation is naturally only true if losses are neglected. In turn, this leads to that the output of the PI-controller should be multiplied by U_{DC} and divided by ω in order to obtain the reference torque. In the implemented control algorithm only the division of ω is performed, the operation is seen in between the 'DC-link voltage control'-block and the control mode switch in Fig. 4.7.

The speed controller consists of a PI-controller with feed forward of the torque request of the *other* machine (as the machines are counter-rotating, a sign conversion is not ne-

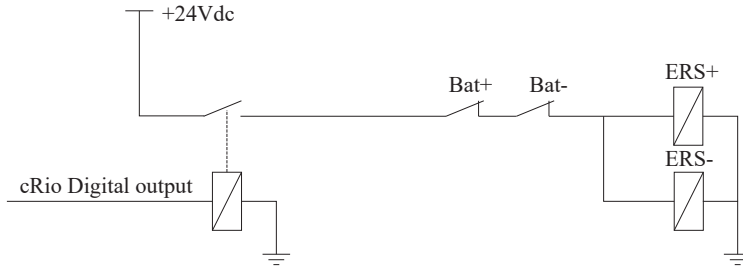


Figure 4.8: Basic schematic of the supply for the contactor coils. A help relay is used to feed 24V to the ERS contactor coils via help contacts of the pair of battery contactor coils.

necessary). The reason for feed forwarding/cross coupling of the torque is that in several of the experiments, power is circulated from one traction drive to another by allowing one drive maintaining a constant rotational speed and whilst the torque is varied on the other machine. Both machines are not allowed to operate in speed control simultaneously. The DC-link voltage control loop is necessary in order to enable the switching of supplies during operation as the two different supplies most likely do not have the same voltage. The DC-link voltage is controlled by a PI-controller which cannot be in operation unless the converter is disconnected from either supply, i.e., the DC-link of the converter is electrically floating.

4.3.2 Switch box and switching sequence

The electromechanical switches, contactors, of the switch box is controlled by digital output signals from the cRio with a relay driver to feed current to the coil of the contactor. Apart from the main contact of the device, it also features a normally closed help contact, which is used to ensure that two pairs of contactors cannot close simultaneously, i.e., the help contact of the devices connecting the battery supply is used to break the coil feeding circuit of the ERS supply and vice versa, see Fig. 4.8. The contactor of the cable shield is controlled by a separate control signal whereas the plus and minus pole contactors are controlled by a common control signal. The reason for this is to ensure that the cable shield connection (which is connected to the floating chassis) at all times is connected when the plus/minus poles are. This is achieved by a kind of blanking; when a converter is required to connect to one of the supplies, firstly the cable shield is connected and a certain time later, the poles connect. When disconnecting, the same procedure is followed the other way round. As the contactors are mechanical and the fact that there is a relay driver in between the digital output and the coil of the contactor, a propagation delay is expected.

The propagation delay of a turn-on scenario is shown in Fig. 4.9, where it is seen that there is a small delay between the digital output of the control system and the output of the relay driver, dotted and dashed lines of Fig. 4.9. The largest part of the total propagation delay is, however, seen between the dashed and the solid line of Fig. 4.9, which illustrates

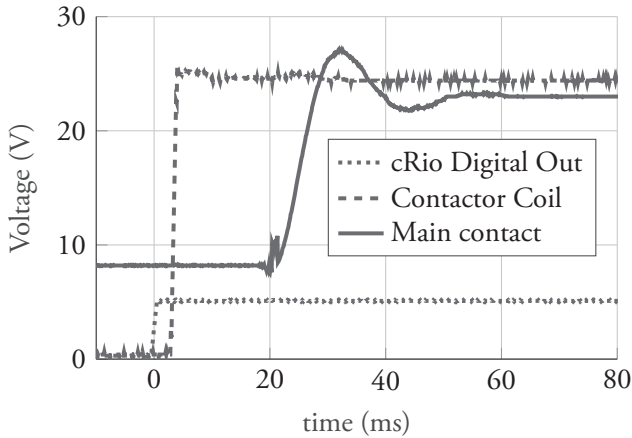
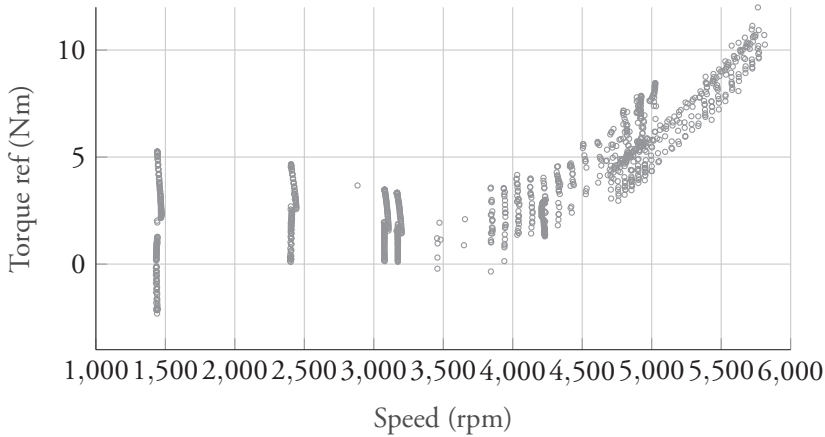


Figure 4.9: The activation of the electromechanical contactor and its propagation delay.

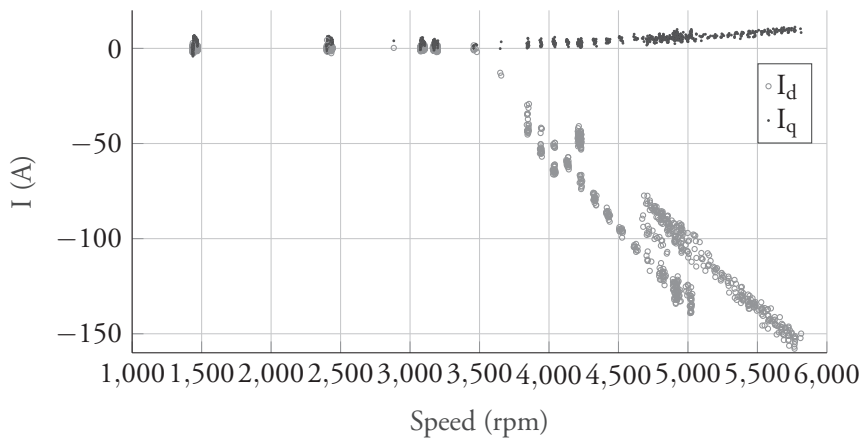
the time delay from where the current starts to flow through the contactor coil to when it actually overcomes the spring load and closes the circuit. The total propagation delay is taken into account when considering the turn-on of the contactors as part of a sequence. Turn-off of the contactor is not related to the same amount of propagation delay; the turn-off occurs within a couple of milliseconds from the instance the digital output goes low.

A software sequence is developed so that the whole sequence of disconnecting from one supply and connecting to another can be triggered by one signal alone. A detailed step by step explanation of the sequence follows below. The starting point is that both machines provide torque to accelerate the vehicle (=flywheel) when the sequence is initiated.

1. Reduce the torque to zero on the machine to be switched whilst the other machine is referenced with a higher torque to maintain total tractive torque. The torque is ramped up/down in order to smooth the process.
2. Wait until the DC current of the converter feeding the machine to be switched (as measured by a sensor inside the switch box) is close to zero.
3. Disconnect the converter to be switched from the supply.
4. Enter DC-link voltage control mode of the converter to be switched.
5. Wait until the voltage of the DC-link of the converter to be switched matches the voltage of the supply to be connected. The DC-link voltage of the converter is internally measured by the converter whereas the voltages of the supplies are measured by sensors inside the switch box.
6. Connect the converter to be switched to the new supply.



(a) Torque reference of the switching traction drive.



(b) Direct, d -, and quadrature, q -, currents of the traction drive.

Figure 4.10: Torque reference (a) and stator current (b) as function of rotational speed during the switching event where the machine operates in DC-link voltage control. The 'bars' of data points represent switching from low to high and from high to low.

7. Return both machines to their initial torque value.

The intention is to be able to perform the above sequence within the time a normal gear change would take, meaning well less than 1 s.

Fig. 4.10 shows the torque reference and stator current as a function of rotational speed of one machine during the switch sequence where it is operating in DC-link voltage control mode and alternating between the two supplies, set at 550 V and 650 V respectively. As the rotational speed of the machine is more or less constant during a switching event, each 'bar' of data points of Fig. 4.10a represents two switching events of the traction drive, from its original supply to the other, and then back to its original. At approximately 1000 rpm

it is clearly seen that there is one group of points above zero torque and one group below. The former represents when the DC-link voltage is decreased, i.e., energy is taken from the DC-link and provided to the output shaft of the machine, whilst the latter represents the event where the DC-link voltage is increased. As the rotational speed is increased while performing the switching sequence it is seen that, 1) the average torque reference, whether increasing or decreasing the DC-link voltage, is increasing and, 2) the difference in torque set point with respect to increasing or decreasing the DC-link voltage is decreasing (the 'height' of the bars is decreasing with increasing rotational speed).

The reason for the **average torque set point increase** with rotational speed is not completely understood. However, it could depend on the following. The effect becomes most prominent when the machine enters its field weakening operation range which means a direct (d -) axis current is fed to the machine in order to suppress the induced voltage, as shown in Fig. 4.10b. Should the rotor angle measurement not be perfectly calibrated, a d -axis current set by the controller will create a q -axis current as well, i.e., creating an active power flow in to or from the DC-link capacitor. This is made very obvious when the machine is rotating while the DC-link of its converter is not connected to a supply since it is easily observable when the DC-link voltage changes. However, the reason for the increased average output when entering field weakening cannot be fully explained by a static angular error between actual electrical angle and measured angle. Fig. 4.10a suggests that the average torque output, which would correspond to the torque reference required to keep the DC-link voltage constant when the DC-link is electrically floating, starts to significantly increase as the field weakening current is increased. This could suggest that the phenomenon seen here is due to the copper losses incurred in the stator windings by the field weakening current and that a certain amount of (mechanical) power is required to compensate. However, should this be the case, the average torque should be *negative* as motoring references are used here, i.e., positive torque generates energy flow from the DC-link to the electric machine. It should be noted, though, that the absolute value of the torque reference is small compared to the nominal torque of the machine which is approximately 450 Nm. Another possible reason for the behaviour shown can be not perfectly calibrated current measurement. To sum up, the reason for the behaviour shown in Fig. 4.10a is not fully understood. However, in order to handle this kind of imperfection, a feed forward term is added to the output of the DC-link voltage PI-regulator so that the integrator part of the controller does not have to compensate for a large error from the initiation of the switching sequence. The feed forward terms' dependence on the rotational speed can be practically solved in a number of ways. One option is to fit a mathematical expression to the 'average' value of the torque reference and add this as a feed forward term. Another option is to store the I-part of the controller at every switching event and use this value as a feed forward term when another switching event occurs at, or nearby, the same rotational speed.

The reason for the decreasing height of the torque data point 'bars' of Fig. 4.10a is explained by what is elaborated on regarding Eq. 4.2. The balance of electrical power at

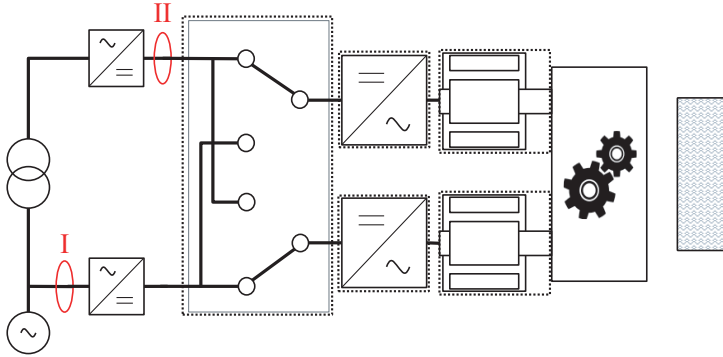


Figure 4.11: Measurement set-up of the AC charging efficiency. 'I' and 'II' shows where the input and output power are measured respectively.

the DC-link and mechanical power of the electrical machine is used in order to adapt the output of the DC-voltage controller, which is a DC-current, to a torque set point. As the rotational speed is increased the amount of torque required to alter the voltage of the DC-link capacitor is decreased if a certain DC-current is referenced by the controller, i.e., this behaviour is expected.

4.4 Preparations of Measurements

The following section outlines the method and set-up of equipment in order to perform a number of measurements.

4.4.1 Charging efficiency

Energy transfer from an ERS to the battery with the FIETS amounts to a number of conversions of power, justifying the effort to perform this study. The electrical power supplied to or provided by the electrical drives is measured by a Newtons 4th, PPA5500 power analyser [77], equipped with a LEM6 current transducer interface [78] and MACC Plus 2 current transducers [79]. A total of three channels (voltage and current) can be measured simultaneously.

In order to determine the maximum charging efficiency, the charging power is evaluated over a range of combinations of rotational speed and torque of the electric machines. This is achieved by operating one of the machines in constant speed mode and the other in torque control mode. At each speed, the torque of the other machine is increased from zero until the power limit is reached. The rotational speed is evaluated in steps of 500 rpm and the torque in steps of 20 Nm. At every speed step, the control system and the power analyser are logging the control signals and input/output power respectively.

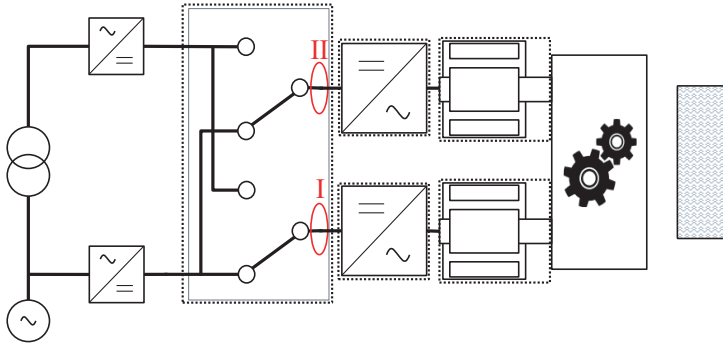


Figure 4.12: Measurement set-up of the DC charging efficiency. 'I' and 'II' shows where the input and output power are measured respectively.

The set-up of the AC charging efficiency measurement is schematically shown in Fig. 4.11 where the input power is measured at 'I'. The DC power at the battery is measured at the battery emulator 'II', the switch box is set in the configuration shown and the flywheel is disconnected from the mechanical transmission. The AC power is measured with two channels of the power analyser, using the two-wattmeter-method [80] whilst the DC power is measured with the third channel of the power analyser. The corresponding set-up of the DC charging efficiency measurement is shown in Fig. 4.12 where, again, the input power is measured at 'I' and output power at 'II'. The reason for the difference in positioning of the current sensors is due to a power limitation in the AFE (d) in Fig. 4.1 of approximately 60 kW. Higher power levels are only possible if the traction drives connect to the same AFE since the AFE then only has to supply the losses of the system. In both cases (AC charging and DC charging), the DC-link voltage of the AFE's is set to approximately 750 V. Ahead of the measurement the system is preconditioned by circulating a significant amount of power at a relatively high rotational speed in order to, mainly, pre-heat the mechanical transmission and its oil until steady state is reached at approximately 60 – 65 °C. The maximum rotational speed of the machines is limited to approximately 7000 rpm due to the resolver interface used.

4.4.2 Dynamic switching behaviour

The assessment of the switching behaviour is performed both below and above base speed of the electric machines and in both 'directions', i.e., the DC-link voltage of the traction converter is required to change from a high voltage supply to a lower voltage supply and vice versa. The control system itself is used for data acquisition.

The below base speed measurement is performed at approximately 1000 rpm during acceleration with the flywheel connected to the output shaft of the mechanical transmis-

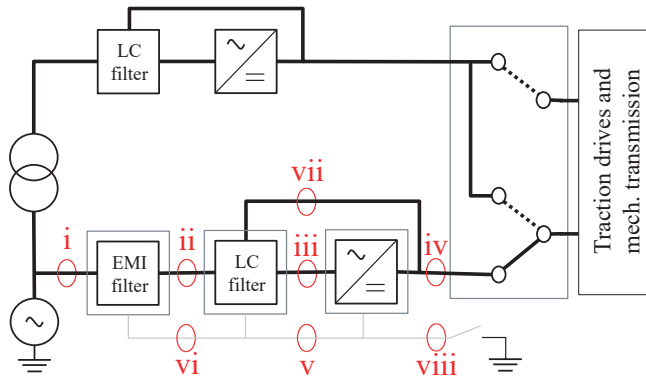


Figure 4.13: Measurement set-up of the common mode current where 'i' - 'viii' shows the measurements points. The switch box is arranged in *either* of the thick dashed lines. The gray lines illustrate the floating chassis which can be manually earthed. The traction drives and mechanical transmission are intentionally left out of the figure.

sion. Both traction drives are initially electrically connected to one of the supplies and are, sequentially, set to alter to the other supply. As the switching sequence is completed in a short amount of time, the rotational speed does not change significantly during the sequence, this is illustrated by the 'columns' of data points at certain rotational speed of Fig. 4.10a.

As the rotational speed is increased to above base speed, approximately 6000 rpm, the DC-link voltage is also lowered in order to operate the machine even further into the field weakening operation region. At such speed the flywheel cannot be connected to the mechanical transmission and as such, one of the machines are set to operate in constant speed mode whilst the other performs the switching sequence.

4.4.3 Common mode current

The common mode current is measured by using a GMC-I Prosys CP30 [81] current clamp where possible and where limitations due to cable size or similar arise either a Fluke i3000s rogowski current probe [82] or a Fluke 80i-1000s AC current probe [83] is used. The current probes are connected to a Picoscope 4824A [84] sampling at 20 MS/s. The measurement points are shown in Fig. 4.13 where the switch box is arranged according to *either* of the thick dashed lines. The upper dashed line is active when isolated charging is performed (the traction drives, and mechanical transmission are still part of the set-up but left out of the illustration for readability purpose) as the electrical power is circulated through the machines whilst the lower thick line is active when non-isolated charging is performed. The grey lines in the illustration shows the floating chassis that can be manually connected to earth by the switch at the bottom right. The reason for having said switch is to emulate a

scenario when statically charging as the vehicle normally is connected to protective earth and where a significant amount of parasitic, common mode, current will trip safety circuitry [85].

As non-isolated charging is emulated the lower dashed line is active and the battery emulator is set in constant DC-voltage mode (as is the default for this converter) whilst the AFE is set to power/current control. This way the power consumed by the grid is controlled by the AFE as the DC-voltage is kept constant by the battery emulator. The current controller of the AFE is configured so that active and reactive power consumed from the grid can be controlled independently. During the experiment when the common mode current is evaluated at different levels of grid power, only active power is consumed by the AFE.

On the contrary, when isolated charging is emulated, the AFE is set to operate in constant DC-voltage mode. The electric machine converters are set to constant speed control and torque control respectively. As a constant rotational speed is reached, the power consumed by the grid is, in effect, controlled by the electric machine operating in torque control mode.

In order to assess the common mode current at different levels of input power, the power analyser used for efficiency measurements is connected to the input of the AFE, measuring the input power.

4.5 Chapter summary

The experimental setup of an ETS concept, chosen among the three presented in Chapter 2, is presented. The ETS comprising integrated charging is chosen since it is deemed the least conventional approach to dynamic power transfer and most interesting to verify experimentally. A mechanical transmission fitted with two electrical machines to its input shafts and one flywheel connected to its output shaft constitute the mechanical part of the setup. A total of four power electronic converters constitutes the major part electrical setup where two are controlling the machines and two act as active rectifiers towards the grid, one emulating a DC-voltage source and one emulating a battery. National Instruments compactRio with LabView is chosen as the control and data acquisition equipment.

A number of experiment procedures are outlined in order to assess charging performance, dynamic controllability and parasitic current. The result of the experiments is presented in the following system validation and analysis chapters.

Chapter 5

System validation and analysis

A system level evaluation is performed in order to be able to assess the performance of the three different ETSs presented in Chapter 2. The performance in this context refers to the energy consumption of the vehicle and battery degradation. Beside the ETS analysis, the placement of the ERS is evaluated from the same performance aspect.

Firstly, this chapter presents the result of the measurements discussed in Chapter 4 and further elaborates on the post processing of these result. Further, data and characteristics regarding the vehicles and drive cycles evaluated in this study are presented, followed by the parameter set that is defined in order to study the difference in performance. Finally, the result of the system analysis is presented.

5.1 Measurement Results

The result of the measurements presented in Section 4.4.1 and 4.4.2 is presented below. As the result of both of these measurements have influence on the modelling the post processing of the data follows the result.

5.1.1 Efficiency

The measured charging efficiency as defined by

$$\eta = \frac{P_{out}}{P_{in}} \quad (5.1)$$

is shown in Fig. 5.1 where it is seen that the power limit encountered when measuring the AC charging efficiency is limiting the possibility to observe a local maxima of the efficiency. As for the DC-to-DC charging efficiency higher power levels are achieved and a maximum of approximately 87% efficiency is showed. It is expected to discover that the efficiency is lower when AC charging since one more conversion is included. Studying one common point, e.g., the combination of machine rotational speed at 3000 rpm and torque at 200

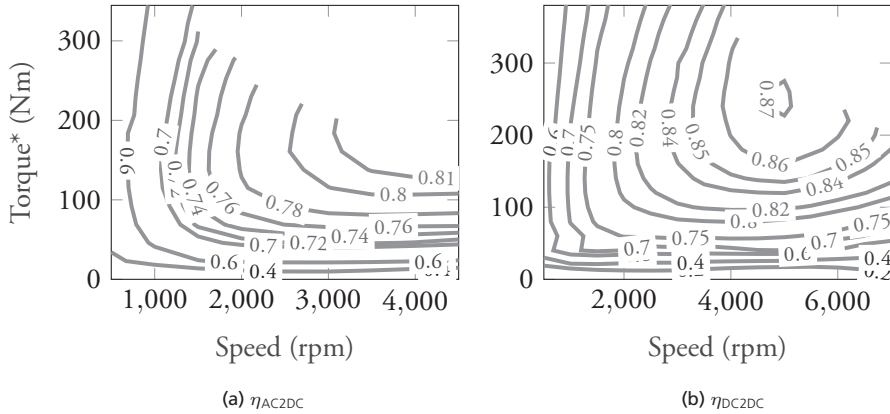


Figure 5.1: Charging efficiency as a function of rotational speed and torque reference of the supply-connected machine.

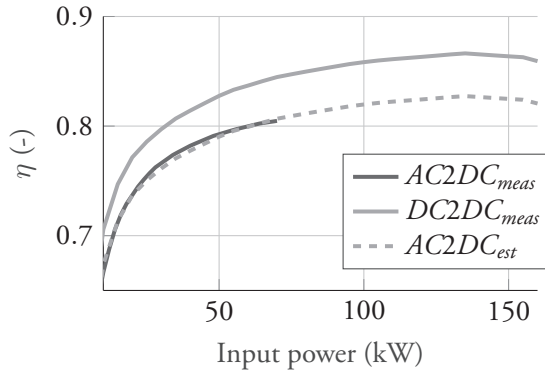


Figure 5.2: Maximum charging efficiency.

Nm for instance, the efficiency of the AC to DC case shows 80 – 81% and the DC-to-DC case approximately 84%, meaning a power loss of 3-4% in the AFE that is the grid interface. Fig. 5.2 shows the maximum efficiency achieved at every measured power level as a function of the input power. Assuming a similar behaviour of the efficiency with respect to input power, an estimate of the maximum AC to DC charging efficiency is shown. The dashed line estimate is the DC-to-DC efficiency curve multiplied with a factor 0.955 (representing an assumed AFE efficiency of 95.5%) in order to match the AC to DC efficiency, reaching a maximum of approximately 83 – 84%.

This result is important for two major reasons; 1) it directly shows what kind of efficiency one could expect statically charging with the FIETS, both from AC and DC (ERS or other), and 2) this result is used to extract a detailed efficiency map of the electric machines and their converters both in motoring and generating mode, see Section 5.1.3, which in turn is used in subsequent drive cycle simulations.

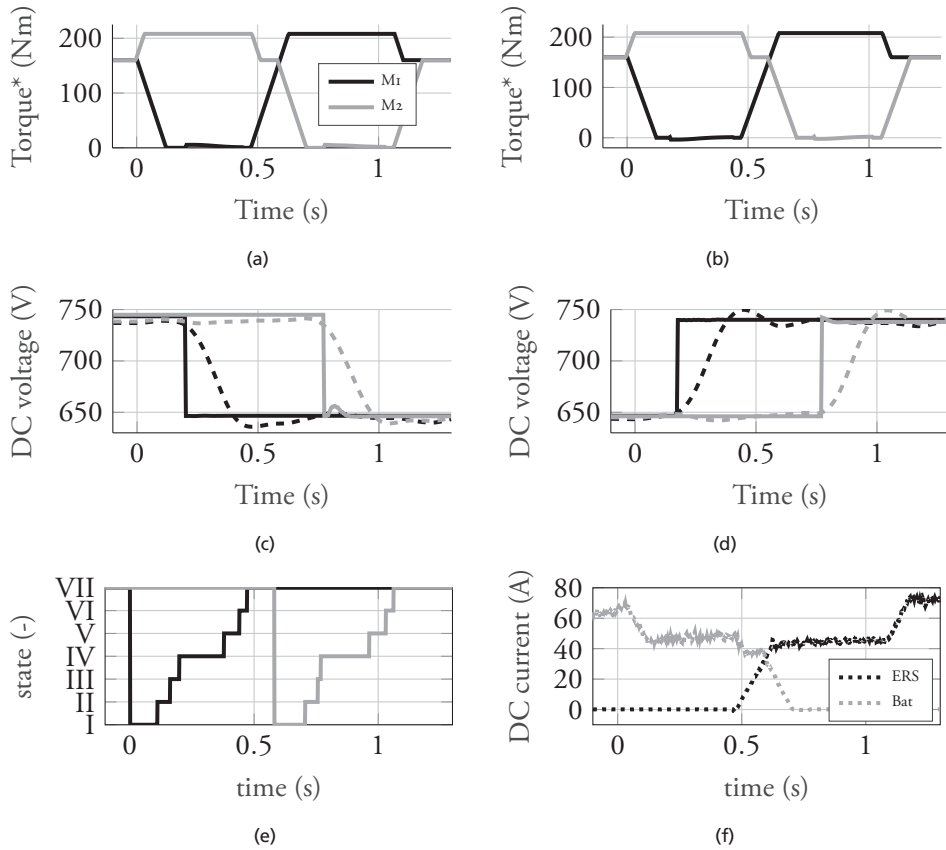


Figure 5.3: Switching sequence from high to low - and low to high - DC-link voltage during acceleration; (a) and (b) shows the torque reference, (c), (d) shows the corresponding measured DC-link voltage and reference for each of the traction drives whilst (e) illustrates the different states the control algorithm traverse during the sequence and (f) shows the DC current of each supply.

5.1.2 Dynamics of switching of electrical supply

With the flywheel attached to the mechanical transmission two switching sequences of DC supply between the battery and the ERS are performed as shown in Fig. 5.3. The sequence is performed during acceleration of the flywheel with both traction drives set at a reference torque of 160 Nm. At a certain speed, approximately 1000 rpm machine speed, the sequence is initiated and while one of the machines reduces its torque the other increases in order to maintain the acceleration. The increase of torque in the non-switching machine can be as large as is required within the maximum limit of the machine. In this experiment this increase is approximately 30% and mainly done in order to visualize how the sequence can be executed. When the torque of the switching machine is at zero the electrical connection on the DC side of the converter is opened and the voltage control mode is engaged, see the small positive torque reference starting at 0.2 s of Fig. 5.3a. Since the DC supply is

Table 5.1: Switching sequence states.

	Action	Condition to continue
I	Set current to zero	Current within zero margin
II	Dead time before release of DC-link contactor	-
III	Release DC-link contactor	Contactor released
IV	DC-link voltage control	DC-link voltage within set point limit
V	Close DC-link contactor	DC-link contactor closed
VI	Dead time before torque control engaged	-
VII	Torque control engaged	-

disconnected the voltage of the DC-link capacitors drops when applying a positive torque to the machine. When the DC voltage is within range of its set point the electrical connection on the DC side of the converter closes and torque ramps up and the sequence is repeated for the other machine. Similarly, Fig. 5.3b shows when the voltage is increased by applying a small negative torque to the machines when electrically disconnected, i.e., taking some of the rotational energy of the rotating mass to increase the energy (voltage) of the DC-link capacitors. Fig. 5.3e shows the states of the control algorithm that is executed at each instance in time, each state is explained in Table 5.1. It should be noted that there is no feedback of the status of whether the DC-link contactors are closed or open, but rather a certain amount of time is allowed to pass before the sequence is allowed to continue after an open/close command to the contactors. As shown in Fig. 4.9, approximately 20 ms is required from the activation of the digital output until the contactor circuit is closed.

In both cases, either increasing or decreasing the DC-link voltage, the total amount of time from initiating the sequence to the point where both machines are at the torque level at which they were before the sequence started, is approximately 1.2 s. It is clear that this time can be shortened by increasing the slope of which the torque reference is changed and also by decreasing the dead times before voltage control and further back to torque control mode is engaged. One method to shorten the sequence time duration is to design the circuit so that the propagation delay of the DC-link contactors is decreased, for instance by using solid state devices rather than electromechanical.

With the flywheel disconnected from the mechanical transmission higher speed of the machines can be achieved, Fig. 5.4 shows the DC voltage and reference of one machine switching supply at approximately 6000 rpm. Furthermore, the level of the DC voltage supplies is set to approximately 100 V lower than in the case with the flywheel attached in order to operate the machines deeper into field weakening. The result shows that the switching can be achieved in approximately 0.3 s. However, it is discovered that at higher speed, such as during this test, the DC voltage is more challenging to control.

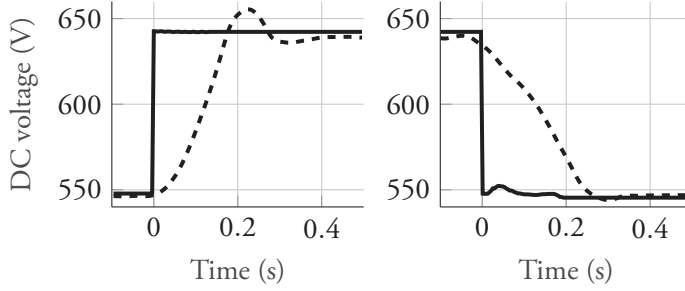


Figure 5.4: Switching sequence from low to high and high to low DC-link voltage while machine in field weakening operation.

5.1.3 Post processing

One of the purposes with the experiments performed is to extract an accurate model of the traction drives to be used in a system concept evaluation with regard to ETS topology and ERS placing strategy, see Chapter 5. In Fig. 5.1b is the energy transfer efficiency through two machines, one motoring and one generating, and the mechanical transmission presented. The total losses of the DC-to-DC conversion is expressed by

$$P_{loss,DC2DC} = P_{in} - P_{out} \quad (5.2)$$

as measured in Section 5.1.1. In order to extend the speed/torque map slightly, the input and output power are extrapolated using the Matlab 'gridfit' tool [86] to 10000 rpm and 400 Nm respectively. As the loss of the mechanical transmission as a function of input speed and torque is provided by the manufacturer, the total loss of both machines including converters can be determined by

$$P_{loss,tot,machine+conv} = P_{loss,DC2DC} - P_{loss,transmission} \quad (5.3)$$

The total losses of one machine including converter is divided into two parts

$$P_{loss,ind,machine+conv} = P_{loss,cu}(i) + P_{loss,f}(\omega) \quad (5.4)$$

where the first term denotes the copper losses, dependant on the current (assuming no skin effect in the phase windings) and the second term the frequency dependant losses, dependant on the rotational speed of the machines. The copper losses are calculated by

$$P_{loss,cu}(i) = 3 \cdot R_{phase} \cdot i_{phase,rms}^2 \quad (5.5)$$

where R_{phase} is measured to approximately 15 m Ω at room temperature, compensated for at the temperature at which the machines are operating according to $R(T) = R_{ref} \cdot (1 + \alpha_{cu} \cdot (T - T_{ref}))$ where α_{cu} is the temperature coefficient of copper. For each stationary measurement point of the input and output power, the current of each machine is also

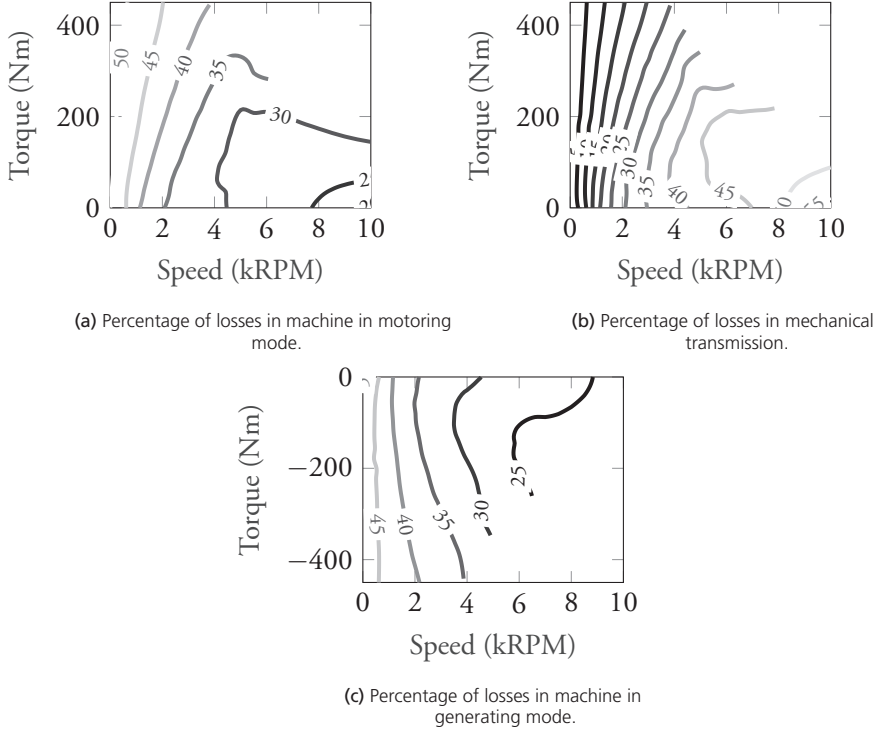


Figure 5.5: Loss distribution in percent of motor (a), mechanical transmission (b), and generator (c). The loss of the mechanical transmission is assumed to be symmetrical with regard to positive and negative torque.

stored, making it possible to calculate the resistive losses individually. The *total* frequency dependant losses can be calculated by

$$P_{loss,tot,f}(\omega) = P_{loss,tot,machine+conv} - P_{loss,tot,cu}(i) \quad (5.6)$$

where the last term is the sum of the resistive losses from both traction drives. As the machines does not rotate at the exact same speed (as per Section 4.2), the total frequency dependant losses are distributed between the traction drives at the same ratio as the difference in rotational speed:

$$\begin{aligned} P_{loss,mot,f}(\omega) &= 0.49 \cdot P_{loss,tot,f}(\omega) \\ P_{loss,gen,f}(\omega) &= 0.51 \cdot P_{loss,tot,f}(\omega) \end{aligned} \quad (5.7)$$

where the subscript *mot* and *gen* denote the motoring and generating traction drive respectively. The total amount of losses for each of the traction drives then become

$$\begin{aligned} P_{loss,mot} &= P_{loss,mot,cu} + P_{loss,mot,f} \\ P_{loss,gen} &= P_{loss,gen,cu} + P_{loss,gen,f} \end{aligned} \quad (5.8)$$

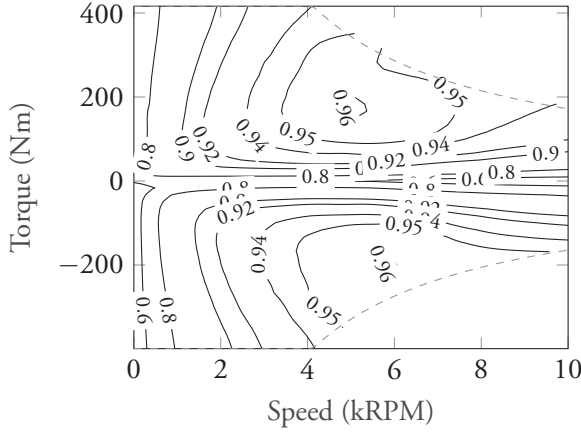


Figure 5.6: Efficiency of the experimentally verified traction drive.

As the total amount of losses for each of the traction drives are established, the loss distribution between the traction drives and mechanical transmission can be deduced. The resulting distribution is shown in Fig. 5.5. An efficiency map of the traction drive can now be created by calculating the efficiency of the traction drive in motoring and generating mode according to

$$\eta_{mot} = \frac{P_{mot} - P_{loss,mot}}{P_{mot}} \quad (5.9)$$

and

$$\eta_{gen} = \frac{P_{gen}}{P_{gen} + P_{loss,gen}} \quad (5.10)$$

where $P_{mot/gen}$ is the measured power at either the motoring and generating traction drive and $P_{loss,x}$ is the corresponding loss term of Eq. 5.8. The efficiency of the traction drive is presented in Section 3.1.2 and repeated here for convenience, see Fig. 5.6.

It is desirable to evaluate traction drives of different levels of rated power in the drive cycle simulations. In order to achieve this, the efficiency map as shown in Fig. 3.3 and 5.6 is used though the y-/torque- axis is altered in order to match the desired power requirement. The nominal torque of the machines experimentally evaluated is approximately 400 Nm and the efficiency map is in this study scaled from 350 Nm to 700 Nm.

The modelling of the switching sequence is made very simple since the level of complexity of the model is on a power and energy level and therefore the dynamics of the DC-link voltage control and the mechanical switches are omitted. Hence, the switching sequence is modelled as an interruption of traction torque for the duration of 0.6s whenever a switching event occurs. The time is chosen on the conservative side as it is shown that the sequence can be performed in an even shorter amount of time.

Table 5.2: Vehicle data.

	City Bus	Truck
Vehicle mass, M_v (tonne)	28	28/40
Frontal area, A_v (m ²)	7.3	9.4
Rolling resistance coefficient, C_r (-)	0.006	0.007
Air drag coefficient, C_d (-)	0.79	0.7
# gears (-)	2	3

5.2 Vehicles

Three different types of vehicles are included in this study; a city bus and two different types of long haul trucks. The focus in this thesis is on heavy transport vehicles since ERS technology is expected to be utilized with heavy duty road vehicles. The traction machines and the transmission are both designed for this type of vehicles. Another reason why the focus is on heavy transport in this study is that differences in outcome with regard to the performance measures stated above, is most likely emphasized when the power and energy demand is high, as is the case with heavy vehicles. Furthermore, with regard to the placing of the ERS and the following consequence whether a vehicle is able to complete the drive cycle, it makes more sense to let the high power/energy consuming vehicles dictate the conditions rather than the passenger vehicles if the ERS is supposed to care for the power and energy supply of all road traffic.

The data of the vehicles are shown in Table 5.2. The characteristics of the vehicles are based on typical values found on the current market. The city bus is on the larger/heavier side of what is typical values for the mass of such a vehicle. Although, a higher mass is deemed more important to evaluate as the requirement on the on-board energy storage capacity and/or energy consumption increases as the mass increase. The long-haul truck is evaluated at two different mass levels; the higher is the typical maximum allowed weight of a long-haul truck in Europe [87]. The lower weight is based on [88] where it is shown that in Sweden, for the last ten years (as data is available), the largest amount of travelled distance is made by long haul trucks in the range of 26 – 28 tonnes.

5.3 Drive cycles

The drive cycle model consists of time series containing the vehicle speed reference value as well as the slope of the road. The former value is fed to the driver model of the vehicle model whereas the latter is fed to the road model. Characteristics describing each drive cycle is presented in Table 5.3.

For each vehicle type, a suitable drive cycle is chosen. The city bus drive cycle is sampled from a real bus route (City bus route number 85 of Gothenburg, no longer in operation)

containing a great deal of stop-start traffic as well as containing several up and down hills. The sampled drive cycle travels from A to B, which is why an even number of multiples of the drive cycle is repeated in order to make the vehicle finish where it starts. A total of three total runs (three from A to B, three from B to A) are compiled into one single drive cycle in order to emulate one work shifts worth of duty.

The drive cycle used with the truck, is a long-haul, high-speed, long-distance drive cycle which travels from A to B and back to A. The majority of time is spent at approximately maximum speed whilst the altitude variation is high; equating to a demanding drive cycle for the long haul truck. The distance and time are approximately what can be expected from two days of work with one driver.

The drive cycles chosen are not what typically is seen in this context, i.e., they are not standardized drive cycles. They are, however, albeit on the more demanding side, a reasonable representation of a drive cycle these types of vehicles operate on. A number of drive cycles have been characterized and compared in [89] where the parameter *aggressiveness*, A is defined as

$$A = \sum_{i=1}^n \int_{t_{i,1}}^{t_{i,2}} (a \cdot v) dt / s \quad (5.11)$$

where a (m/s^2) is the positive (forward) acceleration and v (m/s) the speed of the bus, n (-) is the number of positive acceleration periods, $t_{i,1}$ (s) and $t_{i,2}$ (s) are the start and end of the i -th positive acceleration period, and s is the distance of the entire driving cycle. As expected, the aggressiveness is substantially higher in the city bus drive cycle compared to the long-haul truck drive cycle.

The energy use is presented to give an indication rather than the exact number as it depends on type of ETS, battery capacity, rating of traction drives and so on. The energy use associated with the long-haul truck represents the lower mass of the vehicle investigated.

5.4 Parameter sweep

In order to evaluate the performance of the different ETS topologies a number of parameters, related to the characteristics of the drive train on-board the vehicle as well as ERS characteristics, are selected for adjustment. The parameter set is showed in Table 5.4 where the three ETSs are represented by one column each. The parameters of the truck are divided into its 28- and 40-ton versions where a difference in data is present. A parameter defined as, for instance, 140:20:220 indicates that the parameter range is from (and including) 140 to (and including) 220 with a step size of 20.

The bus is evaluated for two different levels of auxiliary load as the HVAC can be a significant consumer of energy. The two different power levels are set to emulate a scenario of low and high HVAC power requirement respectively.

Table 5.3: Characteristics of the drive cycles.

	City bus route	Long haul
v_{mean} (km/h)	21	84
v_{max} (km/h)	70	89
$v_{mean,drive}$ (km/h)	24	84
Distance (km)	153	1090
Maximum altitude variation (m)	70	473
Time (hour:min)	7 : 10	13 : 03
acc_{max} (m/s ²)	2.0	1.6
dec_{max} (m/s ²)	2.9	3.2
acc_{mean} (m/s ²)	0.47	0.02
dec_{mean} (m/s ²)	0.36	0.02
A (m/s ²)	0.21	0.008
Typical energy use (kWh)	180	1500

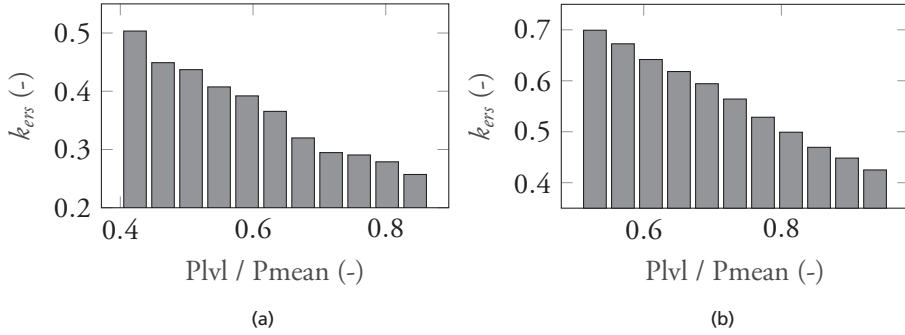


Figure 5.7: Level of relative ERS coverage, k_{ers} , as a function of different levels of traction power requirement normalized with respect to the average traction power requirement. The leftmost figure (a) shows the ERS coverage for the city bus in the city bus route whereas the rightmost (b), shows the ERS coverage for the truck in the long haul drive cycle.

The k_{ers} and d_{ers} quantities relates to what is explained in Chapter 2. The k_{ers} ADA shows only the minimum and maximum value since the difference between two consecutive levels of k_{ers} is not constant as in the case with k_{ers} EQU as it is the tractive power requirement that determines the exact value of the relative ERS coverage. A total of 11 levels of k_{ers} ADA is considered as illustrated by Fig. 5.7. The x-axis if Fig. 5.7 relates to the relative traction power level with regard to the average traction power level above which, the ERS sections are placed.

Beside the parameter sweep, the city bus is evaluated with two different control methods as explained in Section 3.1.6 where the effect of maximum possible regeneration of braking

Table 5.4: Rating of powertrain components and ERS.

Bus			
	FIETS	HSETS	LSETS
$P_{em}/\text{machine}$ (kW)	140 : 20 : 220		
P_{DC-DC} (kW)	-	140 : 20 : 220	40 : 20 : 100
W_{batt} (kWh)	70, 100, 200, 300		
P_{aux} (kW)	2 / 15		
k_{ers} EQU (-)	0 : 0.1 : 1		
d_{ers} EQU (km)	1, 3, 6, 10		
k_{ers} ADA, min/max (-)	0.26/0.50		
$s_{ers,min}$ ADA (km)	0.3		
Truck 28 / 40 ton			
	FIETS	HSETS	LSETS
$P_{em}/\text{machine}$ (kW)	140 : 20 : 220 / 200 : 20 : 280		
P_{DC-DC} (kW)	-	120 : 20 : 200 / 180 : 20 : 260	40 : 20 : 100 / 60 : 20 : 120
W_{batt} (kWh)	200 : 100 : 500		
P_{aux} (kW)	4		
k_{ers} EQU (-)	0.4 : 0.1 : 1		
d_{ers} EQU (km)	1, 3, 10, 30, 100		
k_{ers} ADA, min/max (-)	0.425/0.7		
$s_{ers,min}$ ADA (km)	1		

power is evaluated.

5.5 Result and discussion

This section presents the result of the simulation campaign with its parameter sweep presented above. In order to compare the performance of different ETS topologies and/or ERS placing methods, the result is usually presented in a figure with a surface as a function of two independent variables from Table 5.4.

A certain outcome of the simulation, be it the energy consumption or distance travelled

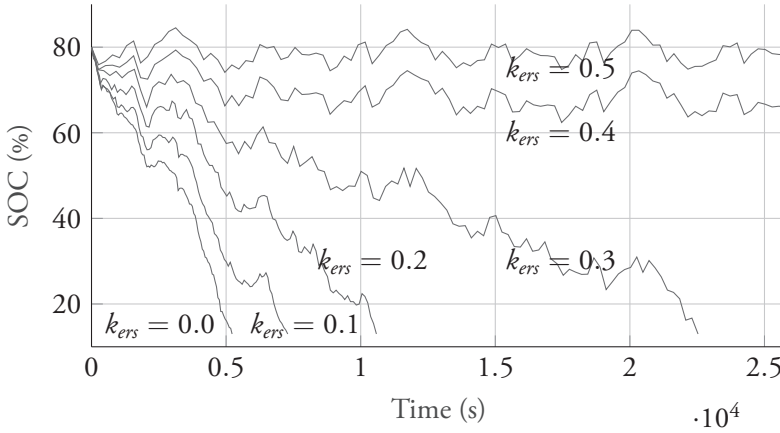


Figure 5.8: SOC of the city bus with the FIETS, $P_{em} = 180$ kW, $W_{batt} = 70$ kWh, on the city bus route, $d_{ers} = 3$ km, at different levels of relative ERS coverage.

for instance, can be displayed as a function of any of the parameters in the parameter set. As it is challenging to illustrate data as a function of more than two variables, it is of importance to choose the independent variables with care in order to illustrate what indeed affects the outcome and also in order to reduce the quantity of data to display as the simulation sweep of each vehicle can be presented by hundreds of figures. Therefore, when the result show that a certain outcome is not to a great extent affected by one or several parameters, these parameters are fixed at a certain value. Another reason why one parameter might be fixed is that its effect on the outcome is expected and straight forward to elaborate on without a bespoke illustration.

Energy consumption of the vehicle is of great interest to study as one outcome of the simulation campaign and it is defined as the sum of the energy supplied by the ERS during the drive cycle and the start to finish energy difference in the battery. At the end of the drive cycle, if the SOC of the battery is lower than its initial value, the losses related to bringing the battery back to its initial value is also added to the total energy consumption.

Similarly, to the addition of charging losses to the energy consumption to compensate for the SOC swing from start to finish of the drive cycle, the cycle ageing of the battery is taking into account the energy cycle required to bring the battery to its initial SOC.

The chapter is mainly divided into two parts, firstly, the result regarding the city bus is presented, followed by the two versions of the long-haul truck.

5.5.1 City bus

In order to benchmark the different ETs with regard to energy consumption and battery degradation, an approximate equal level of charging performance has to be concluded. Charging performance in this context refers to the vehicles' ability to complete a full drive cycle without running out of energy. An illustration of how the SOC changes over the drive

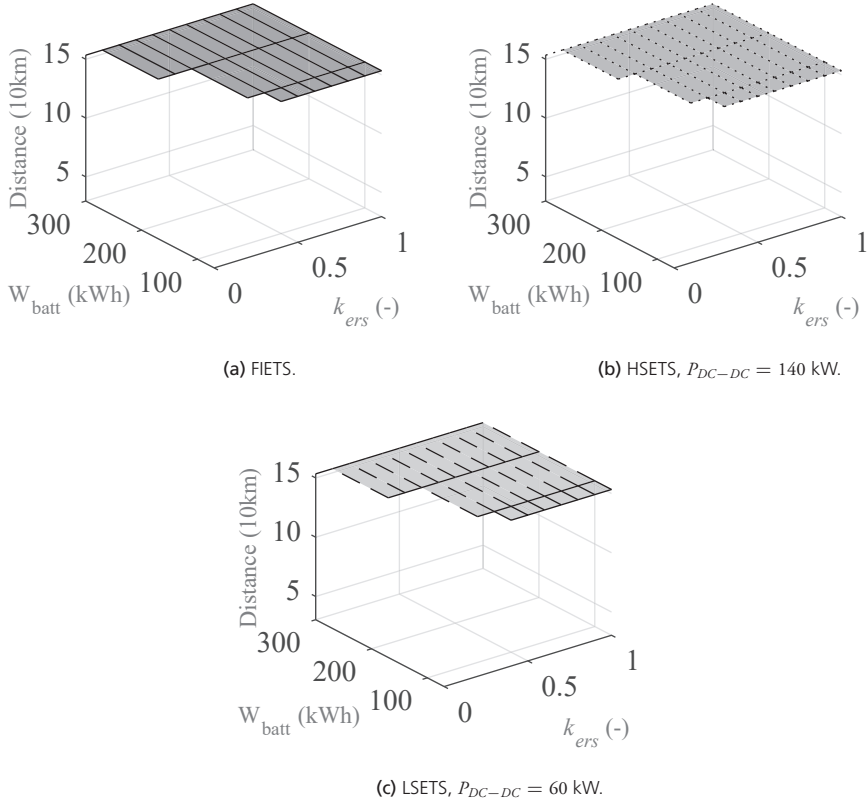


Figure 5.9: The city bus equipped with different ETSs ability to complete the drive cycle as a function of ERS coverage, k_{ers} , and battery capacity, W_{batt} . $P_{em} = 180$ kW in all three ETSs. The ERS is placed according to the EQU method.

cycle at different levels of relative ERS coverage is shown in Fig. 5.8. When the SOC reaches 15% the simulation is stopped and considered not successful. The ability to complete the drive cycle mainly depends on the capability of receiving energy from the ERS (limited by the rated power of the DC-DC converter for instance), the amount of relative ERS coverage (k_{ers}) and the battery capacity. Fig. 5.9 shows the distance travelled as a function of the relative ERS coverage and battery capacity. The figure only shows the data points where the drive cycle is completed. It can be seen that the city bus equipped with different ETS is able to complete the drive cycle to the same extent when the high-power DC-DC converter in the HSETS is rated at 140 kW and the DC-DC converter in the LSETS at 60 kW. (The rated power of the HSETS could probably be derated slightly and still perform on the same level as the others, however, the HSETS is not evaluated with a lower P_{DC-DC} than 140 kW.) The FIETS is in this case equipped with traction drives rated at 180 kW each and it is found that the rated power of the traction drives does not affect the ability to complete the drive cycle to a great extent, within the range evaluated. This means that the

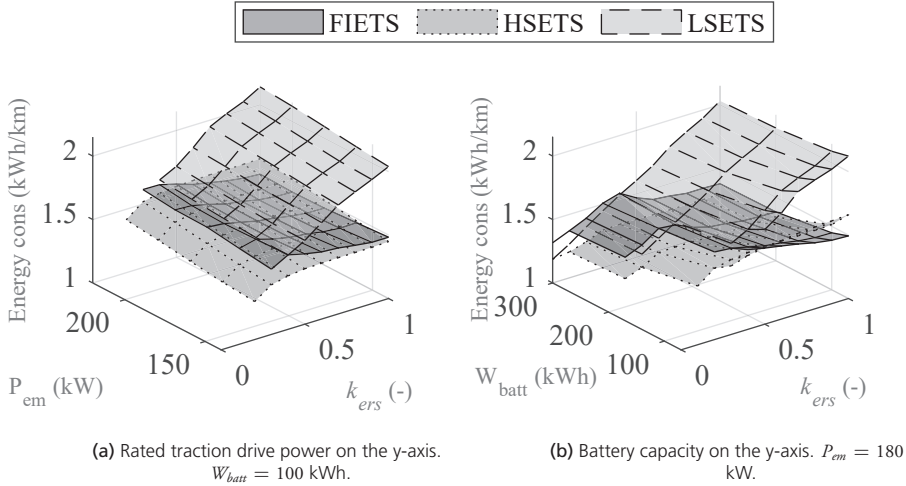


Figure 5.10: Energy consumption comparison of the city bus across the three ETs with EQU ERS placing.

average power the drive cycle requires is lower than what a traction drive rated at 140 kW (the lowest level of rated power evaluated) can deliver in terms of charging performance, in combination with the lowest level of k_{ers} required in order to complete the drive cycle, as shown by Fig. 5.9. As the FIETS is chosen to be equipped with traction drives of 180 kW rated power, the rated power of the tractions drives of the other two ETs are also fixed at 180 kW. Unless otherwise stated, the rated power of the traction drives is fixed at said level in the whole result section.

The level of d_{ers} is set at 3 km in all presented data unless otherwise stated as it is found that the level of d_{ers} does not affect the vehicles' ability to complete the drive cycle to a significant extent. This is not unexpected since the d_{ers} parameter only relates to the distance between sections. Although, if the d_{ers} becomes long in relation to the on-board energy capacity, then it will affect the ability to complete the drive cycle due to the shear distance between sections. In this case, though, the longest d_{ers} distance is 10 km, which is short in relation to the on-board energy storage capacity. The control method is the MnSW unless otherwise stated, which does *not* regenerate as much braking energy as possible but rather minimizes the number of switching events of the switch box (FIETS and LSETS). The auxiliary load is set to 2 kW unless otherwise stated.

The convention of Fig. 5.9 where the data of the FIETS is illustrated by a solid line surface, the HSETS data by a dotted line surface and the LSETS data by a dashed line surface is kept throughout the result section.

5.5.1.1 Energy consumption

As the energy consumption is one of the main cost carrying posts of operating a vehicle of this kind, it is of interest to evaluate to what extent the energy consumption is affected by

different rating of components, control strategy and ERS placing, naming a few. Fig. 5.10 shows the energy consumption in two different configurations; both have the relative ERS coverage on the x-axis whereas Fig. 5.10a has rated traction drive power on the y-axis and Fig. 5.10b have the battery capacity on the y-axis. Fig. 5.10a shows that the rated power of the traction drives is not a significant influence on the energy consumption. Both the HSETS and LSETS show a slight increase in energy consumption with increasing traction power. This is due to that, in average over the drive cycle, the operating points are moved to a slightly lower efficiency position as the rated power increase. As the operating points are determined by the speed of the vehicle and traction torque requirement, the absolute operating points stay relatively the same regardless of rated traction power. In turn, this means that the operating points are moved to a lower relative torque as the rated power increase. Referring to Fig. 3.3 shows that the efficiency decrease as this occurs. The FIETS shows a slightly different behaviour as the energy consumption is relatively constant as the rated traction power changes. The main difference between the FIETS and the HSETS and LSETS is that in the former, the traction drives are integral parts of the energy transfer from ERS to battery, meaning the operating points of the traction drives differs significantly from when they only care for the traction power. As the FIETS, in average over the drive cycle, operates its traction drives at a higher power level, it is shown that it can even be beneficial to increase the rated traction power as the energy consumption decreases slightly with increasing rated traction power. Depending on vehicle and driving situation, a higher available traction power might also be desirable for other reasons.

In conclusion with regard to the rated traction powers' influence on the energy consumption, it is concluded that the effect is small and relatively expected which is why this parameter is fixed at 180 kW in the following results presented.

Still focusing on Fig. 5.10a, it is clear that the relative ERS coverage is of greater influence on the energy consumption and also that the different ETSs show a different behaviour with altering ERS coverage. The LSETS differs in its behaviour in comparison to the FIETS and HSETS as a significant increase in energy consumption of approximately 30% is shown from the lowest to the highest level of k_{ers} . The reason for this is due to the control method of the ETS where the traction drives unconditionally connect to the ERS when present above a certain speed, regardless of traction torque requirement. In turn, this means that regeneration of energy is lost whenever an ERS is present for the vehicle as the ERS is not considered being able to receive energy. Braking with the traction drives are thus not possible when the traction drive is directly connected to the ERS, but instead the kinetic energy of the vehicle is turned into heat with the friction brakes. On the contrary, the FIETS shows a decrease of energy consumption as the relative ERS coverage increase. The FIETS has, due to the switch box, the capability to run its traction drives directly from the ERS supply if the SOC of the battery is high enough. Doing this, the number of energy conversions are reduced significantly as the energy does not have to firstly reach the battery via the traction drives. The HSETS shows a slight increase of energy consumption as the relative ERS coverage increase. This is partly due to the fact that the energy from the ERS

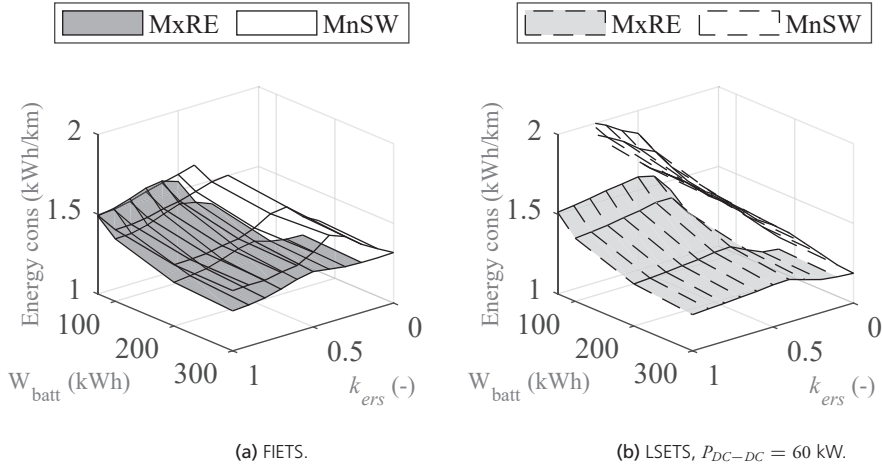


Figure 5.11: Comparison of energy consumption with two different control methods, MnSW and MxRE, of the city bus with EQU ERS placing. Note the different viewing angle from previous figures.

must pass through the DC-DC converter which will generate more loss the more energy it supplies. Also, with a high enough level of k_{ers} the battery is cycled around a relatively high average SOC, i.e. the SOC does not drop significantly from the set-point between ERS sections, which will generate more losses in the battery than if the SOC was fluctuating around 50% for instance, see Fig. 3.5. This is obviously true for all the ETSs as the k_{ers} is high, however with the FIETS and LSETS, other effects are more prominent, hiding the battery loss effect. This could possibly be mitigated with a control strategy based on knowledge about the actual ERS coverage along the drive cycle at any given point as the battery might not having to be charged to a high level of SOC. This kind of control strategy is, however, not investigated.

The energy consumption is presented in Fig. 5.10b with battery capacity on the y-axis rather than rated traction power. This way is deemed more interesting than the former way of displaying data as, 1) the battery carries a higher relative part of the total cost of EVs [90], [91] and, 2) the energy consumption is affected more by altering battery capacity than rating of the traction drives, although not obvious in Fig. 5.10b. The dependence on k_{ers} is naturally similar in comparison with Fig. 5.10a whilst it shows that as the battery capacity increase the energy consumption decrease. This is due to the fact that a higher capacity battery generally produce a smaller amount of loss compared to a smaller capacity battery, see Fig. 3.5.

One way of mitigating the substantial increase in energy consumption with increasing relative ERS coverage of the LSETS is to allow the switch box to rearrange its switches so that when a negative traction torque is required, the traction drives connect to the battery in order to recuperate braking energy. When positive traction torque once again is required, the switch box rearranges to its initial state. As it is shown that a switching event can be done within a couple of hundreds of milliseconds it is considered possible, from a control

perspective, to operate the vehicle in such a way. In Fig. 5.11 a comparison is shown of the **MnSW (minimum number of switching events)** and **MxRE (maximum regeneration) control methods**. The non-filled surfaces are identical to what is shown previously in Fig. 5.10b and the filled surfaces show the energy consumption with the MxRE control method. Only the FIETS and LSETS are shown as the HSETS is not applicable to this kind of control method as its traction drives at all times are connected to the battery enabling recuperation regardless of the presence of ERS. It is shown that the decrease in energy consumption is substantial in the LSETS case with the MxRE control method, as would be expected. A smaller benefit is noted in the FIETS case which also is expected as in most cases at least one traction drive is connected to the ERS, making regeneration of braking power up to half of the total installed traction power possible.

A consequence following the MxRE control strategy is that the number of switching events increase which in turn will lead to increased wear on the switches, especially if they are of mechanical type as in the prototype presented in Chapter 4. The number of switching events depends, regardless of control method, mainly on the relative ERS coverage. The difference in number of switching event for the LSETS ranges from approximately a factor of two at low k_{ers} up to approximately a factor of three for high k_{ers} likely degrading the lifetime of the switches an equal amount. In other words, the time between switching events range from, on average, every 40 to 120 seconds with the MnSW control method and every 14 to 60 seconds with the MxRE control method. The difference in number of switching events is greater with the FIETS as it allows for connecting and disconnecting from the ERS regardless of vehicle speed. With the MnSW control method a switching event occur in the range of every 80 to 800 seconds whilst with the MxRE control method the time between switching event decrease to the range of approximately every 10 to 40 seconds. Whether or not the number of switching events impose a potential problem regarding the lifetime of the switch box depends on the type of switch and also whether or not soft switching of said devices can be guaranteed. The switching sequence proposed and validated in this thesis does ensure that opening and closing of the switches within the switch box occur at zero current. To summarize, it can be concluded that there is a potential trade-off between energy consumption and lifetime of the switching devices.

Moving on, the **auxiliary load** might differ greatly on a city bus depending on, primarily, outer temperature. In cold weather, the HVAC is required to heat the passenger compartment and vice versa. In mild weather the HVAC might not be required to neither heat nor cool the passenger compartment, whereas on cold or hot and sunny days, the HVAC becomes a significant consumer of energy. When either heating or cooling is required, the average power consumed by the HVAC might be on-par with the average traction power [92], i.e., a significant add on to the energy consumption. Fig. 5.12 shows a comparison of two different levels of auxiliary loads in the three different ETSS. The difference in energy consumption due to the increased auxiliary load can be seen as an offset in the figure, i.e., the surfaces are closely matched except the fact that they are vertically shifted. The amount the surface is shifted differs depending on ETS; the FIETS, HSETS and LSETS see an

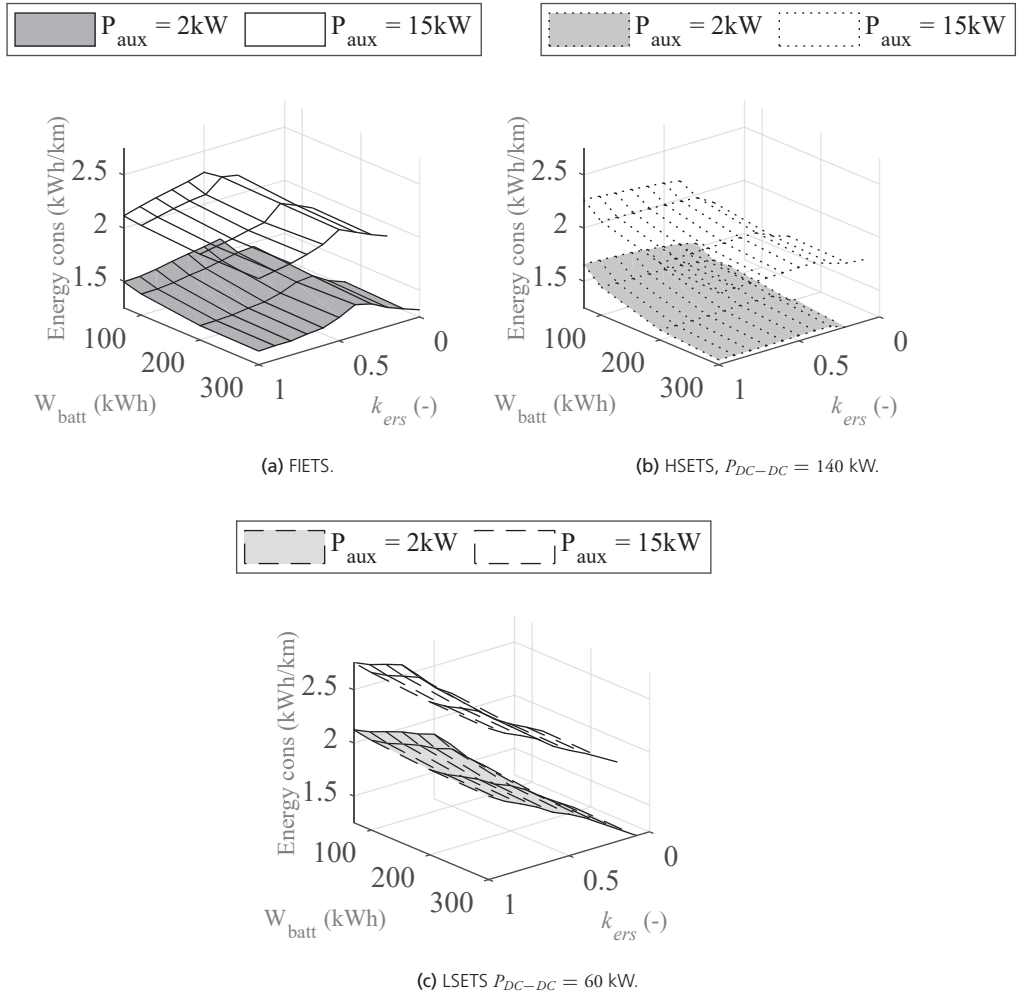


Figure 5.12: Energy consumption of the city bus at different levels of auxiliary load.

average increase in energy consumption of approximately 55%, 45% and 35% respectively. The fact that the FIETS shows the biggest difference in energy consumption due to the increased auxiliary load is not unexpected due to the number of conversions the electrical energy has to pass through from the supply (the ERS) to the load which is electrically parallel to the battery, see Fig. 2.8. The difference in energy consumption increases with regard to the HSETS and LSETS are similar in absolute numbers, approximately 6 kWh/10km is added to the initial consumption but due to the lower initial consumption of the HSETS, the relative difference becomes larger than with the LSETS. What is not clearly observed in the figure is that the LSETS is affected the most with regard to its ability to complete the drive cycle due to the increase in auxiliary load. Approximately a 20% increase of rel-

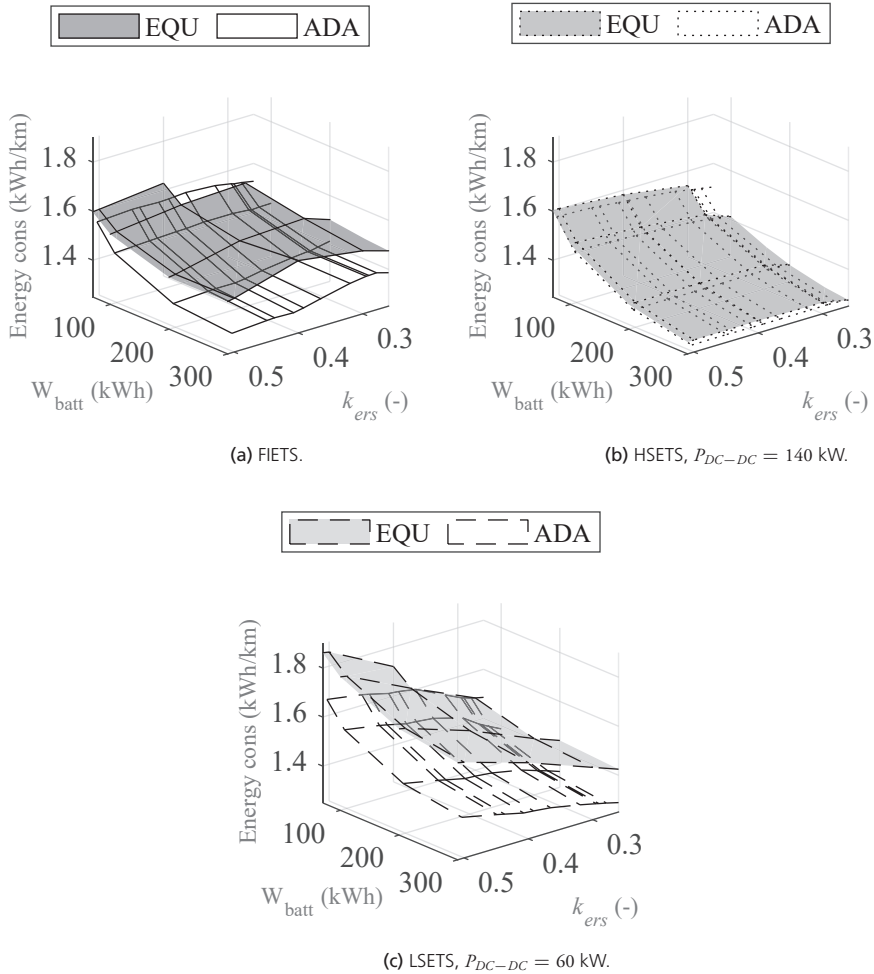


Figure 5.13: Energy consumption of the city bus with different ERS placing methods along the drive cycle.

active ERS coverage is needed as the auxiliary load is increased in order to make the LSETS equipped vehicle complete the drive cycle. The FIETS and HSETS shows the same tendency but at a lower level, generally a 10% increase of relative ERS coverage is required. The reason why the LSETS is mostly affected by the increase in auxiliary load is that its DC-DC converter is rated at a comparatively low power and as it must supply all the power to both the battery and auxiliary load, it is going to be a limiting factor, more so than in the FIETS and HSETS.

Besides what can be done on-board the vehicle, be it rating of components or the topology of the ETS, what is also interesting to investigate is how **the placing of the ERS sections** might affect certain outcomes of the drive cycle simulations. As elaborated on in Section 2.4, two different methods of placing the ERS is evaluated. Up until this point in this

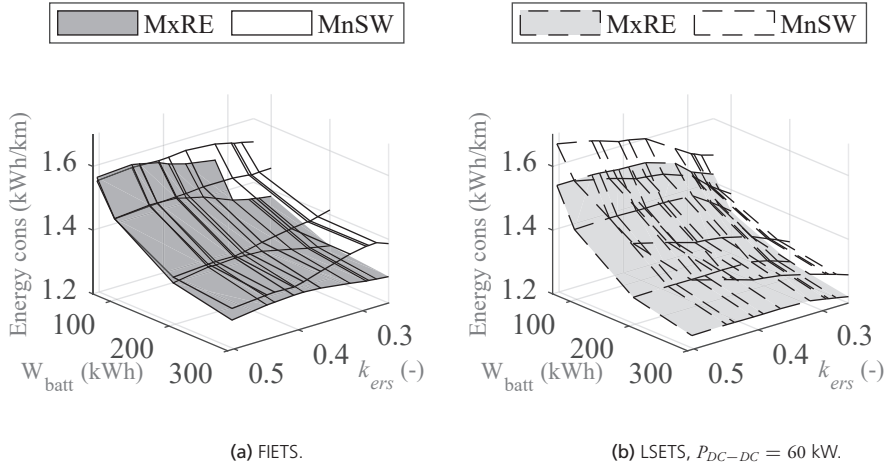


Figure 5.14: Comparison of energy consumption with two different control methods, MnSW and MxRE, of the city bus with ADA ERS placing.

Chapter, the ERS is placed according to the EQU placing method, meaning equidistantly placed along the drive cycle. The other way investigated is the ADA method, where the ERS sections are placed where the traction power requirement is high, typically along up hills and typical places of acceleration. Fig. 5.13 shows a comparison of energy consumption with regard to the ERS placing method. The non-filled surface shows the EQU energy consumption and the filled shows the ADA energy consumption. The axes are scaled only to cover ERS levels that overlap the two methods. It is clearly seen that the difference in energy consumption is the smallest in the HSETS case where only a difference of approximately 1% is shown. The FIETS and LSETS are, however, affected to a greater extent, as a decrease of energy consumption up to 10 – 15% is shown. The reason this result is seen is due to the fact that in the HSETS, traction and energy transfer from the ERS is de-coupled, i.e., the DC-DC converter is completely independent from the operation of the traction drives. Thus, whether the ERS is placed along an uphill or downhill makes little to no impact on the energy consumption. The FIETS and LSETS benefit to a greater extent due to the fact that as high power is required, the machines can operate directly from the ERS rather than from the battery, again reducing the conversion losses and the total consumption. What is not clearly seen in the figure is the fact that the FIETS and LSETS vehicles paired with a smaller capacity battery, 70 – 100 kWh, manages to complete the drive cycle with a k_{ers} reduction of approximately 25% in the ADA compared to the EQU placing of ERS sections. Hence, a sophisticated approach to the ERS placing might possibly reduce the need of ERS coverage significantly.

Finally, it should also be noted that further decrease in energy consumption can be achieved if the MxRE control method is deployed in conjunction with the ADA ERS placing, as shown in Fig. 5.14. The difference is smaller than when the ERS is placed by the EQU method, which is to be expected since the main drawback with the EQU method is

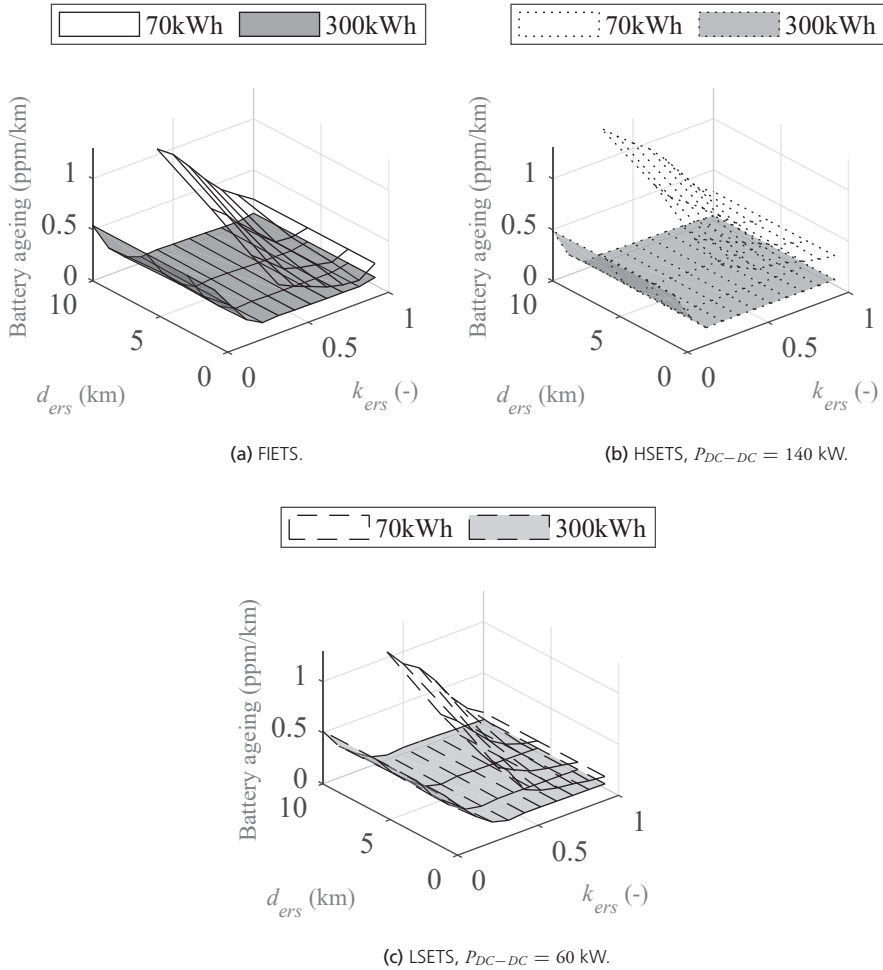


Figure 5.15: Fraction of battery life spent per drive cycle (%/ km) with the city bus.

that regeneration of braking power is lost whenever ERS is present. With the ADA ERS, however, the ERS sections are typically not present at locations where a negative traction torque is required, hence a greater amount of braking energy can be recuperated without having to rearrange the switch box solely for this purpose.

5.5.1.2 Battery ageing

The battery degradation is evaluated after each completed drive cycle for each of the ETS under all different configurations and control methods. The model of the battery ageing mechanism is explained in Section 3.1.3. Only the number of cycles and the DoD of said cycles are taken into account when regarding the ageing of the battery.

Fig. 5.15 shows the amount of **battery degradation as function of d_{ers} and k_{ers}** for the

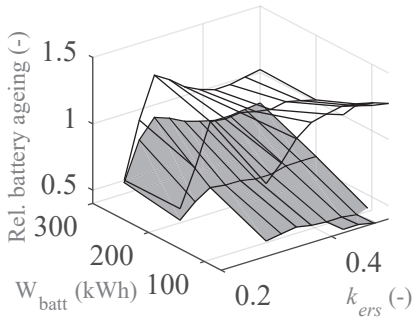
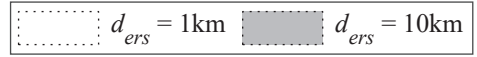
three ETSs with EQU ERS placing, MnSW control method and 2 kW of auxiliary load is used. It can be seen that the difference in battery degradation between the ETSs is limited, suggesting the method of feeding energy from the supply to the wheels and battery are of modest importance. Instead, the characteristics of the ERS and the battery capacity affecting the degradation to a larger extent. Two different levels of battery capacity are illustrated by the two surfaces in each sub figure. It is shown that the battery degradation decreases as the battery capacity increase since a given cycle of *energy* is a smaller cycle in SOC as the capacity increases, see Fig. 3.7 how the total number of cycles of a certain DoD is affecting the ageing. In Fig. 5.15 it is also shown that battery ageing is, for a smaller capacity battery, to a great extent affected by d_{ers} which is not unexpected as a longer distance between ERS sections naturally will cycle the battery deeper. The reason this behaviour cannot be observed to the same extent with the larger capacity battery is that with this amount of energy on-board, the effect of the distance between ERS sections is limited. It can also be seen that the degradation increases with decreasing k_{ers} . As the relative ERS coverage is small, the vehicle is on the verge of completing the drive cycle, finishing the drive cycle at a low SOC. As the battery ageing is calculated after it is assumed the SOC is brought back to its initial value, the simulations with low k_{ers} includes one nearly full discharge and recharge, degrading the battery to a larger extent.

As in the evaluation of the energy consumption of the vehicle, it is of interest to study how the **battery degradation is affected by a different approach to placing the ERS sections**. The *relative* battery degradation between the ADA and EQU ERS placing methods is shown in Fig. 5.16. Each sub-figure shows two surfaces, $S_{non-filled}$ and S_{filled} , where each is defined as

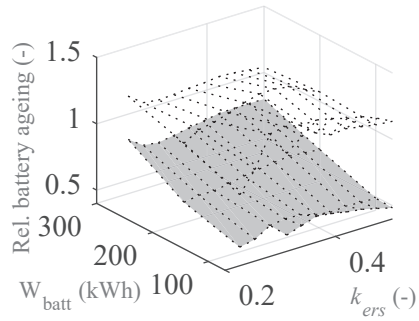
$$S_{non-filled} = \frac{B_{ADA}}{B_{EQU, d_{ers}=1km}} \quad (5.12)$$

$$S_{filled} = \frac{B_{ADA}}{B_{EQU, d_{ers}=10km}} \quad (5.13)$$

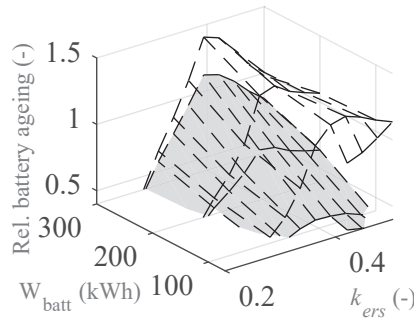
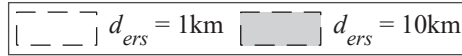
where S denotes the relative improvement of battery degradation and B the battery degradation per drive cycle. By defining S this way, they show how large an impact the ERS placing method impose on the battery ageing. A data point below 1 indicates that the battery is degraded less with the ADA placing method. Generally, the figure shows that the surface corresponding to the EQU placing with d_{ers} equal to 10 km (filled surface) is showing a lower relative degradation of the battery than when d_{ers} equals 1 km. This means that the ADA placing method is generally advantageous, from a battery degradation point of view, if the EQU method adopt a longer d_{ers} distance. 'Longer' in this context means a distance approaching a tenth of the total drive cycle distance. The difference imposed by the two ERS placing methods on the battery degradation are emphasized as the battery capacity becomes smaller suggesting that the ADA placing method cycles the battery to a lesser extent. This is also not unexpected as the ERS sections are placed where traction power is



(a) FIETS.



(b) HSETS, $P_{DC-DC} = 140$ kW.



(c) LSETS, $P_{DC-DC} = 60$ kW.

Figure 5.16: Relative battery ageing between the two ERS placing methods, as defined by Eq. 5.12 - 5.13, with MnSW control method and $P_{aux} = 2$ kW. A value below 1 indicates that the battery is degraded less with the ADA placing method.

required, then bypassing the battery. With an order of magnitude shorter d_{ers} distance, the battery degradation difference between ERS placing method (non-filled surfaces) is not as prominent. As shown in Fig. 5.15 a short d_{ers} is 'kinder' to the battery than when d_{ers} is long, meaning that the effective d_{ers} distance with the ADA method (although it does not feature such characteristic) is closer to 1 km rather than 10 km.

Regardless of the d_{ers} distance, the HSETS stands out slightly in comparison to the other two ETSs as the battery degradation is shown to be relatively unaffected by k_{ers} whereas in the other ETSs a clear effect is seen, especially as k_{ers} becomes small. This means that as the ERS sections are short, it is of extra importance to place them where they make the best

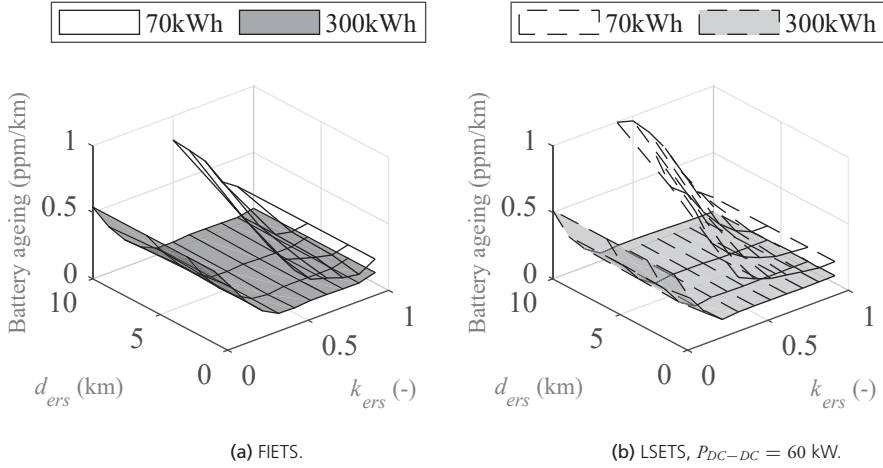


Figure 5.17: Fraction of battery life spent per drive cycle (%/ km) of the city bus. ERS is placed according to EQU, $P_{aux} = 2$ kW and the control method is MxRE.

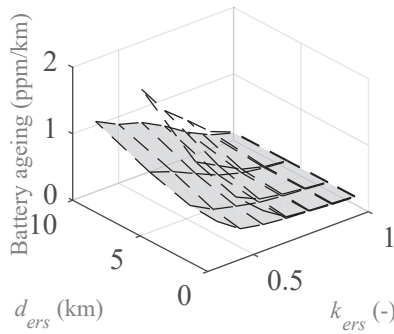
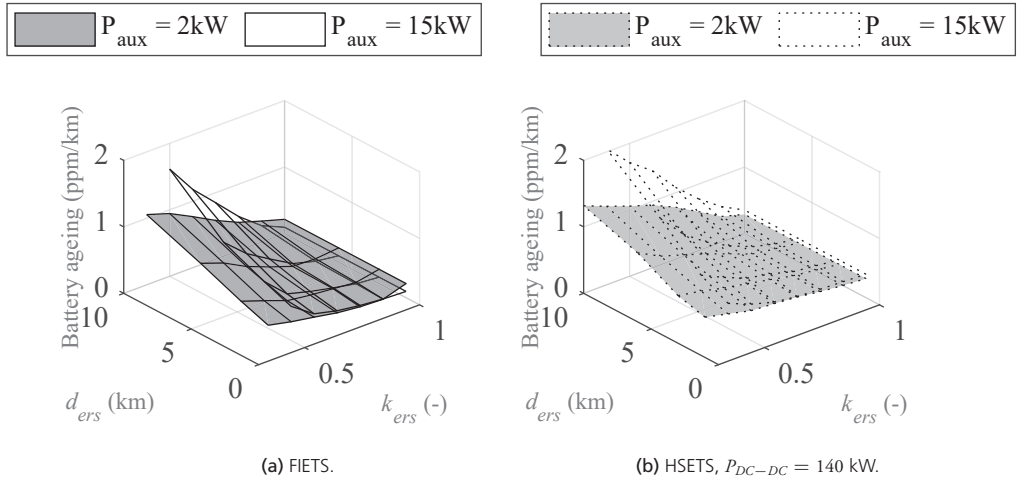
use, as where the most traction power is required for instance.

As it is shown that the **control method regarding regeneration of braking power** and switch box can affect the energy consumption, it naturally follows to evaluate if the control method has any influence on the battery degradation. Fig. 5.17 shows the battery degradation with vehicles utilizing the MxRE control method. It can be seen that, in comparison with Fig. 5.15, a significant difference cannot be concluded but rather, the behaviour of the battery degradation as function of k_{ers} and d_{ers} are largely similar regardless of control method. This further contributes to the overall conclusion regarding how the battery degradation is mostly affected by characteristics of the ERS rather than the components and structure of energy transfer method on-board the vehicle. However, one aspect on-board the vehicle is still influencing the battery degradation to a significant extent and that is the auxiliary load.

Fig. 5.18 shows how the battery degradation is affected by two different levels of auxiliary load with the lowest capacity battery in the parameter range, 70 kWh. As expected, the higher auxiliary load increases the battery degradation since the higher load will cycle the battery more deeply. Across the three ETSs, the relative increase of battery degradation is largely similar; an increase of approximately 60% is seen at low levels of k_{ers} and long d_{ers} distance.

5.5.1.3 Summary, City bus

The previous sections present and elaborate on the result of the simulation campaign regarding the city bus. As energy consumption and battery ageing is two of the main cost carrying posts of operating such a vehicle, these two quantities are the target of the result section. It is shown that the energy consumption to some extent is affected by the method



(c) LSETS, $P_{DC-DC} = 60\text{ kW}$.

Figure 5.18: Fraction of battery life spent per drive cycle (%/ drive cycle) of the city bus. ERS is placed according to EQU and the control method is MnSW.

of which the energy from the ERS is distributed between charging, traction, and auxiliary load. The different ETSs part of this evaluation shows strengths and weaknesses at different areas within the parameter set. For instance, if the relative ERS coverage is high, the ETSs which can feed the tractions drives directly from the ERS is benefited rather than if all the energy supplied by the ERS is fed through a DC-DC converter. Given the assumption that the ERS cannot receive electrical power, it has shown to be advantageous - from an energy consumption point of view - if the vehicles equipped with a switch box are allowed to rearrange its switch states during braking so that braking energy can be recuperated to the battery.

Besides the on-board ETS topology and control method, the characteristics of the ERS

is shown to also affect the energy consumption. Of the two ERS placement methods investigated it is shown that the method of placing the ERS sections where traction power is required the most is beneficial from both an energy consumption aspect as well as battery degradation aspect. It has to be mentioned, though, that only limited consideration to practical aspects have been taken when regarding the placement of ERS sections. Furthermore, it has been shown that the energy consumption is lowered, again mostly in cases where the ETS features the capability to operate its traction drives directly from the ERS, when the ERS sections are placed according to the traction power requirement.

Due to the nature of the drive cycle with an average low traction power requirement of the vehicles, an issue due to overloading of the traction machines does not arise.

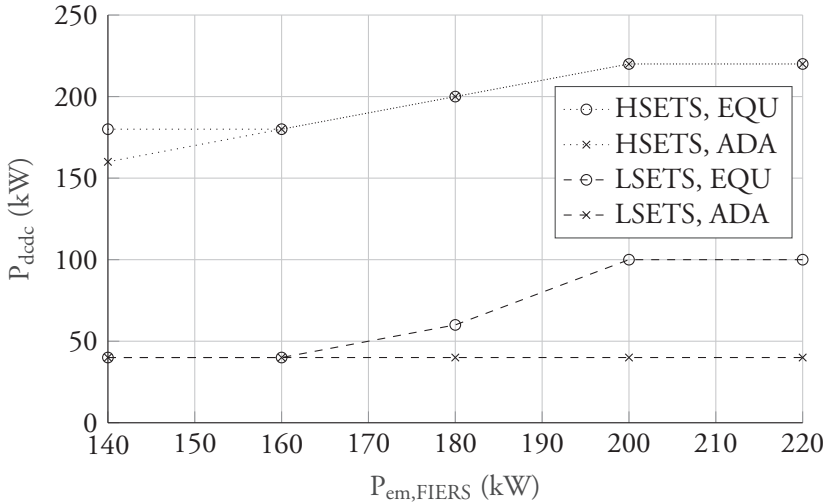


Figure 5.19: The minimum rated power of the DC-DC converter, $P_{DC-DC,min}$, required in the HSETS and LSETS in the 28 tonne long haul truck for a given rated traction drive power of the FIETS in order to obtain similar level of charging performance.

5.5.2 Long haul truck

Two versions of the long-haul truck are evaluated, one weighing 28 tonnes and one weighing 40 tonnes, otherwise the vehicles are similar. Results of either vehicle is shown where it is relevant. Where the result is similar, only data from one vehicle is shown to limit the number of figures. As opposed to the evaluation of the city bus, only one level of auxiliary power is evaluated as well as one method of regeneration/switch box control. This is due to the nature of the drive cycle as it consists mainly of constant speed travelling rather than start-stop-traffic as is the case with the city bus. The benefit of rearranging the switch box during braking is limited and deemed not to add any significant value to the study.

In order to adequately compare the performance of the three ETSs introduced in Chapter 2, a level of comparably equal charging performance has to be established. The FIETS is chosen to be the benchmark to which the HSETS and LSETS are compared to. As the FIETS does not feature a bespoke converter or similar specifically for charging, the rated power of the traction drives is used as the measure to compare with the rating of the DC-DC converter in either HSETS or LSETS. Data of the 28 tonne long haul truck is shown in Fig. 5.19 which shows the rated power of the DC-DC converter in the HSETS and LSETS as a function of rated traction drive power (of all three ETSs) required to achieve a similar level of charging performance as the FIETS at the given rated traction drive power. The result can be seen as a FIETS with rated traction drives at 160 kW, carries the charging performance equal to a 180 kW and a 40 kW DC-DC converter (regardless of ERS placing method) in the HSETS and LSETS respectively. It is also shown that the required DC-DC converter rating is not largely affected by the ERS placing with the HSETS whereas with

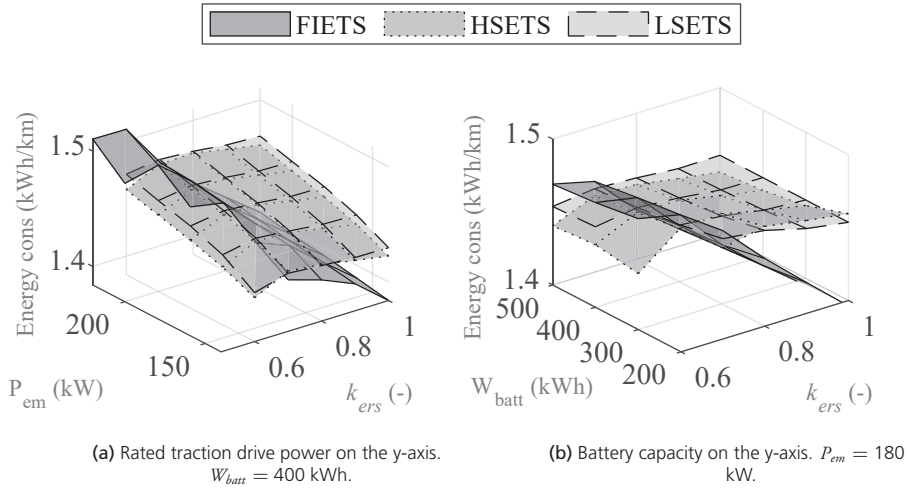


Figure 5.20: Energy consumption comparison of the 28 tonne LHT across the three ETs with EQU ERS placing.

the LSETS, the lowest rated DC-DC converter power is sufficient for all cases of rated traction power when the ERS is placed according to the ADA method. Based on Fig. 5.19, at a rated traction power of 180 kW a rated DC-DC converter power is chosen to 200 kW in the HSETS and 60 kW in the LSETS in the following result presented regarding the 28-tonne long haul truck, unless otherwise stated.

5.5.2.1 Energy consumption, 28 tonne LHT

The energy consumption of the 28 tonne LHT as a function of the relative ERS coverage and rated traction power and battery capacity is shown in Fig. 5.20. The difference in energy consumption between the three ETs with EQU ERS placing is shown to be limited to approximately 5% whilst the rated traction power affects the consumption to a larger extent than the capacity of the battery. A higher rating of traction drive power generally leads to moving the operating points to a lower efficiency of the traction drive, leading to higher consumption as rated traction power increase. A higher rated traction power might be either required or desirable based on other requirements. The battery capacity has a limited influence on the total energy consumption, a slight decrease can be observed as the capacity increases. A larger capacity battery generates a lower amount of losses compared to a lower capacity one, see Section 3.1.3. The relative ERS coverage does affect the FIETS the most. It is seen that the more ERS available, the more does the vehicle supply the traction drives directly from the ERS, regardless of vehicle speed, as opposed to the LSETS, which in turn decreases the energy consumption.

An illustration on how the ERS placing affects the energy consumption is shown in Fig. 5.21. Only a slight decrease in energy consumption can be observed with the HSETS whereas the LSETS and FIETS show a significantly bigger difference in favour of the ADA

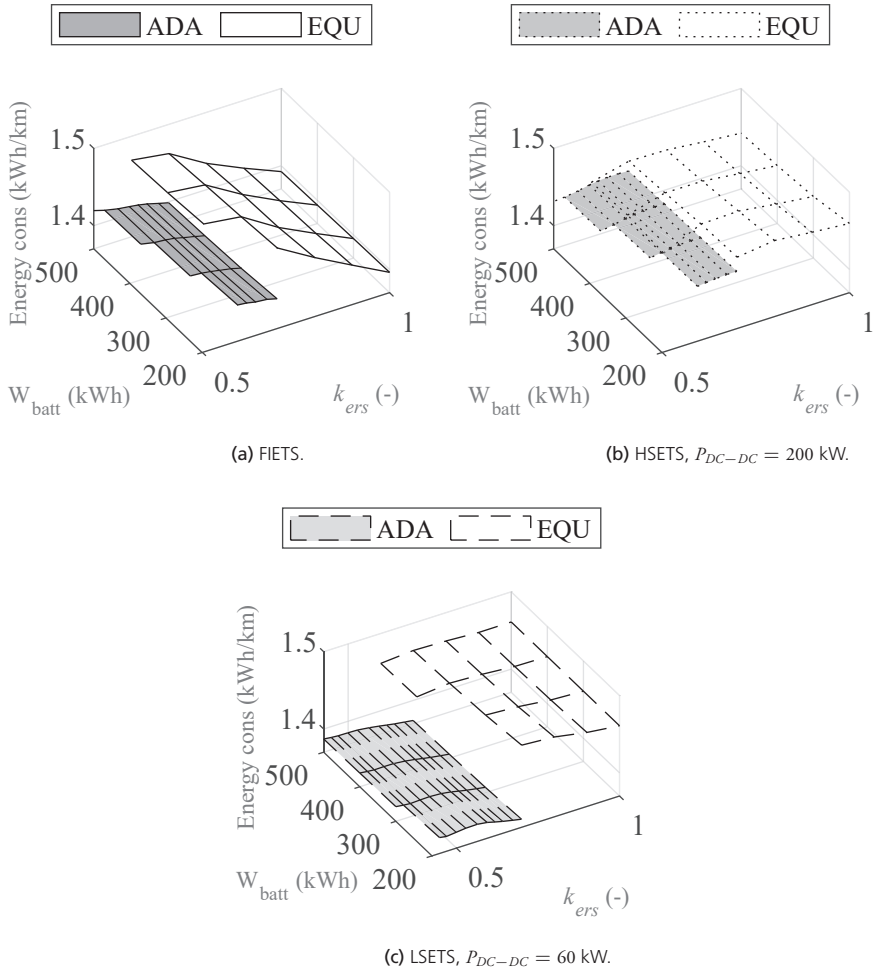


Figure 5.21: Energy consumption of the 28 tonne LHT with different ERS placing methods along the drive cycle. The higher consumption corresponds to the EQU ERS placing and the lower to the ADA ditto.

ERS placing method. This behaviour is not unexpected as the ETs that can supply its traction machines directly from the ERS will benefit the most if the ERS sections are generally placed where high levels of traction power is required. Worth noting is also that the LSETS is capable of completing the drive cycle at both a lower level of k_{ers} as well as a lower capacity battery compared to the FIETS and HSETS. This fact suggests that for long haul truck operations the LSETS topology is the preferred choice from an energy consumption perspective at the evaluated level of auxiliary load.

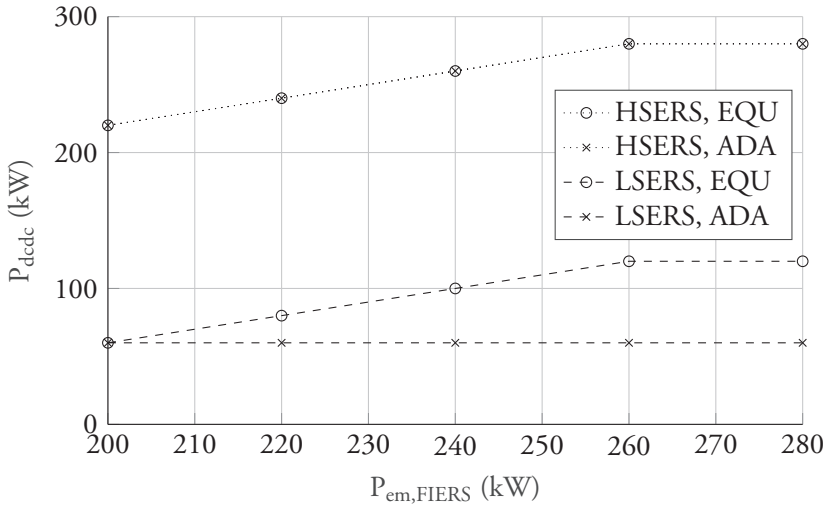


Figure 5.22: The minimum rated power of the DC-DC converter required, $P_{DC-DC,min}$, in the HSETS and LSETS powertrains in the 40 tonne long haul truck for a given rated traction drive power.

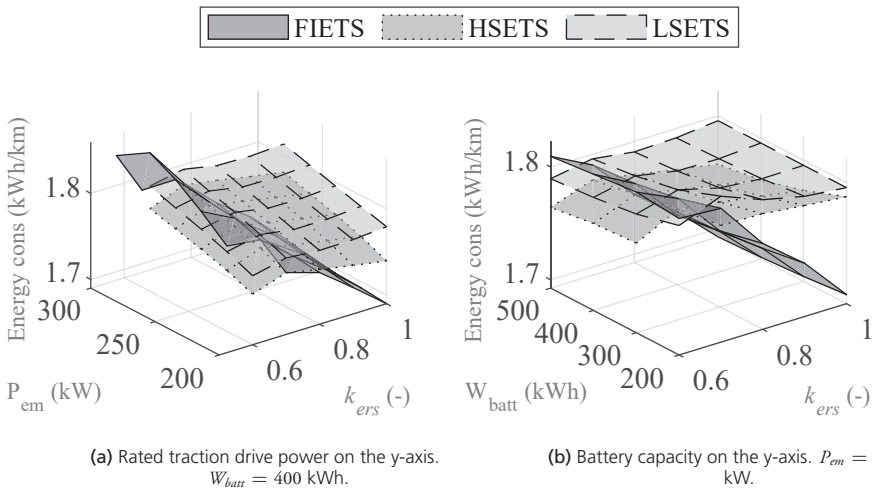


Figure 5.23: Energy consumption comparison of the 40 tonne LHT across the three powertrains with EQU ERS placing.

5.5.2.2 Energy consumption, 40 tonne LHT

A similar charging performance benchmarking as shown above for the 28 tonne LHT, is shown for the 40 tonne LHT in Fig. 5.22 shows. A similar behaviour can be concluded; the HSETS does require a similar level of rated DC-DC converter power regardless of ERS placing method whereas the LSETS is largely benefited by the ADA ERS placing as only the lowest level of rated DC-DC converter power is required regardless of rated traction drive power in the FIETS. Unless otherwise stated, the result regarding the 40t LHT feature a

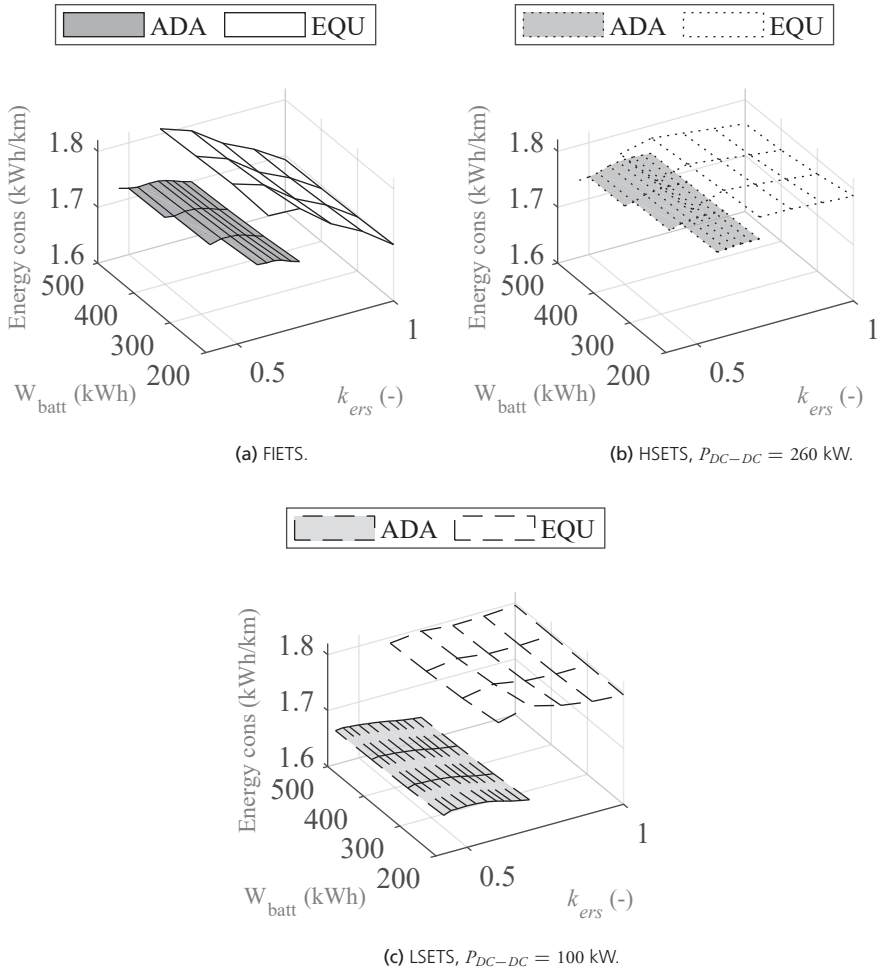


Figure 5.24: Energy consumption of the 40 tonne LHT with different ERS placing methods along the drive cycle. The higher consumption corresponds to the EQU ERS placing and the lower to the ADA ditto.

rated DC-DC converter power of 260 kW in the HSETS and 100 kW in the LSETS.

The energy consumption of the 40 tonne LHT is shown in Fig. 5.23 both as a function of the relative ERS coverage and rated traction drive power and battery capacity. The behaviour is similar to the 28t LHT as shown in Fig. 5.20 with the main difference being an expected, generally, higher energy consumption for the 40 tonne LHT. Also seen is that the difference between the HSETS and LSETS is greater when used in the 40 tonne LHT rather than the 28 tonne LHT. This is due to the fact that in the HSETS, all of the energy from the ERS has to be supplied by the DC-DC converter whereas the traction drives in the LSETS are able to be supplied directly from the ERS and as the total amount of energy required is higher in the 40 tonne LHT, the difference is emphasized.

The impact of the ERS placing on the energy consumption of the 40 tonne LHT is

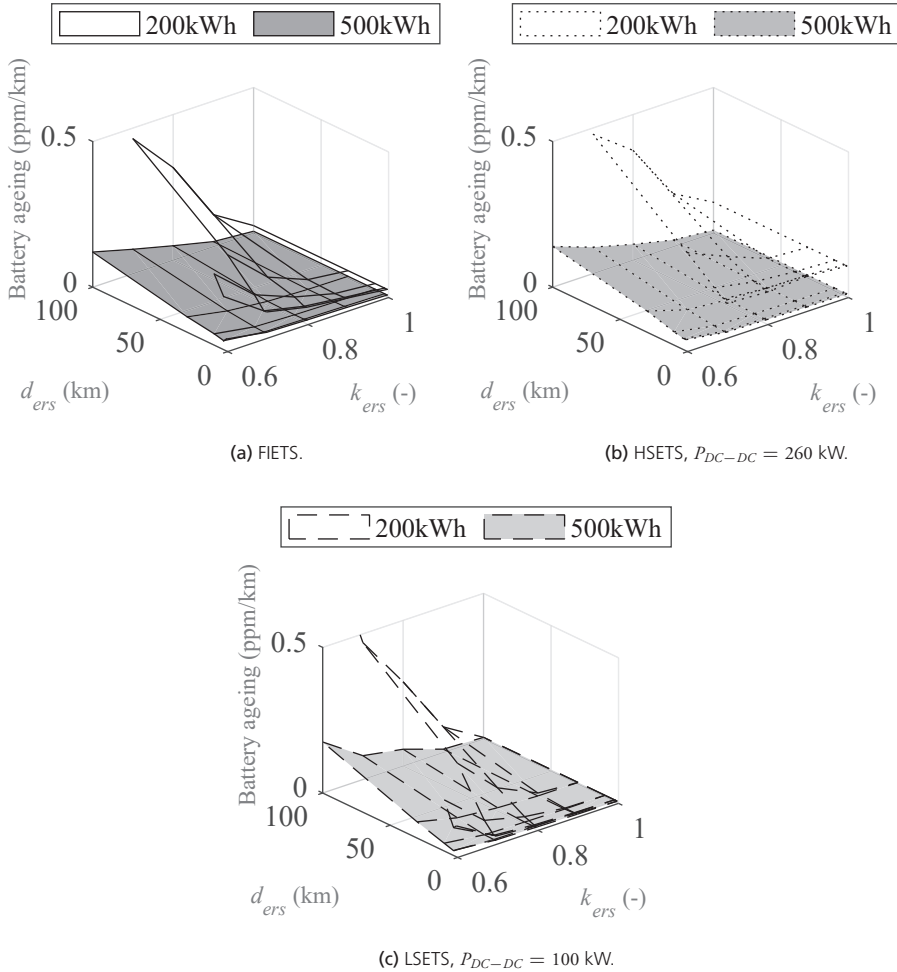
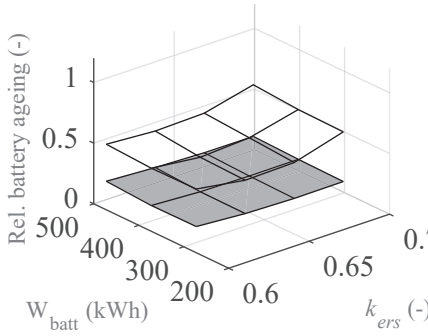


Figure 5.25: Fraction of battery life spent (%/ km) of the 40 tonne LHT with EQU ERS placing.

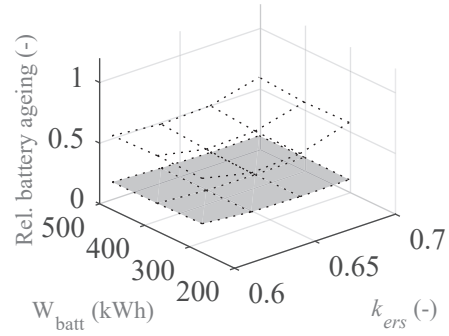
shown in Fig. 5.24 where, again, a similar behaviour as with the 28 tonne LHT can be seen. The LSETS benefits the most by the ADA ERS placing method, both regarding the absolute energy consumption but also by the fact that a smaller capacity battery and/or a lower level of relative ERS coverage is possible.

5.5.2.3 Battery ageing

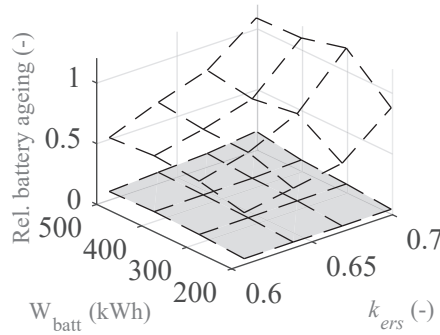
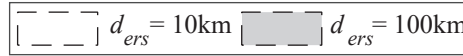
The evaluation of the battery degradation is only shown for the 40 tonne LHT as the result is similar between the LHTs and the 40 tonne LHT displays a 'worse' scenario of the two. Fig. 5.25 shows the battery ageing per drive cycle in ‰ of the three ETSs at two levels of battery capacity. The difference in battery ageing between the powertrains is not significant, albeit with the smaller capacity battery the HSETS displays a higher level of ageing compared to



(a) FIETS.



(b) HSETS, $P_{DC-DC} = 260\text{kW}$.



(c) LSETS, $P_{DC-DC} = 100\text{kW}$.

Figure 5.26: Relative battery ageing between the two ERS placing methods, as defined by Eq. 5.14-5.15 of the 40 tonne LTH.

the FIETS and LSETS. This is due to the fact that in the HSETS, the DC-DC converter, the traction drives, and battery are at all times electrically connected, meaning that energy constantly flows between these three components, in turn, leading to more cycling of the battery. The LSETS and FIETS however, disconnect the traction drives from the battery when possible and whenever doing so, decreasing the energy input/output of the battery significantly. Other than this difference, the same behaviour across the three ETSs can be observed; a larger capacity battery decreases the degradation as well as a short d_{ers} distance and high relative ERS coverage. This is all expected since a given cycle of absolute energy becomes a smaller relative cycle if the capacity of the battery increases, a long d_{ers} distance will inevitably lead to deeper cycles of the battery just as a lower relative ERS coverage will.

Apart from battery degradation due to the variation of k_{ers} and d_{ers} , it is also interesting to study the relative battery degradation from the two alternative ERS placing methods. Again, the data displayed relates to the 40 tonne LHT as the differences in result between the two LHTs are small, and data is only shown where the sets of k_{ers} overlap with both ERS placing methods. Fig. 5.26 shows a relative comparison of battery degradation between the ERS placing methods where each of the two surfaces, $S_{non-filled}$ and S_{filled} , in each plot is defined as

$$S_{non-filled} = \frac{B_{ADA}}{B_{EQU, d_{ers}=1km}} \quad (5.14)$$

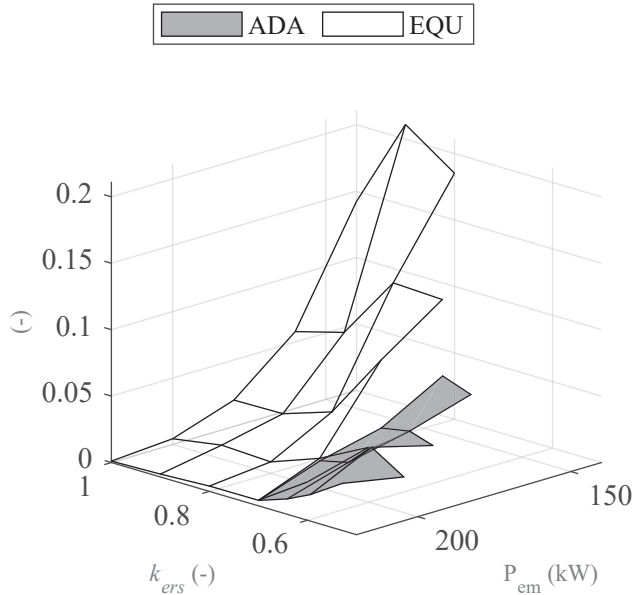
and

$$S_{filled} = \frac{B_{ADA}}{B_{EQU, d_{ers}=100km}} \quad (5.15)$$

where S is the surface and B is the absolute battery ageing per drive cycle, as per Fig. 5.25. This means that if a point on the surface is equal to 1, the battery degradation is equal between the ERS placing methods, a point below 1 means the degradation is lower with the ADA placing method than with the EQU. Generally, it can be concluded that the ADA placing method is the preferred one seen from a battery degradation point of view mostly regardless of the d_{ers} distance of the EQU. Mostly, because it is shown that with the LSETS, the degradation is comparable between the two placing methods for high levels of k_{ers} and a short d_{ers} (non-filled surface). Should the comparison stand between the EQU with a long d_{ers} (100 km in this case) and the ADA, the ADA is by far the better option where a reduction of battery degradation to approximately 15 – 20% can be seen across all three ETSs.

5.5.2.4 Overloading

A consequence due to the way energy is fed from the ERS to the traction drives and/or battery in the FIETS is running one of its traction drives at a high power (traction + charging), overload of the traction drive might occur. One way of partly mitigating overloading of one traction drive, is to share the load between the two traction drives, i.e., as one machine approaches a too high of a temperature; the switch box rearranges so that the other machine carries the high load. How the overloading of a traction drive is established is explained in Sec. 3.1.2. Depending on the drive cycle and/or charging need of the vehicle, both machines might enter the overload state at the same time. Fig. 5.27a shows how large a fraction of the total time of the drive cycle, *both* traction machines are overloaded in the 28 tonne LHT. The battery capacity and the d_{ers} parameter are found not to have a significant impact on the amount of time both machines are overloaded, which is why these are fixed at 200 kWh and 10 km respectively. The non-filled surface corresponds to the EQU ERS placing and the filled the ADA ERS placing. It is shown that in the worst-case scenario,



(a) The fraction of total time of the drive cycle both the traction drives are overloaded in the 28 tonne LHT.

more than a fifth of the time, both machines are overloaded. This occurs primarily when the rated traction drive power is low rather than high, which is to be expected. A certain decrease of the total overloading time can be seen as the relative ERS coverage is increased. When the ERS is available to a larger extent, the vehicle does not have to prioritize charging as much as if the ERS is only available to a lesser extent. For a given relative ERS coverage it can be seen that the ADA ERS placing method does not tend to overload the machines to the same extent as if the ERS were placed according the EQU method and that the difference is emphasized as the rated traction drive power decreases. This is due to the fact that if the ERS sections are placed where the traction power is required the most, the energy fed to the vehicle is consumed directly by the machines as one or both traction drives can be supplied directly from the ERS. The opposite would be to place the sections where traction requirement is low (as might very well occur with the EQU), meaning the traction drives are required to operate at high power during acceleration and up hills *as well as* during deceleration and down hills as the battery still needs to be charged, effectively doubling the time the machines has to supply high power and increasing the duration of overload.

The HSETS and LSETS which do not feature integrated charging, i.e., a separate DC-DC converter which care for the supply of energy to the battery, does not suffer from this issue to the same extent as the traction drives only supplies the traction power. With the lowest rated traction drive power investigated (120 kW) the relative time both machines

are overloaded only amounts to 1 – 2%.

This thesis does not investigate further whether a certain amount of time of the drive cycle is spent in an overloaded state is reasonable or acceptable but rather concludes that the time can be mitigated with a higher rated power of the traction drives and/or a more sophisticated approach to placing the ERS sections. Literature also suggests that there are methods of cooling of electrical machines that allows overloading to a larger extent [93], [94], [95].

5.5.2.5 Summary, LHT

The three ETSs introduced in Section 2 are evaluated in two versions of a long-haul truck from a charging performance, energy consumption and battery degradation point of view. The drive cycle used is a long distance, high average speed drive cycle, typical for long haul transport and the ERS is placed according to two different strategies, EQU and ADA, see Section 2.4. It is found that the weight of the vehicle does not alter the overall behaviour but rather generally introduces an offset on the outcome. In general, the choice of ETS and the method of placing the ERS affects the energy consumption significantly and also the vehicles' ability to complete the drive cycle with a given battery capacity. The battery degradation is only very slightly affected by the choice of ETS, however, the characteristics of the ERS and battery capacity are largely influential.

Aside the outcomes above, the FIETS is investigated with regard to whether the traction machines become overloaded due to the way energy is fed from the ERS to the battery. It is evident that the FIETS equipped with comparably low power traction drives, does in fact overload its machines to a significant extent.

The one parameter alone that affects both energy consumption, battery degradation and the over loading issue (in the FIETS) is the placing of the ERS sections. It has been shown that from all of the above points, placing the ERS sections where the traction power is required is advantageous.

5.6 Chapter summary

A city bus and two versions of a long-haul truck are modelled and simulated in a, for the vehicle type, relevant use case. The three ETSs introduced in Section 2 are evaluated in each vehicle in order to investigate how the on-board topology concerning traction and charging affects the energy consumption and battery degradation. One ETS (referred to as *Fully Integrated Energy Transfer System*, FIETS) features integrated charging, meaning components whose primary task is to propel the vehicle are also used in the process of transfer energy from the charging supply (ERS or AC grid) to the on-board storage. The two additional ETSs (referred to as *High power Separate Energy Transfer System*, HSETS and *Low power Separate Energy Transfer System*, LSETS) feature to a slightly different degree separate charging, meaning a bespoke component is installed on-board the vehicle solely

for the purpose of transferring energy from the supply to the on-board energy storage. Not only is the overall topology of the ETS altered but also the on-board control method and the rating of involved components such as rated traction drive power, battery capacity and so forth.

Besides the technology on-board the vehicle, the layout of the ERS is also a part of the study where the ERS sections are placed according to two different philosophies, 1) where equally long sections are placed an equal distance apart (referred to as EQU), and 2) where the sections are placed primarily where the traction power requirement is the highest (referred to as ADA).

It is found that the choice of ETS does affect the energy consumption to some extent. However, possibly more important is that different characteristics of the ERS is shown to affect the energy consumption to a significant extent. For instance, the impact of changing the relative ERS coverage largely affects the energy consumption of the FIETS and LSETS whereas the HSETS remains comparably unaffected. As the HSETS is comparably unaffected by the placing of the ERS, the average energy consumption seen with the HSETS over the two different placing methods is higher than what the FIETS and LSETS produce. If the use case dictates a significant amount of start-stop traffic it is also shown that the energy consumption can be significantly lowered if the vehicle is allowed to regenerate kinetic energy to the battery, which is not necessarily always a possibility, depending on ETS topology.

With regard to battery degradation, the impact of altering the ETS is low, in this case the characteristics of the ERS and the battery capacity are the main influencers. A long distance between the ERS sections in combination with a relatively low-capacity battery ages the battery to a larger extent than the opposite, which is quite expected.

The sole parameter that is shown to affect all of the investigated outcomes the most is the method that dictates where the ERS sections are placed. It is shown that if the ERS sections are placed where the requirement of traction power is the highest, i.e., on inclines and typical places of acceleration, both energy consumption, battery degradation and required battery capacity are affected, generally for the better. This result suggests that when considering electrifying the on-road transport by means of electric roads, it is important to consider the effects of the location of the ERS sections.

Chapter 6

Common mode current validation and analysis

As is elaborated on in previous chapters, the FIETS is capable of energy transfer from both an AC grid as well as a DC source (ERS). The way of which the energy is transferred is different from traditional methods of charging of EVs, which is why it is interesting to evaluate how the FIETS performs from an EMI/common mode current perspective.

This chapter presents and compares measurement result with modelling result of the common mode current that arise while emulating/simulating *static* charging with the FIETS, meaning the floating chassis is connected to protective earth. Measurements are performed on both isolated and non-isolated charging as is illustrated on a high level in Fig. 4.3 whilst both set-ups are modelled using Matlab/Simulink with Plecs [70]. Detailed schematics of the experimental setup is shown in Appendix A.4 which constitutes exactly what is modelled with Plecs *except* the parasitic capacitance which does not exist as a physical component in the physical system. Two models are developed based on the physical system, 1) where only the AFE (including passive filters and so on) acts as the interface between the grid supply and the battery, i.e., non-isolated charging and, 2) where the full system of the FIETS with its AFE and two mechanically coupled traction drives are utilised for the transfer of energy from the grid to the battery (emulator/model), i.e., isolated charging. The physical system is designed in such a way so that it can easily be reconfigured between isolated and non-isolated charging. More details on the modelling of the physical system are presented in Section 3.2.

Common mode (or, zero sequence) current is generally undesirable as it might cause safety equipment to trip, cause EMI challenges or become a potential danger if safety equipment is not present. The common mode current arises due to the common mode voltage that is present in switching systems as elaborated on in Chapter 2 and Fig. 2.3. The presence of parasitic capacitance creates a path for the common mode current back to the source which in this case is a neutral grounded three phase supply. The phenomenon is illustrated

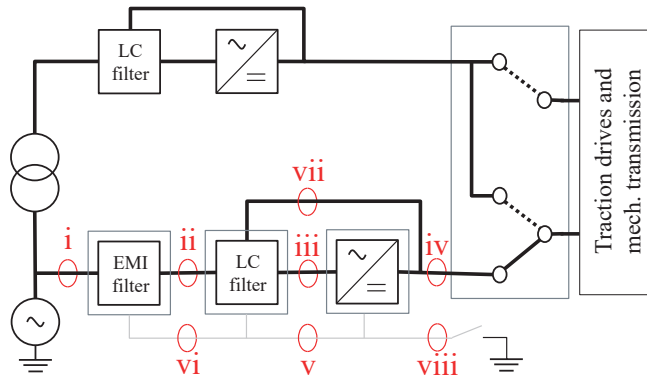


Figure 6.1: Measurement set-up of the common mode current where 'i' - 'viii' shows the measurements points. Identical to Fig. 4.13, repeated here for convenience.

in Fig. 3.11 and 3.12.

The following sections present the measurement result of isolated and non-isolated charging at idle power and at approximately 20 kW, measured at the supplying grid followed by modelling result in comparison with measured result and an evaluation of what characteristics of the model which generates the most accurate simulation result. An analysis is also made of how an increase of parasitic capacitance at the traction voltage system on-board a vehicle might affect the common mode current on the supplying grid side. This is done in the simulation environment as the experimental setup is measured for one level of parasitic capacitance.

All of the measurements and simulations are performed at a DC-link voltage of approximately 700 V.

6.1 Measurement results

The currents are measured using an oscilloscope sampling at 20 MS/s with a suitable current transducer. One period of the fundamental frequency (20 ms at 50 Hz) is shown and for each position a harmonic content analysis is performed using the Matlab 'fft' function [96]. The switch box of the experimental set-up is configured to either connect the active front-end directly to the battery emulator (non-isolated charging) or to one of the traction drives whilst the other traction drive is connected to the battery emulator (isolated charging), see Fig. A.7. Firstly, the measurement result from the non-isolated charging setup is presented followed by the isolated charging measurement result. Data from every measurement position, Fig. 6.1 (identical to Fig. 4.13, repeated here for convenience) is presented, including the phase current at the supplying grid. A compilation of the fundamental and

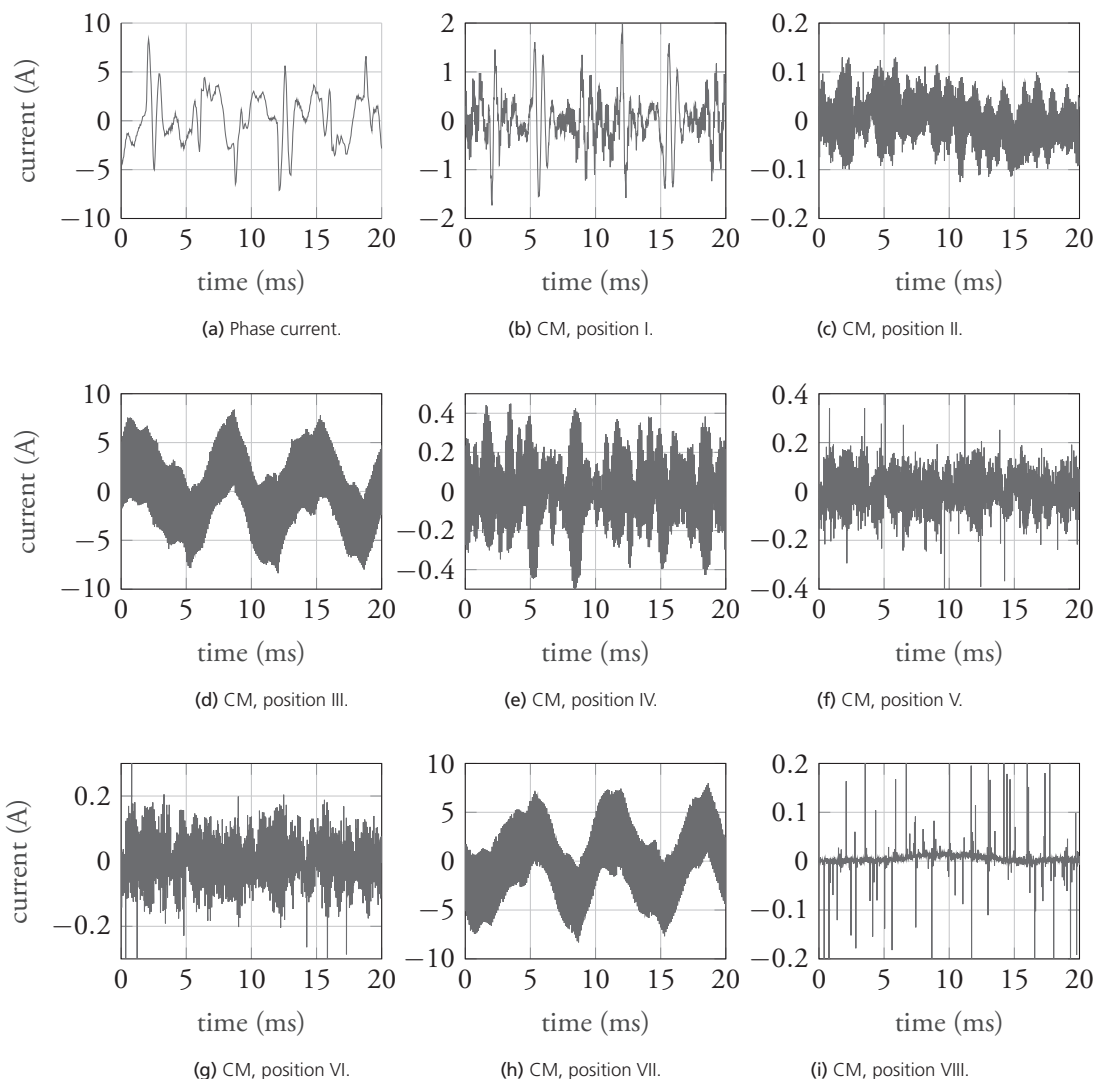


Figure 6.2: Measured currents at 'idle' with the non-isolated charger.

harmonic content is shown in Table 6.1.

Fig. 6.2 shows the measured currents at the specified positions when emulating non-isolated charging. Fig. 6.2(a) shows the phase current of one of the phases whereas figures, (b)-(i), shows the common mode currents. The current measured at position I is the common mode current from the grid, meaning the cause of a tripping RCD circuit breaker can be observed here. The active front-end converter is switching; however, no power is actively drawn from the grid. At most of the sampled positions of the circuit, a high frequency component is shown. However, between the active front-end converter and the common

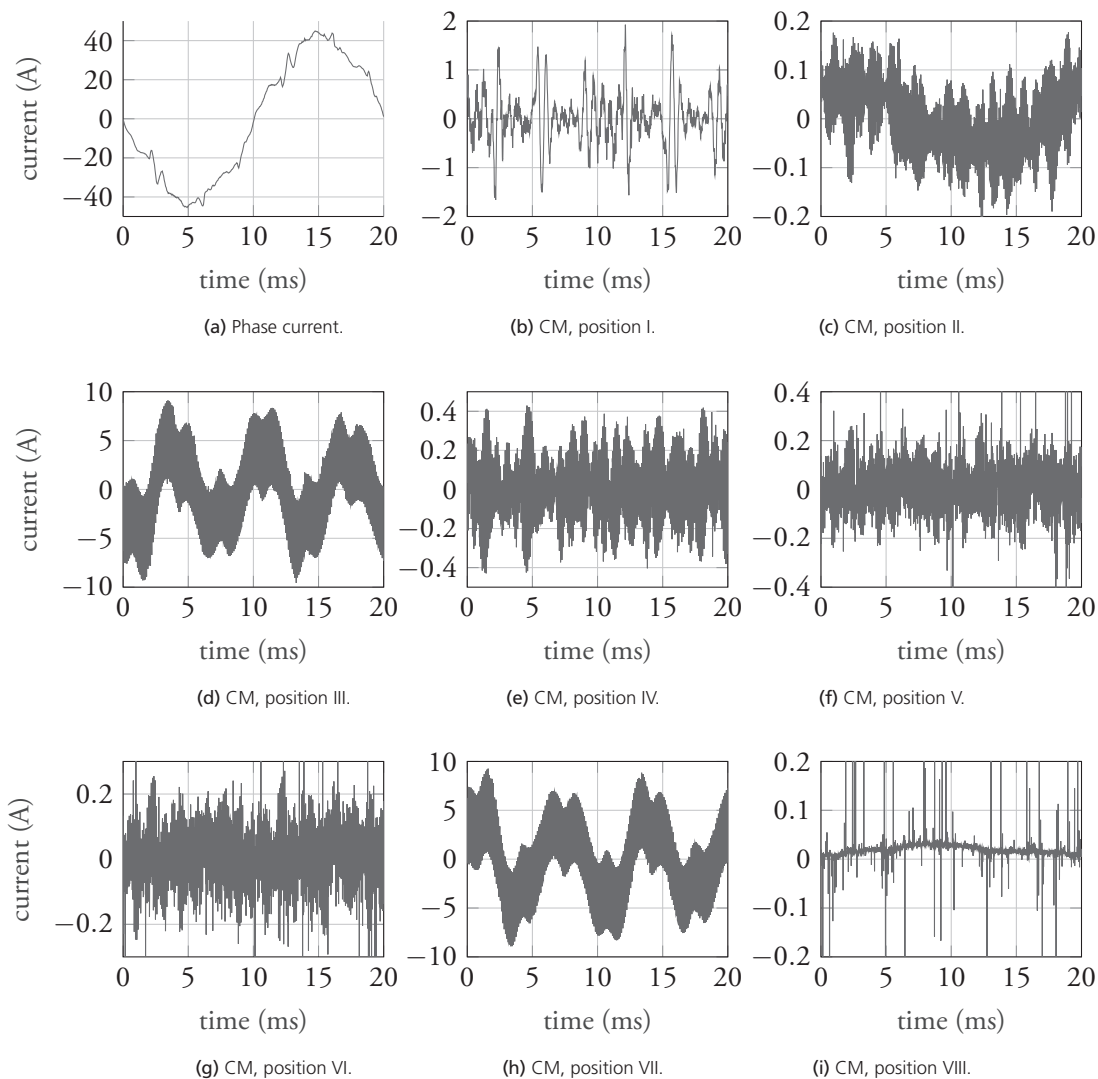


Figure 6.3: Measured currents at 20 kW with the non-isolated charger.

mode filter, position III and VII in Fig. 6.1, a prominent 3rd harmonic is present. The origin of this harmonic is elaborated on when discussing the modelling result.

When consuming approximately 20 kW of power from the grid, the corresponding currents turn out to what is shown in Fig. 6.3. It is clearly seen that the common mode currents are in the same order of magnitude even though the power level is increased substantially. This suggests that the common mode current arises mainly from the switching of the converters in combination with the circuit layout, i.e., the created common mode voltage as illustrated by Fig. 2.3 and is not largely affected by the power level consumed

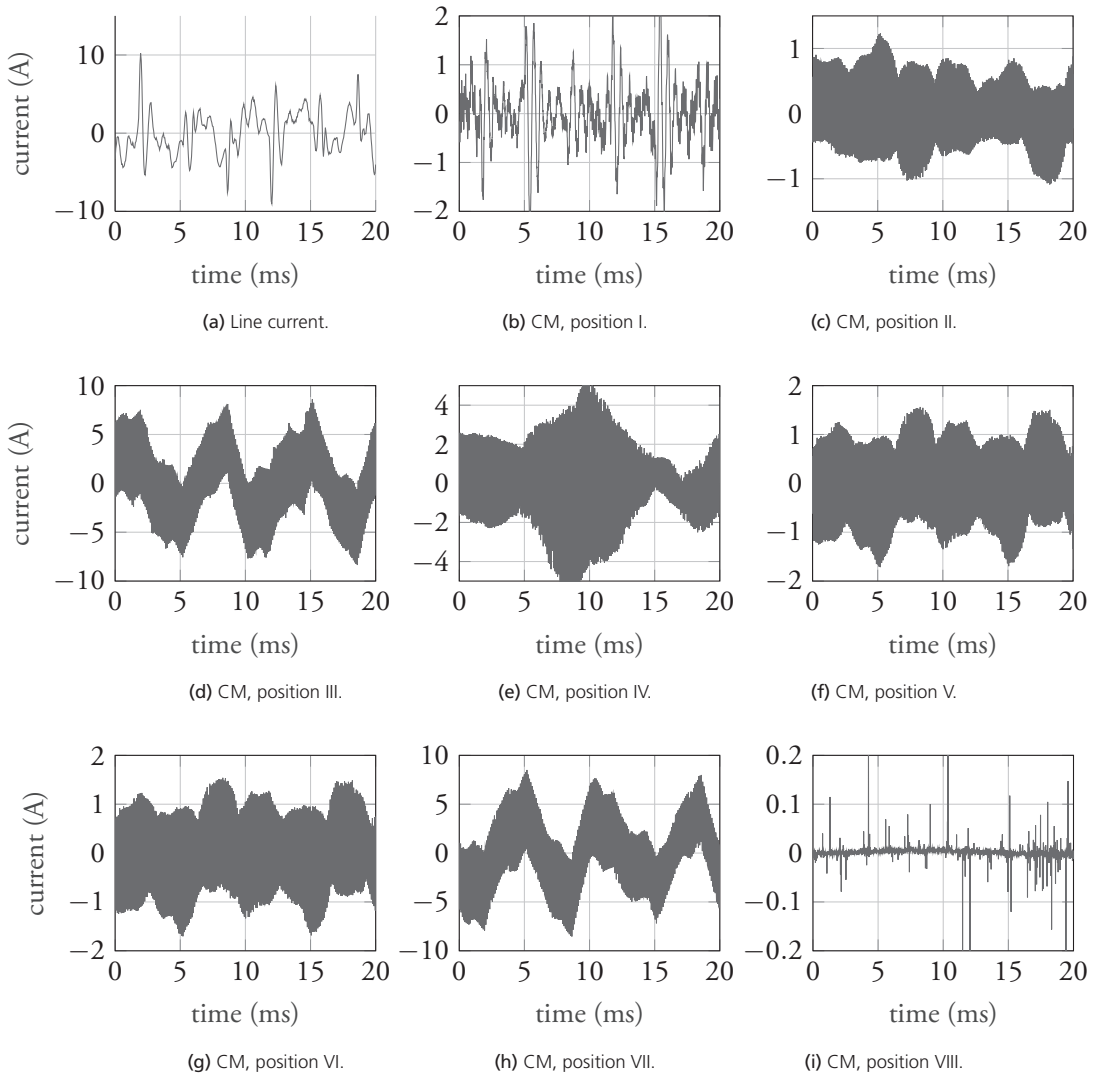


Figure 6.4: Measured currents at 'idle' with the isolated charger.

from the grid.

The corresponding measurement when emulating isolated charging is shown in Fig. 6.4. In this case, the active front-end converter and both traction drives are switching although no power is actively transferred to the battery emulator. Similarities to the currents of the non-isolated charger are clearly seen although differences, especially observed at position II and IV-VI where the common mode current is higher in the isolated case, which possibly is unexpected. This will be elaborated on later in this section.

As the power is increased to approximately 20 kW, the common mode currents of the

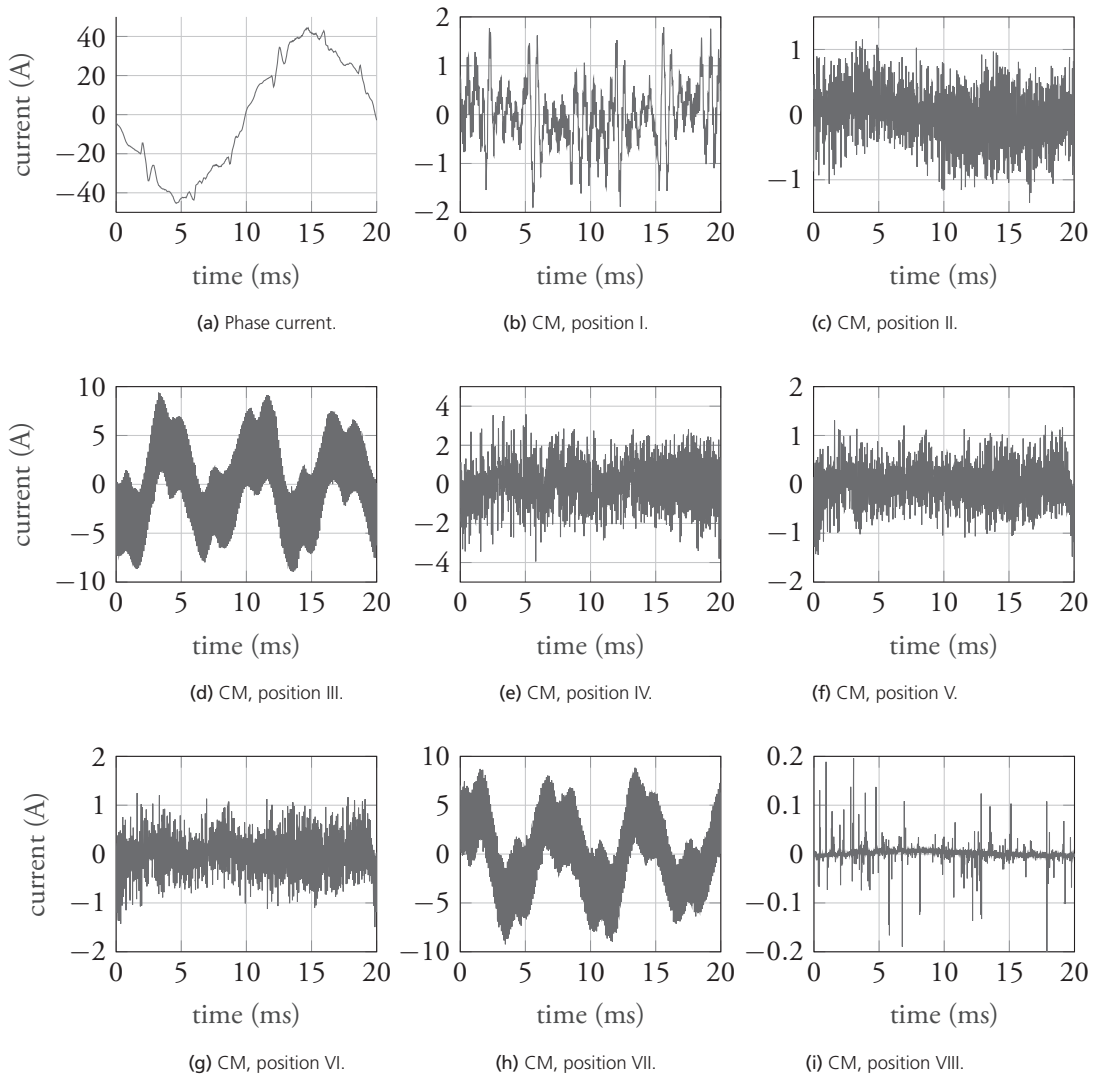


Figure 6.5: Measured currents at 20 kW with the isolated charger.

various positions of the charger circuit turn out to what is shown in Fig. 6.5. As is the case with the non-isolated charger, the difference in common mode current is not substantial as the grid power is increased. As this is observed, and expected, in both charger modes, the data of the 'idle' case is hereinafter mainly used in the validation of the modelling of the chargers.

All of the measured currents are analysed with a Fourier transform in order to assess the harmonic content of each of the positions in the circuit. Table 6.1 shows the RMS of the current as is, the RMS of the fundamental part of the current and also the RMS of

Table 6.1: RMS, fundamental and harmonic current.

	measurement position	non-isolated			isolated		
		I_{rms} (A)	$I_{fundamental}$ (A)	$I_{harmonic}$ (A)	I_{rms} (A)	$I_{fundamental}$ (A)	$I_{harmonic}$ (A)
'idle'	Phase current	2.57	0.14	2.54	2.81	0.71	2.69
	I	0.55	0.02	0.52	0.66	0.07	0.62
	II	0.04	0.01	0.0	0.43	0.01	0.01
	III	3.56	0.05	2.4	3.61	0.04	2.45
	IV	0.16	0.0	0.0	1.35	0.0	0.01
	V	0.09	0.0	0.0	0.66	0.0	0.0
	VI	0.08	0.0	0.0	0.65	0.0	0.0
	VII	3.49	0.06	2.39	3.52	0.05	2.44
	VIII	0.05	0.0	0.0	0.02	0.0	0.0
20kW	Phase current	29.9	29.76	2.84	29.09	28.92	3.11
	I	0.54	0.02	0.52	0.64	0.19	0.56
	II	0.07	0.04	0.01	0.42	0.13	0.02
	III	4.04	0.15	3.02	4.08	0.16	3.05
	IV	0.16	0.0	0.0	1.09	0.03	0.17
	V	0.11	0.0	0.0	0.43	0.01	0.08
	VI	0.1	0.0	0.0	0.42	0.01	0.09
	VII	3.99	0.17	3.01	3.98	0.18	3.03
	VIII	0.07	0.01	0.0	0.03	0.0	0.0

the non-fundamental current. It is seen that the currents levels are comparable between the charger modes and charging power at a given measurement position. Notable is that the phase current mainly consists of harmonic content rather than the fundamental when the charging power is low. The level of harmonic content in the phase current remains relatively constant as the charging power is increased to approximately 20 kW (emphasized by red colour in the Table). This behaviour is also seen in the common mode currents. As observed in Fig. 6.2-6.5 the highest level of common mode current appears at position III and VII, which are the cables connecting the DC-link between the AFE and the common mode filter (emphasized by green colour in the Table). This is not unexpected as the purpose of this connection is to reduce the common mode voltage swing of the DC-link. It is also evident that the CM currents in positions II, IV, V and VI are an order of magnitude higher in the isolated converter than in the non-isolated. The main difference between the two

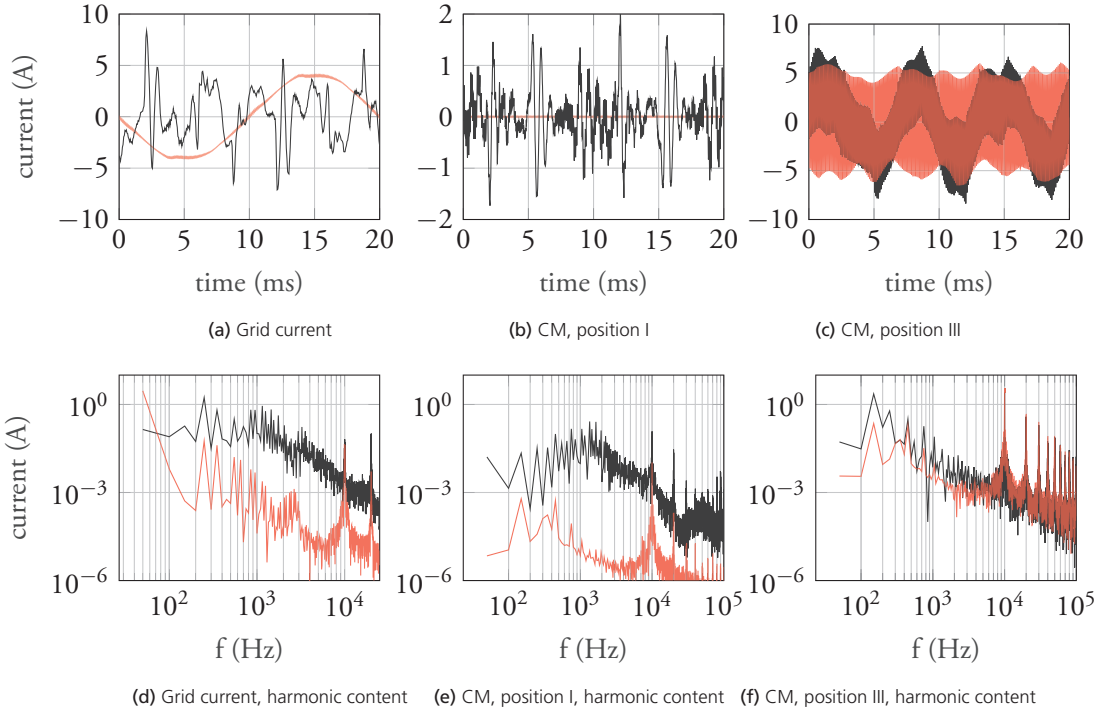


Figure 6.6: Measured (black) and simulated (red) currents at 'idle' with the non-isolated charger.

is that the motor drive of the isolated converter is a source of CM currents that find their way in the ground via the EMI-filter. The common mode current measured at position I (blue colour in the Table) are similar in all cases; a possibly more expected outcome is that the isolated charger generates measurably lower common mode current. This is elaborated more in detail in the following section.

6.2 Model validation

This section elaborates on a detailed level on the validation and adaption of the charger models to the measurement result. First, a basic slightly idealised model is evaluated, followed by stepwise introduction of non-idealities in blanking time of the transistor switches and phase voltage harmonics. The non-ideal characteristics are added to the model to fit the measurements to the simulated results and thus trace what feature of the model is resulting in a certain characteristic of the measured currents. The versions of the model simulations are presented in Table 6.2.

Showing the current of all measured positions takes an unreasonable amount of space which is why only the phase current and the common mode current of position I and III in Fig. 6.1 are shown when evaluating the different features of the model. Fig. 6.6 shows

Table 6.2: Vehicle data.

iteration	characteristic
1.	'ideal'
2.	actual grid voltage
3.	blanking time of the converter
4.	actual grid voltage and blanking time of converter

the three measured currents and their corresponding harmonic content. It is obvious that the measured and simulated currents do not match to a great extent except the apparent commonality at the switching frequency, 10 kHz, where a clear peak occur in both simulated and measured currents. This result is to be expected as the model, at this point, is a somewhat idealised version of the reality.

The following part of this section shows figures of the same structure as Fig. 6.6 where a certain aspect of the model is altered as described above. Firstly, the supplying phase voltage is replaced by the real, measured voltage as shown in Fig. 3.13 followed by a version where a blanking time is added to the AFE converter. Finally, the result of a model containing both these imperfections is also evaluated.

As stated in Section 3.2, the model can in addition to an ideal voltage source also be **supplied with a recording of the real, measured voltage**, as shown in Fig. 3.13. The result of this is shown in Fig. 6.7 where it is shown that the harmonic content of the phase current as well as the common mode current, measurement position I in Fig. 6.1, is increased substantially over the whole frequency spectrum (in relation to what is shown in Fig. 6.6). Note in particular that the 5th and 7th harmonic of the phase current matches the measured current significantly better in this case rather than when the supplying voltage is a clean sine wave. At position III the harmonic content is also elevated to conform to a greater extent with the measured current suggesting that a substantial part of harmonic content can be mitigated with a 'clean' supplying voltage. In reality, the grid voltage is never a perfectly clean sine wave, containing only the fundamental frequency. There are multiple possible sources of harmonic distortion on the low voltage grid, for instance, photo voltaic inverters, EV chargers and electric heat pumps to name a few [71], [72]. Both active and passive rectification of the grid cause harmonics, albeit utilizing active rectification with proper control and filtering the harmonics can be kept reasonably low [97], [98].

Blanking time in a switching converter is the time when the upper and lower transistor in one leg is turned off simultaneously. A blanking time is necessary in order to mitigate shoot through of the DC-link, however, it does lead to non-ideal current wave forms [99]. There are methods of limiting the effect of the dead-time [100], [101], [102], however none is implemented in the control software used in these measurements/simulations. The effect of the blanking time is seen in Fig. 6.8, especially on the common mode current at position III where a pronounced 3rd harmonic is present, very similar to the measured current. A

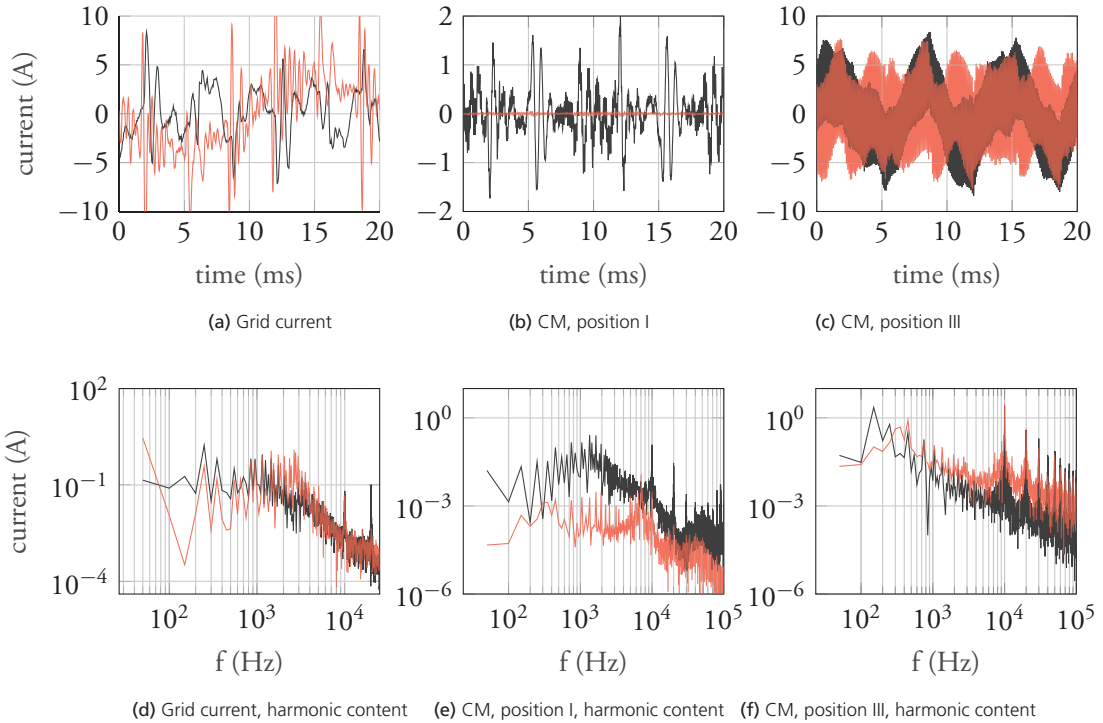


Figure 6.7: Measured (black) and simulated (red) currents at 'idle' with the non-isolated charger with actual grid voltage.

5th and 7th harmonic are also emphasized in the phase current. However, the common mode current at position I is not largely affected by the addition of blanking time in the converter.

When both the imperfections of the supplying grid and the blanking time are included in the model, the simulated currents turn out to what is shown in Fig. 6.9. It is shown that the phase current and harmonic content at position III matches reasonably well. The simulated common mode current at position I does not match the measurements greatly; a 3rd harmonic is shown but between the 3rd harmonic (150 Hz) and the switching frequency (10 kHz) the simulated current is substantially lower than the measured current. The reason for this is not fully understood. A possible reason can be various switched power supplies connected to the grid in the vicinity of the supply to the laboratory facilities.

The procedure of adding one characteristic of the model at the time in order to evaluate how the current is affected is also done in the case with the isolated charger model. It is found out that the behaviour does not differ from what is shown with the non-isolated charger which is why only the result of the model containing all the considered imperfections is shown. Fig. 6.10 shows the measured and simulated currents of the isolated charger at low power. Similarly, to what is shown with the non-isolated charger in Fig. 6.9, the harmonic content of the measurement and simulation of the phase current and

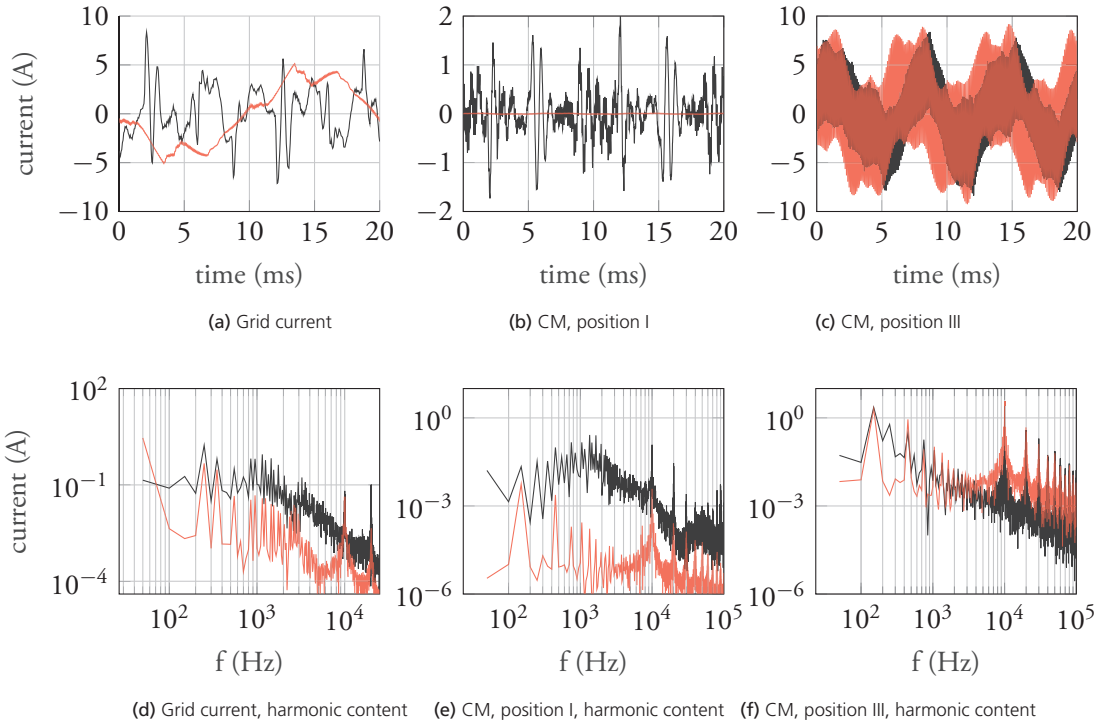


Figure 6.8: Measured (black) and simulated (red) currents at 'idle' with the non-isolated charger with blanking time in the converter.

at measurement position III matches reasonably well. However, at measurement position I, the simulation is not able to catch all the frequencies of the measured current. Worth noting, though, is that both the measurement and simulation suggest that the common mode current at position I in Fig. 6.1, i.e., the common mode current the grid supplies, is larger when utilizing isolated charging rather than non-isolated charging. This is possibly not what one would expect since one of the purposes of isolated charging is to mitigate the common mode current. The probable reason for this is that the parasitic capacitance of the TVS, i.e., the battery emulator, of the measurement setup is so low (at the battery emulator, the parasitic capacitance is measured to approximately 100 nF/pole) that a significant current does not arise in the non-isolated connection. And, on the other hand, in the case of isolated charging, the parasitic capacitance of the electric machine does affect the common mode current to a larger extent, so that the gain of have isolated charging is lost, when regarding only the common mode current at least.

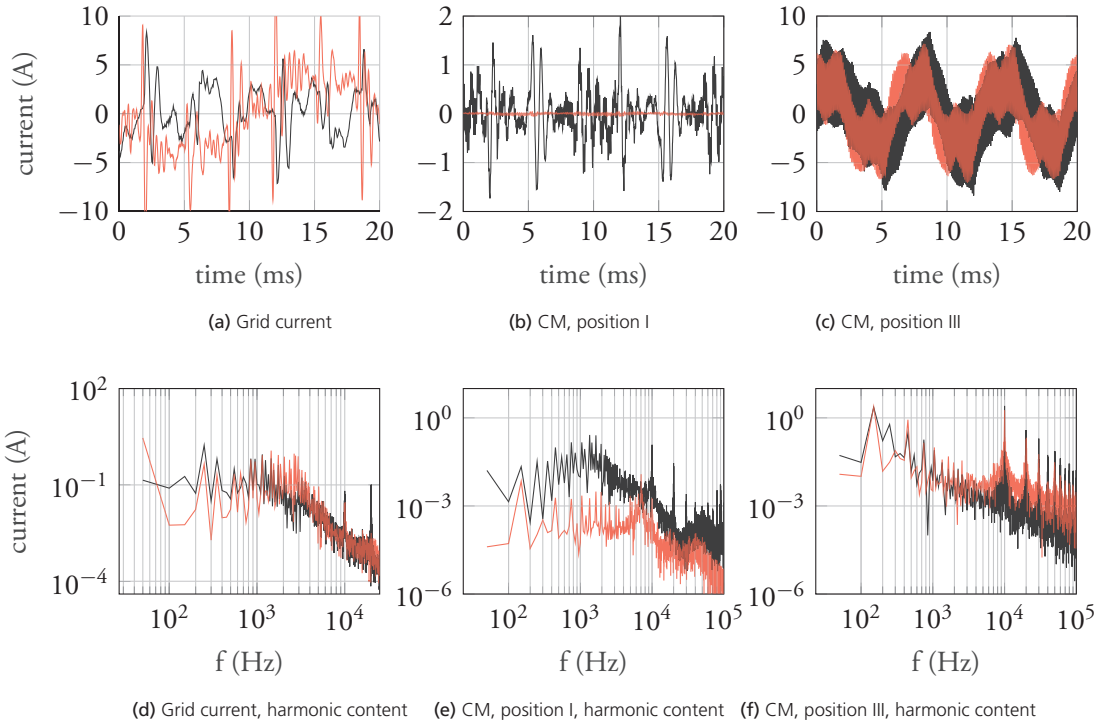


Figure 6.9: Measured (black) and simulated (red) currents at 'idle' with the non-isolated charger with both non-idealities included.

6.3 Analysis

The main goal of modelling a physical system is to adjust certain parameters of a validated model and be able to somewhat trust the result without having to rebuild the physical system. This is done with the charger models. The non-isolated charger is here modelled with different levels of parasitic capacitance, C_{par} of Fig. 3.11, at the TVS whereas the isolated charger is modelled with different levels of parasitic capacitance at the 'primary' electric machine, illustrated in Fig. 3.12.

A larger parasitic capacitance at the TVS is expected to amount to a larger common mode current when utilizing non-isolated charging from the grid. The non-isolated charger is modelled with either 100 nF/pole (as measured) or 1.5 μ F/pole (expected order of magnitude in a real vehicle installation) at the TVS in order to verify and quantify this. Fig. 6.11 shows the common mode current at position I, position IV (the DC-connection between the AFE and the battery emulator) and position VIII (the current to ground) of Fig. 6.1. It is clearly seen that a higher parasitic capacitance at the TVS increases the common mode current at the presented positions of the circuit, which is to be expected. It is shown that an increase of the parasitic capacitance of approximately one order of magnitude can increase the common mode current at certain frequencies up to as much as three

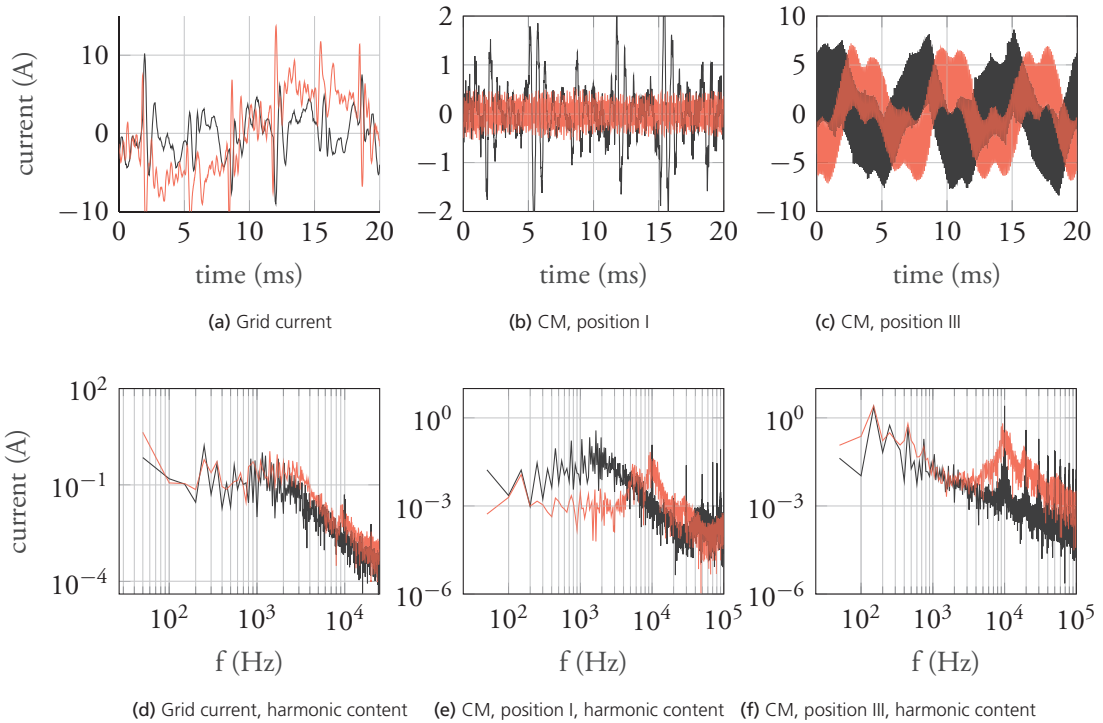


Figure 6.10: Measured (black) and simulated (red, 7nF/phase) currents at 'idle' with the isolated charger with both non-idealities included.

orders of magnitude. This verifies that it may be desirable to keep the parasitic capacitance at a minimum even though other aspects may need the opposite, to keep CM currents close around the DC/AC converter [103]. However, in many cases the possibility to reduce parasitic capacitance is limited. There are methods of possibly limiting the common mode current without necessarily reducing the parasitic capacitance at the TVS. Using the non-isolated charger as an example, in order to reduce the common mode current at the grid, for a given amount of parasitic capacitance at the TVS, one could force the common mode current into a return path at the primary side of the AC/DC converter (the AFE in this case) by deliberately connecting capacitors between the phases and ground [103]. This way, the common mode current does not appear at the grid supply but rather circulates within the LC-filter and AFE itself. This kind of analysis, however, is not done in this thesis.

Just as interesting it is to evaluate how the parasitic capacitance at the TVS affects the common mode current with a non-isolated charger, equally important it is to evaluate how said capacitance at the 'primary' electric machine affects the common mode current with the isolated charger. Fig. 6.12 shows the common mode current at position I, IV and VIII of the isolated charger at two different levels of parasitic capacitance at the 'primary' electric machine. It is seen that an increase of the parasitic capacitance at the TVS, C_{par} in

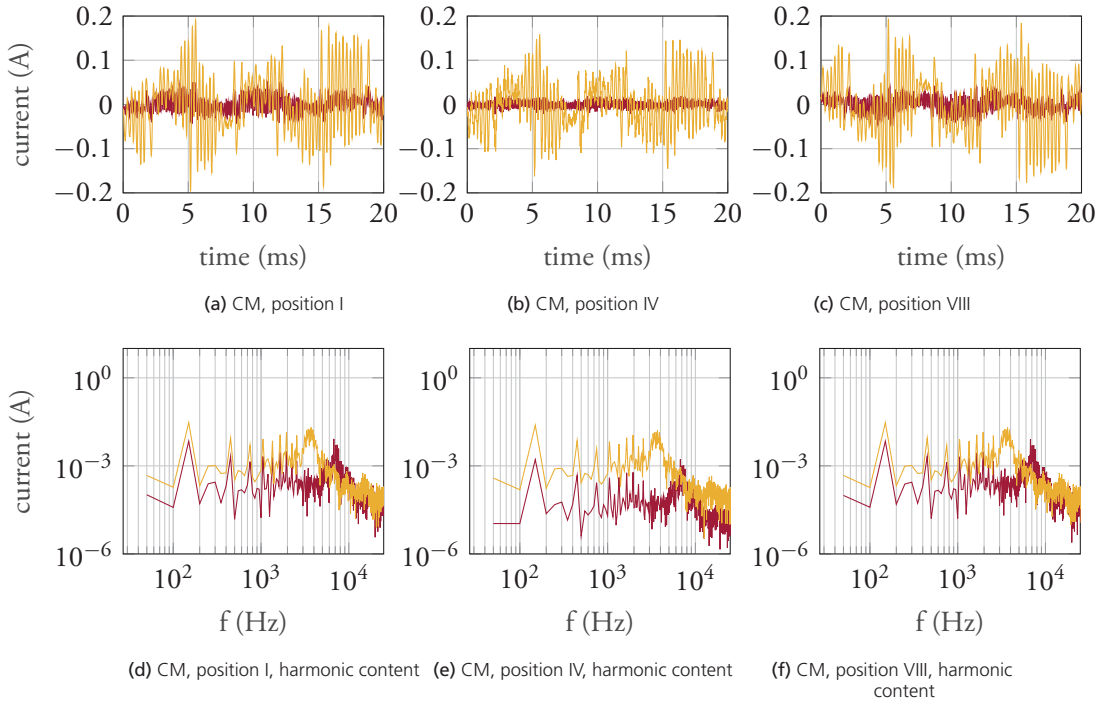


Figure 6.11: Simulation result of the common mode currents at measurement position I, IV and III of the non-isolated charger with different levels of parasitic capacitance, 100 nF/pole, 1.5 μ F/pole at the TVS.

Fig. 3.11, of a factor 2-3 does increase the common mode current. However, observing the frequency spectrum of each current it is seen that the difference mainly occurs at higher frequencies as well as in the region between 200-400 Hz. Overall, what can be concluded from this is that the dimensioning of the grid interface with the isolated charger evaluated in this thesis might, as tested, not be optimal from a parasitic current due to parasitic capacitance point of view. The main reason being that the voltage across the parasitic capacitance of the electrical machine is fluctuating with the switching frequency at an amplitude of $U_{DC}/2$. The voltage fluctuation across the parasitic capacitances at the TVS when emulating non-isolated charging is, due to (thanks to) the LC-filter and EMI-mitigating components within the converter, significantly lower. This means, even though the capacitances at the TVS are numerically larger, a smaller amount of current is conducted through them. In [103] these phenomena are studied in detail on an on-board electrical system where it is shown that an increase of capacitance at the DC-link for a given amount of (parasitic) capacitance at the electric machine can actually decrease the common mode current at the battery. This theory can be adapted to the system(s) studied in this thesis; the capacitance of the LC-filter would then represent the parasitic capacitances of the electric machine in [103] whilst the parasitic capacitance at the DC-link in this system represents the intentionally placed capacitances in [103]. With this in mind it can be argued that the

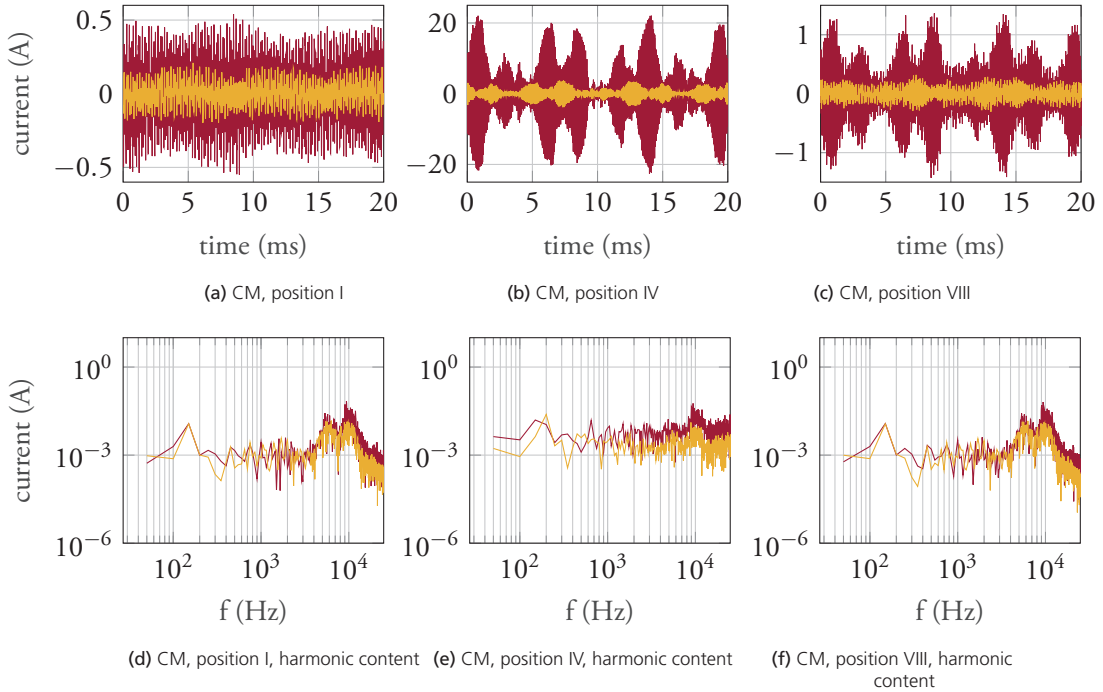


Figure 6.12: Simulation result of the common mode currents at measurement position I, IV and III of the isolated charger with different levels of parasitic capacitance, 2 nF/phase, 7 nF/phase at the 'primary' electric machine.

common mode current at the grid decreases when non-isolated charging is emulated since a larger amount of capacitance is introduced at the DC-link compared to when isolated charging is emulated. It should be noted that the main purpose of evaluating the FIETS experimentally is not the electrodynamics but rather proves the concept in terms of usage on an electric road, as discussed in previous chapters. This means that the design of the filters is not made with minimizing possible common mode currents as first priority. Taking the whole system into consideration, the LC-filter should be possible to design so that at least the same performance can be expected from a common mode perspective of both the isolated and non-isolated charging systems. From an electrical safety aspect, the isolated charger does regardless of EMI performance still have an advantage over the non-isolated alternative.

In an attempt to benchmark the non-isolated and isolated charger from a common mode current due to parasitic capacitance point of view, Fig. 6.13 is presented where the phase current and common mode current at position I is shown of both charger topologies. It is found that to match the frequency spectrum between the topologies, the larger value of the TVS parasitics corresponds approximately to the smaller value of the electric machine parasitics.

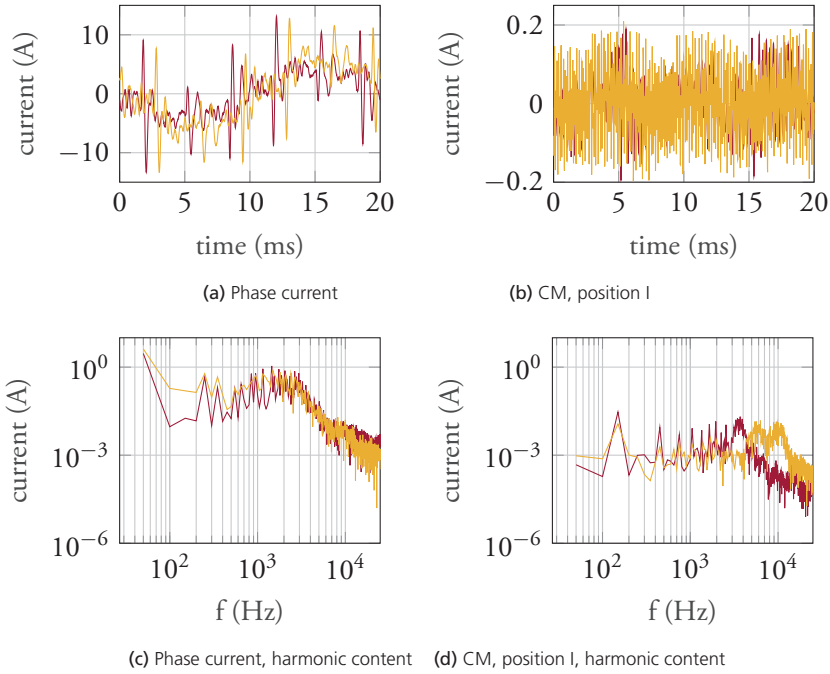


Figure 6.13: Comparison of currents of the **non-isolated charger** ($C_{par} = 1.5 \mu\text{F}/\text{pole}$ at the TVS) and the **isolated charger** ($C_{par} = 2 \text{ nF}/\text{phase}$)

6.4 Chapter summary

This chapter is evaluating the ETS featuring integrated charging, presented in Chapter 2, from a parasitic current due to parasitic capacitance point of view. Both experimental measurements and modelling results are presented and compared and both isolated and non-isolated energy transfer is performed. In both cases the floating chassis of the ETS is connected to earth, as shown in Fig. 4.13, which would normally be the case when statically charging a vehicle. The phase current from the grid and the common mode current at various point of the ETS are measured in order to evaluate how and where the common mode current manifests itself in the circuit. Furthermore, the model of the ETS is validated with respect to the measurements by adding certain features of 'imperfections' to the - from the start - close to ideal model. It is shown that imperfections of the grid voltage and the dead/blanking time of the grid connected three phase converter largely affects the common mode current and its harmonic content.

Also presented is that, though not expected, non-isolated energy transfer results in a smaller amount of common mode current at the grid supply when compared to isolated energy transfer, if using the exact same grid interface. This is mostly due to the fact that the parasitic capacitance of the electric machines - windings to chassis - largely affects the common mode current, implying that if the goal is to minimize common mode current

at the grid supply, the parasitic characteristic of the electric machines has to be taken into consideration in this kind of topology when it comes to the design of the grid filter(s). With proper consideration the isolated and non-isolated chargers should be able to perform on a similar level from an EMI perspective. Although, considering the topology of the FIETS, the effect of the parasitic capacitance on the TVS, i.e., the energy storage, possible auxiliaries and so on, is removed thanks to the galvanic isolation interface utilized by the two electric machines. This means that less consideration to the parasitics of the system 'beyond' the galvanic interface has to be taken. In turn meaning that the FIETS could be fitted to a number of different vehicle types with different specification of the TVS (battery size, auxiliaries, etc) without having to be adapted to a specific vehicle from an EMI perspective.

Chapter 7

Conclusion and continuation

An Electric Road System (ERS) is the technology of transferring electrical energy to a moving vehicle. The purpose of the general concept is that by enabling energy transfer to a moving vehicle it reduces the requirement on a large capacity on-board storage which in turn can reduce the cost of the vehicle. Depending on how the energy flow is administered on-board the vehicle, the energy consumption is potentially lowered as well, motivating the adoption of ERS even further. In this thesis, conductive ERS is in focus and with that comes a number of challenges, mainly regarding safety as a connection to protective earth cannot be guaranteed. Energy transfer to a moving vehicle by means of an ERS is referred to as *dynamic* energy transfer.

It is concluded that energy transfer to a vehicle usually requires, on a block diagram level, roughly the same components regardless of whether inductive, conductive, dynamic or static energy transfer is considered. The source is the AC-grid, and the destination is the energy storage. In between, stages of rectification, high frequency AC generation, a magnetic coupling and rectification and power/current control is required. Either all of these stages are part of an on-board charger (OBC) and thus on-board the vehicle or, all stages are off-board (such as in high power DC-charging) or some parts are off-board and some parts are on-board (as in energy transfer from an ERS, inductive or conductive). If conductive ERS is considered, the components required are usually contained in one device, an isolated DC-DC converter. Should high power transfer capabilities be desired, the components related to the stages above adds up to both a significant physical weight and size and also cost. Therefore, it is desirable to utilize equipment already required for traction purposes also for energy transfer from the grid/ERS in order to reduce the need of costly and space demanding equipment. This way of utilizing existing equipment for several purposes is referred to as *integrated* charging or energy transfer.

This thesis work presents and evaluates different methods of energy transfer to an electric vehicle from a conductive electric road system. Different energy transfer systems (ETs) are considered and evaluated from an operational cost perspective, where quantities such as energy consumption and battery degradation are of main interest. One of the ETs is of

particular interest in this work since it features a novel way of achieving high transfer power, galvanic isolation as well as being integrated with the traction components. The components contained, as per above, in either an OBC or a DC-DC converter and the functionality they provide are in this ETS partly distributed among the traction components. This is made possible by utilizing two traction drives (converter and electrical machine) interconnected mechanically via the mechanical transmission of the vehicle. By adding a device allowing the DC-link of each traction drive independently connect to a supply - be it a DC fast charger or an ERS - and the energy storage, the supply and energy storage become galvanically separated as the two traction drives act as a rotating transformer. Furthermore, high power levels can be achieved as the maximum power transfer capability is only limited by the rated power of the traction drives. A prototype is developed of said ETS in order to prove the concept idea in terms of functionality, energy transfer efficiency and dynamic controllability as well as in order to develop a model of it to put into a drive cycle simulation context. The ETS featuring integrated energy transfer capabilities is referred to as 'Fully Integrated Energy Transfer System (FIETS)'. In order to put the FIETS into context, two additional ETSs are included in the study, both of which feature an isolated DC-DC converter. In one of them the DC-DC converter transfers all of the energy supplied by the ERS (of DC fast charger), hence the rated power of it is required to be high, in the range of several hundreds of kilo watts if heavy duty transport is considered. This ETS is referred to as 'High Power Separate Energy Transfer System (HSETS)'. The second additional ETS featuring a DC-DC converter is a combination of the two aforementioned in the way that it comprises both a DC-DC converter and a device allowing the traction drives to be supplied directly from the ERS. In the latter case, galvanic isolation of the on-board electrical system is not achieved, however it does enable the DC-DC converter to be rated at relatively low power levels. This ETS is referred to as 'Low Power Separate Energy Transfer System (LSETS)'.

Experimental verification of the FIETS suggests that the functionality is promising enough to be considered as an alternative for dynamic energy transfer. Although, the outright charging efficiency (from supply to energy storage) is lower in comparison to what can be expected from the HSETS and LSETS due to the increased number of conversions of energy. However, the overall energy consumption when put into a real drive cycle scenario is not necessarily higher due to its ability to run its traction drives directly from the ERS supply. The simulation study of the three ETSs considered in this thesis display a different behaviour with regard to the relative ERS coverage of a drive cycle as well as the approach to where the ERS sections are placed. This is mainly due to the assumption that the ERS cannot receive energy, i.e., when a vehicle is supplied by the ERS and *could* regenerate energy due to a velocity decrease or a downhill, this is not done but instead the friction brakes are used and energy is lost. In order to evaluate the value of being able to regenerate braking power, different control approaches are investigated in the ETSs where this is applicable. A significant decrease of energy consumption is shown, where the trade-off being heavier usage of the switching devices.

Different behaviour with regard to the ETSs in different driving and vehicle scenarios is also established as both a city bus on a low speed, city traffic drive cycle and a long-haul truck on a high speed, motorway drive cycle is investigated. It is shown that the difference in terms of energy consumption is emphasized when the vehicle is subject to a dynamic driving scenario rather than a monotonous one.

Furthermore, it is shown that a given installed rated traction power in FIETS (which is related to the vehicles' ability to receive power from the ERS as well as traction performance) corresponds to a significant amount of rated power in a separate power supplying method, i.e., in the HSETS and LSETS suggesting that the FIETS to some extent exhibits a certain charging performance 'for free'.

In addition to the system level analysis of ETSs the experimental setup of the FIETS is also utilized in order to attempt to quantify the impact of parasitic capacitance on parasitic, common mode, current. The experimental setup can be configured in such a way that energy transfer from the grid to the energy storage (a battery emulator in the setup) can be achieved either through the electrical machines (as described above) i.e., galvanically isolating the supply and energy storage, or through a non-isolated active front end converter (can be regarded as a non-isolated OBC). As the on-board high voltage system can be physically large in a heavy vehicle due to battery capacity requirements, HVAC systems, cabling and so on, the parasitic capacitance that comes with it cannot necessarily be neglected. Non-isolated energy transfer could then possibly lead to a level of common mode current that might trip safety circuitry, i.e., affect the up-time, cause EMI concerns or even cause potentially dangerous situations. Isolated energy transfer can mitigate the impact of the parasitics on the *isolated* side of the on-board high voltage system as a path through ground is eliminated. Measurements suggest that in the setup developed this difference could not be observed when comparing non-isolated and isolated energy transfer. This is likely due to the fact that the design of the experimental setup is not done with mitigation of common mode currents as a top priority. With proper design of filter components at least the same performance can be expected by both charger types from an EMI perspective. Though, it should be noted that the isolated charging system has its significant benefits over the non-isolated when considering electrical safety. Furthermore, what the measurements provide, is validation for the developed simulation models where certain aspects of the components and their control can be related to certain harmonic content of the common mode current. As well as an estimate on how the common mode current is affected by different levels of parasitic capacitance present at the high-voltage system.

7.1 Future work

There are a number of areas where a continuation of the work presented in this thesis can be valuable. Considering the experimental setup developed during this thesis work, there are aspects that can be improved in order to gather, 1) more operating points and 2) more accurate data. Some of these aspects are listed below.

- Replace the resolver interface so that higher rotational speed of the machines can be achieved. As of today, the maximum achievable speed is approximately 7000 rpm which is lower than what the machines themselves are rated for. Achieving higher speeds would extend the current data and lead to an extended torque/speed map of the machines.
- Replace the battery emulator with an actual battery. Due to safety reasons this was not possible in the experimental setup developed during this thesis work. However, should this be possible, a more realistic scenario is created since the battery emulator - constituted by a grid connected converter - imposes certain limitations regarding power and dynamics. However, the existing system has a number of advantages such as that different voltage levels are easily achieved. One attractive alternative would be to add another 'channel' of the switch box and connect a battery to it, in that way both systems could co-exist.
- The perhaps obvious continuation of the present work would be to validate the functionality and performance of the proposed energy transfer system(s) in a vehicle which would create great opportunities for measurement and validation. As there are a number of test sites of conductive electric roads in operation in Sweden, the possibility is not unreasonable.

Appendices

Appendix A

Electrical schematics and implementation

A.1 Battery model and emulator

The battery emulator is in the experimental set up similar to the AFE with its filters towards the grid. The main difference being that a three-phase isolation transformer is connected in between the grid supply and the LC-filter in order to galvanically isolate the battery emulator supply from the grid. The battery modelled at a significantly lower level, with an ideal DC-source with a series resistor and a parasitic capacitance to the chassis at each pole. The circuits are shown in Fig. A.1-A.2.

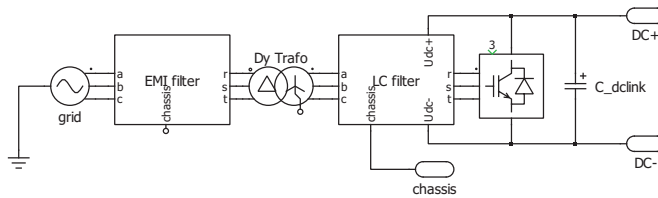


Figure A.1: The circuit of the battery emulator.

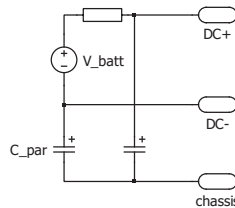


Figure A.2: The model of the battery emulator.

A.2 Double isolation

In the experimental setup presented in Chapter 4, the traction drives, electrical machines, filters and so on all have to be double isolated from the grounded chassis. The grounded chassis is constituted by the electrical cabinets, the mechanical transmission, the cooling pipes and so on. This means that the components that are part of the floating chassis has to be fitted with an extra layer of insulation as illustrated by Fig. A.3 and A.4 below. In addition to the extra insulation Fig. A.3(b), a flange (a) is installed in order to house the isolated axle coupling fitted in between the output of the electrical machine and input of the mechanical transmission.

Fig. A.4 shows how components of the floating chassis is mounted in the electrical cabinets, i.e. the grounded chassis. Isolating mounts (red) are used for mechanical fitting inside the cabinets between the mounting wall and the chassis of the converter. Also shown is the hose (blue) carrying coolant to the converter since a metallic pipe cannot be used.

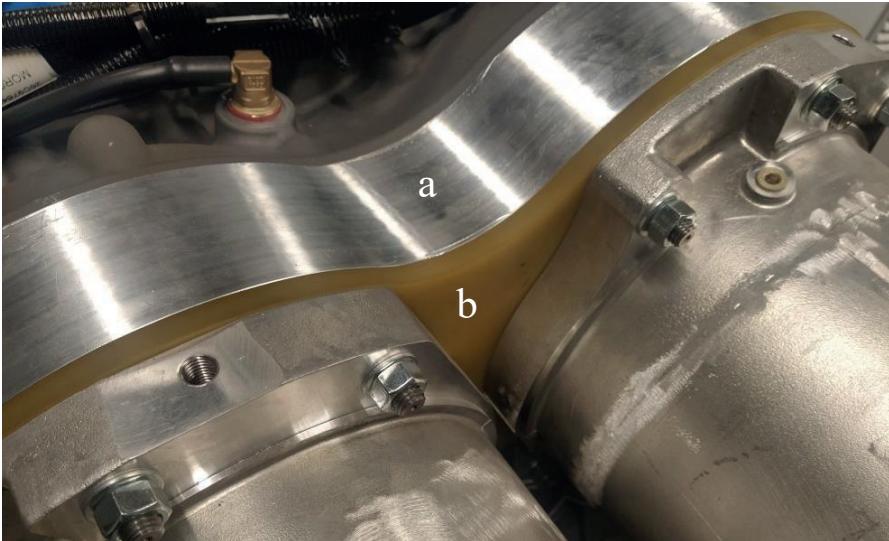


Figure A.3: Dielectric material installed in between the housing of the electrical machines and the mechanical transmission housing (b) and additional flange (a).



Figure A.4: The mounting of the traction converter in the electrical cabinet. The red mounting points are isolators. The blue hos in the foreground the coolant supply to the converter.

A.3 EMI filter

The schematics of the EMI-filter is shown in Fig. A.5. It should be noted that this is not an exact model of the EMI-filter used in the experimental setup as a complete data sheet is not available. Rather, the value of the components is partly deduced by external measurement of the physical EMI-filter as well as making reasonable assumptions.

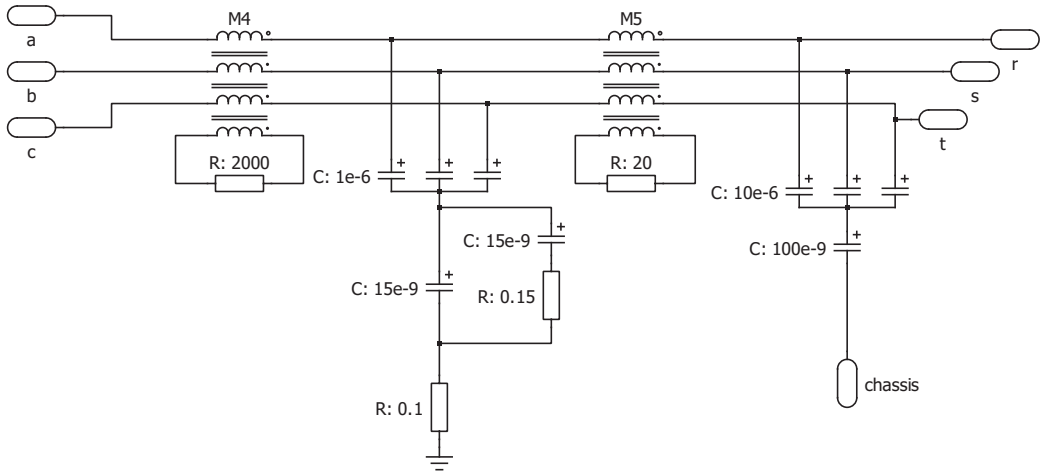


Figure A.5: The model of the EMI-filter used.

A.4 FIETS experimental setup

The schematics of the FIETS experimental setup is divided into three parts, Fig. A.6 - A.8. The dashed lines in Fig. A.6, A.7 indicates the floating chassis which can be grounded by the switch shown in Fig. A.6. The coloured boxes of Fig. A.7 indicates the conducting triplets of mechanical switches of the switch box when emulating isolated (blue) and non-isolated (green) charging respectively.

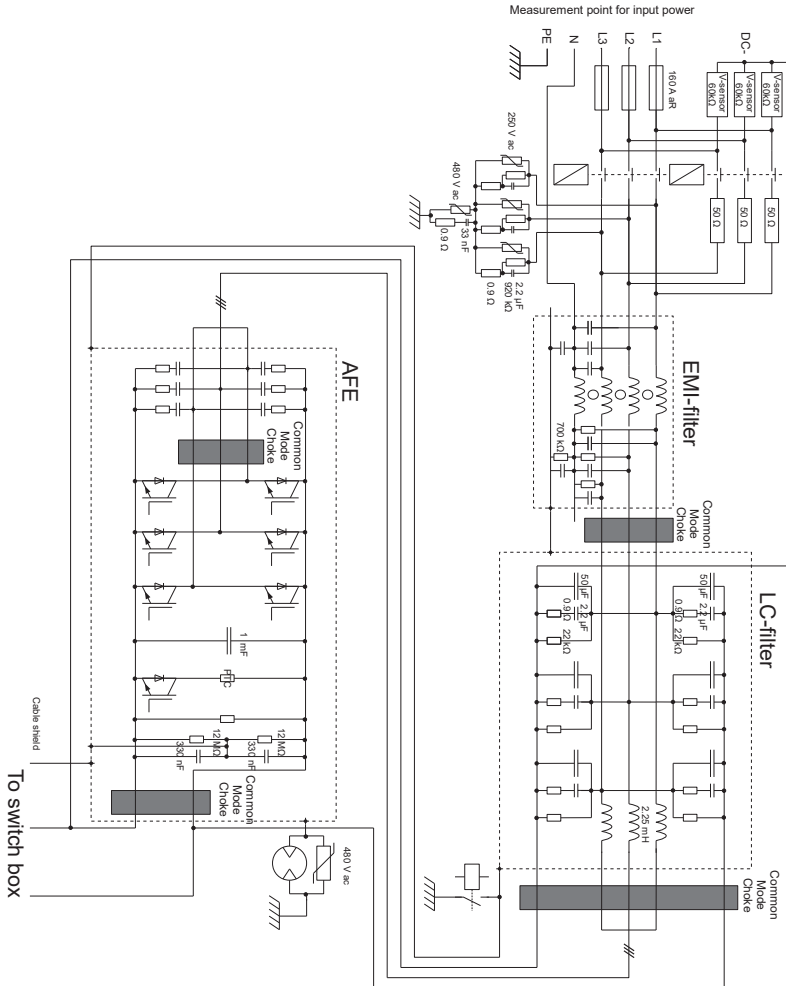


Figure A.6: The electrical schematics of the AFE and its supplying circuit.

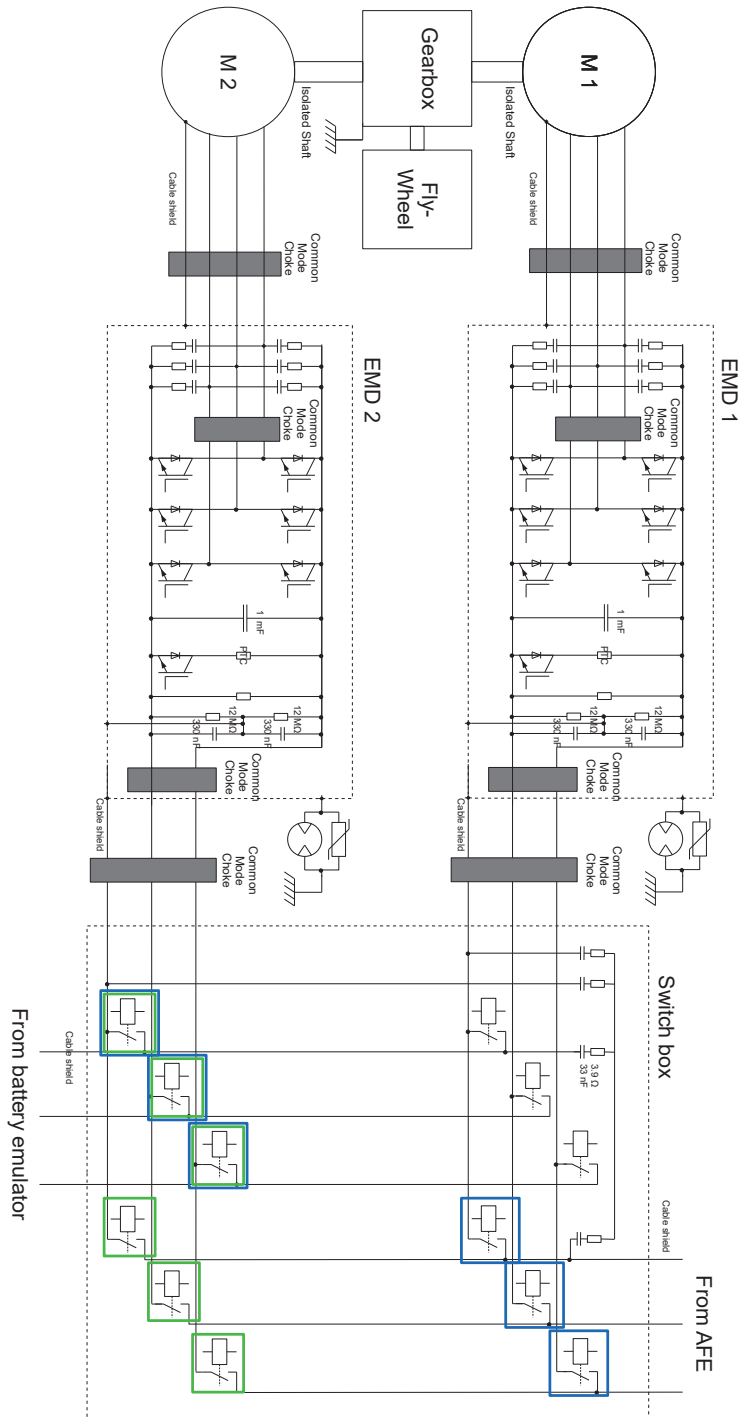


Figure A.7: The electrical schematics of the EMDs and switch box. The blue boxes indicates which switches are active when emulating isolated charging, the green ones the active switches when emulating non-isolated charging.

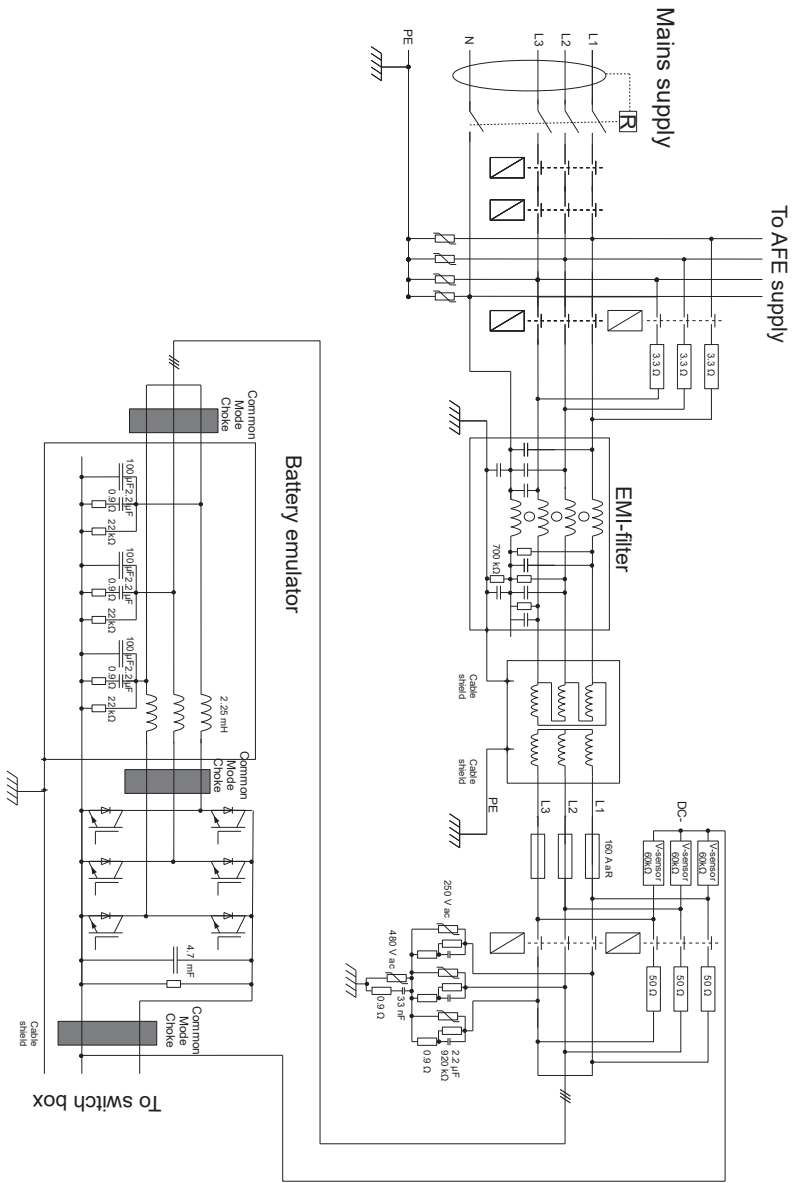


Figure A.8: The electrical schematics of the battery emulator.

References

- [1] IEA, “Global EV Outlook 2021,” tech. rep., IEA, Paris, 2021.
- [2] M. Fischer, M. Werber, and P. V. Schwartz, “Batteries: Higher energy density than gasoline?,” *Energy Policy*, vol. 37, no. 7, pp. 2639–2641, 2009.
- [3] ABB, “ABB launches the world’s fastest electric car charger, , accessed 2021-09-20.” https://resources.news.e.abb.com/attachments/published/82941/en-US/C60FB1B6D227/20210930_ABB_launches_the_worlds_fastest_electric_car_charger_EN.pdf, 2021.
- [4] “Iionity GmbH Technology, accessed 2021-09-20.” <https://ionity.eu/en/design-and-tech.html>.
- [5] C. Daake, C. Gehring, and M. Hackmann, “Comparison of the fast charging capability of different electric vehicles from an user perspective, accessed 2021-10-05,” tech. rep., P3 automotive GmbH, 2021.
- [6] M. Coffman, P. Bernstein, and S. Wee, “Electric vehicles revisited: a review of factors that affect adoption,” *Transport Reviews*, vol. 37, no. 1, pp. 79–93, 2017.
- [7] A. Adepetu and S. Keshav, “The relative importance of price and driving range on electric vehicle adoption: Los Angeles case study,” *Transportation*, vol. 44, p. 353–373, 2017.
- [8] Z. Liu, J. Song, J. Kubal, N. Susarla, K. W. Knehr, E. Islam, P. Nelson, and S. Ahmed, “Comparing total cost of ownership of battery electric vehicles and internal combustion engine vehicles,” *Energy Policy*, vol. 158, p. 112564, 2021.
- [9] F. Orsi, M. Muratori, M. Rocco, E. Colombo, and G. Rizzoni, “A multi-dimensional well-to-wheels analysis of passenger vehicles in different regions: Primary energy consumption, co2 emissions, and economic cost,” *Applied Energy*, vol. 169, pp. 197–209, 2016.
- [10] Spielvogel, “Plug-in hybrid vehicle (PHV) - on board charger for Toyota Prius. Photo taken at exhibition IAA 2015 in Frankfurt, Germany.” licensed under CC BY-SA 4.0.

- [11] A. Ahmad, Z. A. Khan, M. S. Alam, and S. Khateeb, “A review of the electric vehicle charging techniques, standards, progression and evolution of ev technologies in germany,” *Smart Science*, vol. 6, no. 1, pp. 36–53, 2018.
- [12] Donald Trung Quoc Don - Wikimedia Commons.
- [13] R. Collin, Y. Miao, A. Yokochi, P. Enjeti, and A. von Jouanne, “Advanced electric vehicle fast-charging technologies,” *Energies*, vol. 12, no. 10, 2019.
- [14] NJo, “Demonstration of wireless charge during parking. In Tokyo Motor Show 2011.” licensed under CC BY-SA 3.0.
- [15] K. A. Kalwar, M. Aamir, and S. Mekhilef, “Inductively coupled power transfer (icpt) for electric vehicle charging – a review,” *Renewable and Sustainable Energy Reviews*, vol. 47, pp. 462–475, 2015.
- [16] A. F. A. Aziz, M. F. Romlie, and Z. Baharudin, “Review of inductively coupled power transfer for electric vehicle charging,” *IET Power Electronics*, vol. 12, no. 14, pp. 3611–3623, 2019.
- [17] T. M. Fisher, K. B. Farley, Y. Gao, H. Bai, and Z. T. H. Tse, “Electric vehicle wireless charging technology: a state-of-the-art review of magnetic coupling systems,” *Wireless Power Transfer*, vol. 1, no. 2, p. 87–96, 2014.
- [18] S. Niu, H. Xu, Z. Sun, Z. Shao, and L. Jian, “The state-of-the-arts of wireless electric vehicle charging via magnetic resonance: principles, standards and core technologies,” *Renewable and Sustainable Energy Reviews*, vol. 114, p. 109302, 2019.
- [19] A. A. Mohamed, A. A. Shaier, H. Metwally, and S. I. Selem, “A comprehensive overview of inductive pad in electric vehicles stationary charging,” *Applied Energy*, vol. 262, p. 114584, 2020.
- [20] A. Genovese, F. Ortenzi, and C. Villante, “On the energy efficiency of quick DC vehicle battery charging,” *World Electric Vehicle Journal*, vol. 7, 2015.
- [21] H. Sundelin, M. G. H. Gustavsson, and S. Tongur, “The maturity of electric road systems,” in *2016 International Conference on Electrical Systems for Aircraft, Railway, Ship Propulsion and Road Vehicles International Transportation Electrification Conference (ESARS-ITEC)*, pp. 1–5, 2016.
- [22] M. Hellgren and N. Honeth, “Efficiency of an AC conductive in-road charging system for electric vehicles-analysis of pilot project data,” *SAE International Journal of Alternative Powertrains*, vol. 9, 2020.

- [23] R. Bosshard and J. W. Kolar, "Multi-objective optimization of 50 kw/85 khz ipt system for public transport," *IEEE Journal of Emerging and Selected Topics in Power Electronics*, vol. 4, no. 4, pp. 1370–1382, 2016.
- [24] C.-S. Wang, G. Covic, and O. Stielau, "Investigating an LCL load resonant inverter for inductive power transfer applications," *IEEE Transactions on Power Electronics*, vol. 19, no. 4, pp. 995–1002, 2004.
- [25] T. Tajima, W. Noguchi, , and T. Aruga, "Study of a dynamic charging system for achievement of unlimited cruising range in EV," tech. rep., Honda R I& D Co., Ltd., 2015.
- [26] B. Nykvist and M. Nilsson, "Rapidly falling costs of battery packs for electric vehicles," *Nature Clim Change*, vol. 5, pp. 329–332, 2015.
- [27] Y. Ding, Z. Cano, A. Yu, and et al., "Automotive Li-Ion batteries: Current status and future perspectives," *Electrochem. Energ. Rev.*, vol. 2, p. 1–28, 2019.
- [28] G. Domingues-Olavarría, F. J. Márquez-Fernández, P. Fyhr, A. Reinap, and M. Alaküla, "Electric roads: Analyzing the societal cost of electrifying all danish road transport," *World Electric Vehicle Journal*, vol. 9, no. 1, 2018.
- [29] P. Fyhr, G. Domingues, M. Andersson, F. J. Márquez-Fernández, H. Bängtsson, and M. Alaküla, "Electric roads: Reducing the societal cost of automotive electrification," in *2017 IEEE Transportation Electrification Conference and Expo (ITEC)*, pp. 773–778, 2017.
- [30] The Swedish Government, "(In Swedish) Uppdrag att planera för en utbyggnad av elvägar, accessed 2021-10-14." <https://www.regeringen.se/4a952c/contentassets/20544bf1b8aa4176900508ae667ee356/uppdrag-att-planera-for-en-utbyggnad-av-elvagar.pdf>, 2020.
- [31] Z. Zhang, H. Pang, C. H. T. Lee, X. Xu, X. Wei, and J. Wang, "Comparative analysis and optimization of dynamic charging coils for roadway-powered electric vehicles," *IEEE Transactions on Magnetics*, vol. 53, no. 11, pp. 1–6, 2017.
- [32] L. Tan, W. Zhao, H. Liu, J. Li, and X. Huang, "Design and optimization of ground-side power transmitting coil parameters for ev dynamic wireless charging system," *IEEE Access*, vol. 8, pp. 74595–74604, 2020.
- [33] D. M. Nguyen, M. A. Kishk, and M.-S. Alouini, "Modeling and analysis of dynamic charging for evs: A stochastic geometry approach," *IEEE Open Journal of Vehicular Technology*, vol. 2, pp. 17–44, 2021.

- [34] S. Jeong, Y. J. Jang, and D. Kum, “Economic analysis of the dynamic charging electric vehicle,” *IEEE Transactions on Power Electronics*, vol. 30, no. 11, pp. 6368–6377, 2015.
- [35] P. Machura, V. De Santis, and Q. Li, “Driving range of electric vehicles charged by wireless power transfer,” *IEEE Transactions on Vehicular Technology*, vol. 69, no. 6, pp. 5968–5982, 2020.
- [36] M. Alaküla and F. J. Márquez-Fernández, “Dynamic charging solutions in Sweden: An overview,” in *2017 IEEE Transportation Electrification Conference and Expo, Asia-Pacific (ITEC Asia-Pacific)*, pp. 1–6, 2017.
- [37] T. Tajima, H. Tanaka, T. Fukuda, Y. Nakasato, and et al., “Study of high power dynamic charging system,,” tech. rep., Honda R I& D Co., Ltd., 2017.
- [38] M. Y. Metwly, M. S. Abdel-Majeed, A. S. Abdel-Khalik, R. A. Hamdy, M. S. Hamad, and S. Ahmed, “A Review of Integrated On-Board EV Battery Chargers: Advanced Topologies, Recent Developments and Optimal Selection of FSCW Slot/Pole Combination,” *IEEE Access*, vol. 8, pp. 85216–85242, 2020.
- [39] I. Subotic, N. Bodo, E. Levi, M. Jones, and V. Levi, “Isolated Chargers for EVs Incorporating Six-Phase Machines,” *IEEE Transactions on Industrial Electronics*, vol. 63, no. 1, pp. 653–664, 2016.
- [40] A. S. Abdel-Khalik, A. Massoud, and S. Ahmed, “Interior permanent magnet motor-based isolated on-board integrated battery charger for electric vehicles,” *IET Electric Power Applications*, vol. 12, no. 1, pp. 124–134, 2018.
- [41] S. Haghbin, S. Lundmark, M. Alakula, and O. Carlson, “An isolated high-power integrated charger in electrified-vehicle applications,” *IEEE Transactions on Vehicular Technology*, vol. 60, no. 9, pp. 4115–4126, 2011.
- [42] V. Šmídl, t. Janouš, and Z. Peroutka, “Improved stability of dc catenary fed traction drives using two-stage predictive control,” *IEEE Transactions on Industrial Electronics*, vol. 62, no. 5, pp. 3192–3201, 2015.
- [43] D. Wenander, P. Abrahamsson, F. Marquez-Fernandez, and M. Alaküla, “Measuring electric properties of a conductive electric road,” in *2021 AEIT Automotive Conference*, 2021.
- [44] “IEC 62196.” International Electrotechnical Commission, ”Plugs, socket-outlets, vehicle connectors and vehicle inlets – Conductive charging of electric vehicles”.
- [45] C. Shi, Y. Tang, and A. Khaligh, “A three-phase integrated onboard charger for plug-in electric vehicles,” *IEEE Transactions on Power Electronics*, vol. 33, no. 6, pp. 4716–4725, 2018.

- [46] I. Subotic, N. Bodo, E. Levi, and M. Jones, "Onboard integrated battery charger for EVs using an asymmetrical nine-phase machine," *IEEE Transactions on Industrial Electronics*, vol. 62, no. 5, pp. 3285–3295, 2015.
- [47] L. Solero, "Nonconventional on-board charger for electric vehicle propulsion batteries," *IEEE Transactions on Vehicular Technology*, vol. 50, no. 1, pp. 144–149, 2001.
- [48] S.-K. Sul and S.-J. Lee, "An integral battery charger for four-wheel drive electric vehicle," *IEEE Transactions on Industry Applications*, vol. 31, no. 5, pp. 1096–1099, 1995.
- [49] D. Thimmesch, "An SCR inverter with an integral battery charger for electric vehicles," *IEEE Transactions on Industry Applications*, vol. IA-21, no. 4, pp. 1023–1029, 1985.
- [50] M. S. Diab, A. A. Elserougi, A. S. Abdel-Khalik, A. M. Massoud, and S. Ahmed, "A Nine-Switch-Converter-Based Integrated Motor Drive and Battery Charger System for EVs Using Symmetrical Six-Phase Machines," *IEEE Transactions on Industrial Electronics*, vol. 63, no. 9, pp. 5326–5335, 2016.
- [51] L. De Sousa, B. Silvestre, and B. Bouchez, "A combined multiphase electric drive and fast battery charger for electric vehicles," in *2010 IEEE Vehicle Power and Propulsion Conference*, pp. 1–6, 2010.
- [52] G. E. P. Box, "Science and statistics," *Journal of the American Statistical Association*, vol. 71, no. 356, pp. 791–799, 1976.
- [53] K. Jonasson, *Control of Hybrid Electric Vehicles with Diesel Engines*. PhD thesis, Department of Industrial Electrical Engineering and Automation, Faculty of Engineering, Lund University (LTH), 2005.
- [54] M. Alakula, K. Jonasson, C. Andersson, B. Simonsson, and S. Marksell, "Hybrid drive systems for vehicles, part 1." Course material, Department of Industrial Electrical Engineering and Automation, Faculty of Engineering, Lund University (LTH), 2004.
- [55] F. J. Marquez-Fernandez, *Electric traction machine design for an E-RWD unit*. PhD thesis, Department of Industrial Electrical Engineering and Automation, Faculty of Engineering, Lund University (LTH), 2014.
- [56] The MathWorks, Inc., "Stateflow Toolbox, accessed 2021-10-17." <https://www.mathworks.com/products/stateflow.html>, 2018.
- [57] E. Gundabattini, A. Mystkowski, A. Idzkowski, R. Singh R., and D. G. Solomon, "Thermal mapping of a high-speed electric motor used for traction applications and analysis of various cooling methods—a review," *Energies*, vol. 14, no. 5, 2021.

- [58] S. Hall, *Testing and Modelling of Electrical Traction Machines - Performance Characterisation with Measurements from Transient Operation*. PhD thesis, Department of Industrial Electrical Engineering and Automation, Faculty of Engineering, Lund University (LTH), 2019.
- [59] M. Hannan, M. Lipu, A. Hussain, and A. Mohamed, "A review of lithium-ion battery state of charge estimation and management system in electric vehicle applications: Challenges and recommendations," *Renewable and Sustainable Energy Reviews*, vol. 78, pp. 834–854, 2017.
- [60] D. Wang, Y. Bao, and J. Shi, "Online lithium-ion battery internal resistance measurement application in state-of-charge estimation using the extended kalman filter," *Energies*, vol. 10, no. 9, 2017.
- [61] A. International, "ASTM Standard E 1049, 1985 Standard practices for cycle counting in fatigue analysis.," 2011.
- [62] P. Zhang, J. Liang, and F. Zhang, "An overview of different approaches for battery lifetime prediction," *IOP Conference Series: Materials Science and Engineering*, vol. 199, p. 012134, may 2017.
- [63] M. J. Swierczynski, *Lithium ion battery energy storage system for augmented wind power plants*. PhD thesis, Department of Energy Technology, Aalborg University, 2012.
- [64] S. Atalay, M. Sheikh, A. Mariani, Y. Merla, E. Bower, and W. D. Widanage, "Theory of battery ageing in a lithium-ion battery: Capacity fade, nonlinear ageing and lifetime prediction," *Journal of Power Sources*, vol. 478, p. 229026, 2020.
- [65] N. Omar, Y. Firouz, H. Gualous, J. Salminen, T. Kallio, J. Timmermans, T. Coosemans, P. Van den Bossche, and J. Van Mierlo, "9 - aging and degradation of lithium-ion batteries," in *Rechargeable Lithium Batteries* (A. A. Franco, ed.), Woodhead Publishing Series in Energy, pp. 263–279, Woodhead Publishing, 2015.
- [66] W.-S. Lee, J.-H. Kim, J.-Y. Lee, and I.-O. Lee, "Design of an Isolated DC/DC Topology With High Efficiency of Over 97% for EV Fast Chargers," *IEEE Transactions on Vehicular Technology*, vol. 68, no. 12, pp. 11725–11737, 2019.
- [67] B.-K. Lee, J.-P. Kim, S.-G. Kim, and J.-Y. Lee, "An Isolated/Bidirectional PWM Resonant Converter for V2G(H) EV On-Board Charger," *IEEE Transactions on Vehicular Technology*, vol. 66, no. 9, pp. 7741–7750, 2017.
- [68] M. Hossain, N. Rahim, and J. a/l Selvaraj, "Recent progress and development on power DC-DC converter topology, control, design and applications: A review," *Renewable and Sustainable Energy Reviews*, vol. 81, pp. 205–230, 2018.

- [69] S. Chakraborty, H.-N. Vu, M. M. Hasan, D.-D. Tran, M. E. Baghdadi, and O. Hegazy, “DC-DC Converter Topologies for Electric Vehicles, Plug-in Hybrid Electric Vehicles and Fast Charging Stations: State of the Art and Future Trends,” *Energies*, vol. 12, no. 8, 2019.
- [70] Plexim, Electrical Engineering Software, “Plecs, The Simulation Platform for Power Electronic Systems, accessed 2022-01-30.” <https://www.plexim.com/products/plecs>, 2022.
- [71] M. Bollen, G. de Castro, and S. Rönnerberg, “Typical harmonic levels and spectra with low-voltage customers,” in *CIREC 2019 Conference*, 2019.
- [72] J. Lundquist, “On harmonic distortion in power systems.” Licentiate thesis, Chalmers University of Technology, 2001.
- [73] National Instruments Corp., “CompactRio Systems, accessed 2021-10-20.” <https://www.ni.com/sv-se/shop/compactrio.html>, 2021.
- [74] Hioki E.E. Corporation, “LCR METER IM3533, accessed 2021-10-29.” https://www.hioki.com/global/products/lcr-meters/10-mhz/id_6065, 2018.
- [75] Y.-G. Wang and H.-H. Shao, “Optimal tuning for PI controller,” *Automatica*, vol. 36, no. 1, pp. 147–152, 2000.
- [76] L. Harnefors and H.-P. Nee, “Model-based current control of ac machines using the internal model control method,” *IEEE Transactions on Industry Applications*, vol. 34, no. 1, pp. 133–141, 1998.
- [77] Newtons 4th Ltd, “PPA5500 user manual, accessed 2021-11-01.” https://www.newtons4th.com/wp-content/uploads/2021/03/D000229_PPA5500-User-Manual.pdf, 2017.
- [78] Newtons 4th Ltd, “LEM-6 interface user manual, accessed 2021-11-01.” <https://www.newtons4th.com/wp-content/uploads/2014/07/LEM-6-Interface-PDF-Jan-2019.pdf>, 2017.
- [79] PM Special Measuring Systems B.V., “Specification of the MACC 2 plus, accessed 2021-11-01.” <http://www.pm-sms.com/files/2016/02/Specifications-MACC-2-plus.pdf>, 2017.
- [80] A. Babuta, B. Gupta, A. Kumar, and S. Ganguli, “Power and energy measurement devices: A review, comparison, discussion, and the future of research,” *Measurement*, vol. 172, p. 108961, 2021.
- [81] GMC Instrumentation Ltd, “GMC-I Prosys CP30, accessed 2021-11-02.” https://www.gmciuk.com/gmc_i-prosys-cp30-80, 2021.

- [82] Fluke Corporation, “Fluke i3000s Flex AC current probe, accessed 2021-11-02.” <https://www.fluke.com/sv-se/produkt/tillbehor/stromtanger/fluke-i3000-flex-4pk>, 2021.
- [83] Fluke Corporation, “Fluke 801-1000s AC current probe, accessed 2021-11-02.” <https://www.fluke.com/sv-se/produkt/tillbehor/prober/fluke-i1000s>, 2021.
- [84] Pico Technology Limited, “PicoScope 4000A Series, accessed 2021-11-02.” <https://www.picotech.com/oscilloscope/4000/picoscope-4000-series>, 2021.
- [85] Els akerhetsverket, “(Swedish) SS-EN 61008-1. Jordfelsbrytare utan inbyggt  verstr msskydd f r bostadsinstallationer och liknande (RCCB) - Del 1: Allm nna regler. Avsnitt 5.3.12, tabell 1.”
- [86] J. D’Errico, “Surface Fitting using gridfit, MATLAB Central File Exchange , accessed 2021-11-01.” <https://www.mathworks.com/matlabcentral/fileexchange/8998-surface-fitting-using-gridfit>, 2021.
- [87] EUR-Lex, “Council Directive 96/53/EC of 25 July 1996 laying down for certain road vehicles circulating within the community the maximum authorized dimensions in national and international traffic and the maximum authorized weights in international traffic.” <http://data.europa.eu/eli/dir/1996/53/2019-08-14>, 2019.
- [88] Trafikanalys, “(Swedish) K rstr ckor med svenskregistrerade fordon.” <https://www.trafa.se/vagtrafik/korstrackor>, 2020.
- [89] K. Kivek s, A. Lajunen, J. Veps l inen, and K. Tammi, “City bus powertrain comparison: Driving cycle variation and passenger load sensitivity analysis,” *Energies*, vol. 11, no. 7, 2018.
- [90] A. K nig, L. Nicoletti, D. Schr der, S. Wolff, A. Waclaw, and M. Lienkamp, “An overview of parameter and cost for battery electric vehicles,” *World Electric Vehicle Journal*, vol. 12, no. 1, 2021.
- [91] P. Ahmadi, X. Cai, and M. Khanna, “Multicriterion optimal electric drive vehicle selection based on lifecycle emission and lifecycle cost,” *International Journal of Energy Research*, vol. 42, no. 4, pp. 1496–1510, 2018.
- [92] D. G hlich, T.-A. Fay, D. Jefferies, E. Lauth, A. Kunitz, and X. Zhang, “Design of urban electric bus systems,” *Design Science*, vol. 4, p. e15, 2018.

- [93] A. Tüysüz, F. Meyer, M. Steichen, C. Zwyssig, and J. W. Kolar, “Advanced cooling methods for high-speed electrical machines,” *IEEE Transactions on Industry Applications*, vol. 53, no. 3, pp. 2077–2087, 2017.
- [94] A. Reinap, F. J. Márquez-Fernández, R. Andersson, C. Högmark, M. Alaküla, and A. Göransson, “Heat transfer analysis of a traction machine with directly cooled laminated windings,” in *2014 4th International Electric Drives Production Conference (EDPC)*, pp. 1–7, 2014.
- [95] S. Estenlund, “Model of air cooled windings for traction machine,” in *2018 XIII International Conference on Electrical Machines (ICEM)*, pp. 1278–1284, 2018.
- [96] T. M. Inc., *Fast Fourier Transform Toolbox*, accessed 2021-10-10. Natick, Massachusetts, U.S., 2018.
- [97] H. Fujita and H. Akagi, “A practical approach to harmonic compensation in power systems-series connection of passive and active filters,” *IEEE Transactions on Industry Applications*, vol. 27, no. 6, pp. 1020–1025, 1991.
- [98] P. Mattavelli, “A closed-loop selective harmonic compensation for active filters,” *IEEE Transactions on Industry Applications*, vol. 37, no. 1, pp. 81–89, 2001.
- [99] N. Mohan, T. M. Undeland, and W. P. Robins, *Power Electronics, 3rd Edition*. John Wiley I& Sons, Inc., 2003.
- [100] L. Ben-Brahim, “The analysis and compensation of dead-time effects in three phase pwm inverters,” in *IECON '98. Proceedings of the 24th Annual Conference of the IEEE Industrial Electronics Society (Cat. No.98CH36200)*, vol. 2, pp. 792–797 vol.2, 1998.
- [101] T. Messo, T. Roinila, A. Aapro, and P. Rasilo, “Evaluation of dead-time effect of grid-connected inverters using broadband methods,” *IFAC-PapersOnLine*, vol. 51, no. 15, pp. 449–454, 2018. 18th IFAC Symposium on System Identification SYSID 2018.
- [102] Y. Ji, Y. Yang, J. Zhou, H. Ding, X. Guo, and S. Padmanaban, “Control strategies of mitigating dead-time effect on power converters: An overview,” *Electronics*, vol. 8, no. 2, 2019.
- [103] P. Widek and M. Alaküla, “Modeling of electric power system in electric vehicles,” in *2020 International Symposium on Power Electronics, Electrical Drives, Automation and Motion (SPEEDAM)*, pp. 293–298, 2020.



Division of Industrial Electrical
Engineering and Automation
Department of Biomedical Engineering

Faculty of Engineering, Lund University
ISBN 978-91-985109-4-2
CODEN: LUTEDX/(TEIE-1095)/1-149/(2022)

